ABSTRACT

Title of dissertation: NEAR-FIELD MICROWAVE MICROSCOPY AND MULTIVARIATE ANALYSIS OF XRD DATA

Christian Long, Doctor of Philosophy, 2011

Dissertation directed by: Professor Ichiro Takeuchi
Department of Physics

The combinatorial approach to materials research is based on the synthesis of hundreds or thousands of related materials in a single experiment. The popularity of this approach has created a demand for new tools to rapidly characterize these materials libraries and new techniques to analyze the resulting data. The research presented here is intended to make a contribution towards meeting this demand, and thereby advance the pace of materials research.

The first part of the dissertation discusses the development of a materials characterization tool called a near field microwave microscope (NFMM). We focus on one particular NFMM topology, the open ended coaxial resonator. The traditional application of this NFMM topology is the characterization of the dielectric properties of materials at GHz frequencies. With the goal of expanding the capabilities of the NFMM beyond this role, we explore two non-traditional modes of operation. The first mode is scanning ferromagnetic resonance spectroscopy. Using this technique, we map the magnetostatic spin wave modes of a single crystal gallium doped yttrium iron garnet disk. The second mode of operation entails combining near field

microscopy with scanning tunneling microscopy (STM). Operating in this mode, we show that the NFMM is capable of obtaining atomic resolution images by coupling microwaves through an atomic scale tunnel junction.

The second part of the dissertation discusses the analysis of X-Ray Diffraction (XRD) data from combinatorial libraries. We focus on two techniques that are designed to simultaneously analyze all of the XRD spectra from a given experiment, providing a faster method than the traditional one-at-a-time approach. First, we discuss agglomerative hierarchical cluster analysis, which is used to identify regions of composition space that have similar crystal structures. Second, we discuss non-negative matrix factorization (NMF). NFM is used to decompose many experimental diffraction patterns into a smaller number of constituent patterns; ideally, these constituent patterns represent the unique crystal structures present in the samples. Compared to hierarchical clustering, NMF has the advantage of identifying multi-phase regions within the composition space. These techniques are also applicable to other types of spectral data, such as FTIR, Raman spectroscopy, XPS, and mass spectrometry.

NEAR-FIELD MICROWAVE MICROSCOPY AND MULTIVARIATE ANALYSIS OF XRD DATA

by

Christian Long

Dissertation submitted to the Faculty of the Graduate School of the
University of Maryland, College Park in partial fulfillment
of the requirements for the degree of
Doctor of Philosophy
2011

Advisory Committee:
Professor Ichiro Takeuchi, Chair/Advisor
Professor Steven Anlage
Professor Michael Fuhrer
Professor Richard Greene
Professor Romel Gomez

Dedication

To my wife, Johanna, and parents, John and Danielle.

Acknowledgments

I would first like to thank my advisor, Professor Ichiro Takeuchi, for offering me the opportunity to work on a variety of interesting and rewarding projects. He has provided me with just the right balance of guidance and freedom to make pursuing research an incredible joy. I consider it an honor to have him as a mentor and a friend.

I would like to thank my present and former group members Anbu Varatharajan, Arun Luykx, Daisuke Kan, Debjani Banerjee, Dwight Hunter, Emad Din, Fengxia Yang, Luz Sanchez, Peng Zhao, Richard Suchoski, Tiberiu Dan Onuta, Sean Fackler, Yi Wang, Tieren Gao, Iain Kierzewski, Yiming Wu, Gilad Kusne, Hiroyuki Oguchi, Olugbenga Famodu, Ryota Takahashi, Shige Fujino, Sung Hwan Lim, Tamin Tai, Kao-Shuo Chang, and Antonio Zambano for many fruitful discussions.

I would like to thank Jason Hattrick-Simpers for fabricating thin film combinatorial libraries and sharing all of his combinatorial data, Makoto Murakami for his contributions in performing XRD, Stephen Yang for his contributions to coding CombiView, Stephen Kitt for his contributions in compiling and running RKMAG simulations, David Bunker for his assistance in getting the non-negative matrix factorization code working, Jonghee Lee for his frequent assistance in getting the NFMM-STM system running, Naoyuki Taketoshi for his assistance in performing FMR using the NFMM-AFM system, and Nathan Orloff for discussions about microwave measurements.

I would like to thank Samuel Lofland for his insights into the theory of ferro-

magnetic resonance, Steven Anlage for insightful conversations about microwave microscopy, Jack Touart for his help in building and repairing custom electronics, and Haitao Yang for answering many questions about microwave microscopy.

I would also like to thank all of the staff members at UMD, who make it possible for me to spend the great majority of my time in the laboratory.

My deepest thanks I owe to my wife, Johanna, and parents, John and Danielle, for the love and unwavering support they have provided throughout my studies.

Contents

List of Tables

List of Figures

List of Abbreviations

A/D	Analog to Digital
AFM	Atomic Force Microscopy
BCC	Body Centered Cubic
D/A	Digital to Analog
DC	Direct Current or zero frequency
FCT	Face Centered Tetragonal
FCC	Face Centered Cubic
FMR	Ferromagnetic Resonance or Ferrimagnetic Resonance
GHz	10^9 Hz
f_{r}	Resonant Frequency
FMR	Ferromagnetic Resonance
FSMA	Ferromagnetic Shape Memory Alloy
HOPG	Highly Ordered Paralytic Graphite
I_t	Tunnel Current
ICSD	Inorganic Crystal Structure Database
LCR	A type of Electrical Circuit Involving an Inductance (L) a Capacitance (C) and a Resistance (R)

PCA	Principle Component Analysis
PLL	Phase Locked Loop
RF	Radio Frequency
STM	Scanning Tunneling Microscopy
TEM	Transverse Electro-Magnetic
MFM	Magnetic Force Microscopy
MMDS	Metric Multidimensional Data Scaling
NIST	National Institute of Standards and Technology
NFMM	Near Field Microwave Microscopy
NMF	Non-Negative Matrix Factorization
Q	Quality Factor
VSM	Vibrating Sample Magnetometer
WDS	Wavelength Dispersive Spectroscopy
XRD	X-Ray Diffraction
YIG	Yttrium Iron Garnet ($Y_3Fe_5O_{12}$)
Z	The Out of Plane Direction for a Sample Mounted in a Scanning Probe

Chapter 1

Introduction

1.1 Motivation & Combinatorial Science

In this dissertation, we discuss two main topics. The first part of the dissertation focuses on a materials characterization technique called Near Field Microwave Microscopy (NFMM). The second part focuses on new techniques for analyzing X-Ray Diffraction (XRD) data. Both parts of this dissertation are motivated by the increasing popularity of the combinatorial approach to investigating new materials. The combinatorial approach has created a demand for the development of new tools to characterize the physical properties of materials, as well created demand for new techniques to rapidly analyze the data produced by these investigations. The research presented in this dissertation is intended to make a contribution to meet these demands, and thereby advance the pace of materials research. Before exploring NFMM and the analysis of XRD data in more detail, we would like to provide a brief introduction to combinatorial materials investigation.

The ultimate goal of materials science is to map out the relationship between the composition, structure, and physical properties of materials. Once these relationships are mapped out, the underlying physics that dictates these relationships can be explored. The composition-structure-property relationships can also be applied directly to engineering problems like the design of sensors or integrated circuits.

The traditional approach to mapping composition-structure-property relationships is to fabricate one material, measure its composition, measure its structure, measure its physical properties, and then move on to the next material of interest. After a large database of materials has been built up in this way, the data are compared in order to identify optimal materials, plan new experiments, and formulate physical theories about the composition-structure-property relationships. This process is not ideal for two main reasons. First, a large amount of time is required to fabricate and characterize a single material, making this a slow process. Second, the fabrication and characterization conditions are likely to be slightly different for each material fabricated, adding uncertainty to the resulting data.

Beginning around 1995, a new approach to materials exploration was developed in which many different (but closely related) materials are fabricated and characterized in a single run[1]. This method is called the "combinatorial approach" or simply "combi". This method allows for much more rapid exploration of materials systems than the traditional one-at-a-time approach. Frequently, the combinatorial approach also results in higher quality data because the processing conditions for all of the materials in a given experiment are identical.

Figure 1.1 illustrates an experiment that shows the hallmarks of the combinatorial approach: parallel sample fabrication followed by rapid characterization. The details of the complete experiment can be found in reference [9]. In this example, the sample was a composition gradient including all compositions from pure $CoFe_2O_3$ to

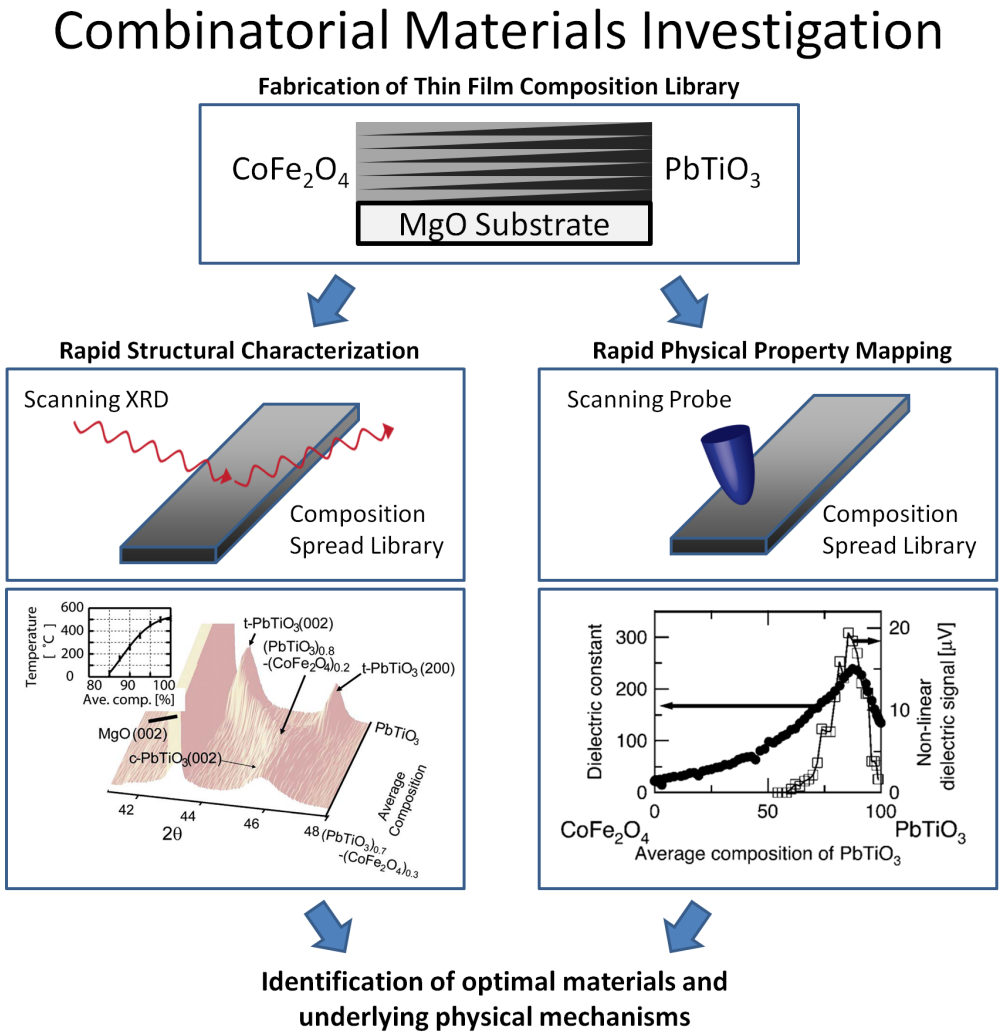

Figure 1.1: A schematic of the combinatorial approach to materials investigation. Characterization techniques such as scanning XRD and NFMM play a key role in rapid exploration of novel materials. In this example, a multiferroic nanocomposite displaying ferroelectricity and ferromagnetism was discovered in the $CoFe_2O_3$-$PbTiO_4$ binary system. For further details of this experiment see reference [9].

pure $PbTiO_4$[1]. Once the sample was fabricated, the relevent physical properties were mapped using high-throughput scanning probe techniques. The main motivation of this study was to identify candidate magnetoelectric materials, therefore the physical properties of interest were the magnetic and electrical ordering. The remnant magnetization was mapped using a room temperature scanning superconducting quantum interference device (SQUID) microscope, and the linear and non-linear dielectric constant were mapped using NFMM. Once these physical properties were measured, the crystal structure along the composition gradient was mapped out using scanning XRD. In the analysis of the resulting data, a material was found—specifically $(CoFe_2O_3)_{15}(PbTiO_4)_{85}$—that displayed a peak in the linear dielectric constant and a large dielectric tunability, while still showing robust magnetization. This made it a candidate material for further investigations of the magnetoelectric coefficient, which were later performed using NFMM[15]. The study also identified the physical mechanism corresponding to the enhanced dielectric properties, which was a structural transition from tetragonal to cubic symmetry.

There have been significant advances in the area of rapid characterization and screening techniques; there are now a variety of physical properties that can be mapped for combinatorial libraries and composition spreads with relatively quick turnaround[49, 50, 51, 61]. The combinatorial approach to materials research has proven to be effective in uncovering new materials phases with enhanced physical properties as well as rapidly mapping composition-structure-property relationships

[1]The composition gradient was created by depositing alternating wedges of $CoFe_2O_3$ and $PbTiO_4$ onto an MGO substrate; the deposition of wedge shaped layers was achieved using laser ablation in combination with a movable shutter system.

in complex materials systems [49, 50, 51]. In particular, composition spread experiments are instrumental in mapping compositional phase diagrams of multicomponent systems [52, 53, 54, 55]. Mapping phase diagrams is central in obtaining comprehensive pictures of materials systems, and mapping active physical properties such as magnetism and ferroelectricity as a function of composition is an integral part of understanding the underlying physical mechanism of the properties [55, 56, 57].

The diffusion-multiple approach—which entails annealing a conglomerate of three or more bulk metal pieces in order to form alloys of graded compositions—has been developed to map bulk phase diagrams[58, 59]. In thin film composition spreads, large fractions of compositional phase diagrams can be mapped out with a high density of data points on an individual wafer. The large number of data points can truly bring out the strength of the combinatorial technique because systematic mapping can reveal subtle composition dependence effects that are otherwise very difficult to discern from individual sample experiments with sparse sampling in composition space [55]. Thin film materials can often display properties with deviation from bulk samples, but it has been shown in many systems that one can indeed obtain compositional trends that closely resemble or mirror those of bulk counterparts [55, 60]. There are also instances where the target application of a specific materials system is a thin film device. In such cases, using thin film spread samples for mapping composition dependence is well justified [54].

1.2 Outline of this Dissertation

In Chapter 2 we provide an introduction to NFMM in general. We then introduce the coaxial resonator geometry of the NFMM, which is used throughout the first part of this dissertation. After introducing the resonator geometry we discuss a lumped-element circuit model of the resonator. The last section of this chapter discusses the microwave circuitry involved in the NFMM measurements.

In Chapter 3 we present an exploration of the possibility of using the open ended coaxial resonator NFMM topology to perform scanning ferromagnetic resonance spectroscopy. This chapter begins with an introduction to ferromagnetic resonance spectroscopy. We next present the details of the instrument used in this experiment, which is a hybrid between a shear mode atomic force microscope (AFM) and a NFMM. We then present the details of the experimental design and the data obtained. After an exposition of the experimental data, we describe the details and results of numerical micromagnetic simulations that were performed using the RKMAG software.

In Chapter 4 we present an experiment in which we demonstrate that the spatial resolution of the coaxial resonator NFMM can be pushed to the atomic limit by bringing the probe tip close enough to a conducting sample to form a tunnel junction. We begin with a description of the instrument, which is a custom built hybrid between an STM and a NFMM. Next we present images of the surface of Au(111) terraces and atomically resolved images of HOPG and a Au(111) surface.

In Chapter 5 we present a brief introduction and motivation to the problem of analyzing XRD data. We also present the experimental details of the fabrication

and characterization of the Fe-Ga-Pd combinatorial library that will be analyzed in Chapters 6 and 7.

In Chapter 6 we present a technique called agglomerative hierarchical cluster analysis and its application to the analysis of XRD data. We find that using cluster analysis we can select the optimal subset of the experimental diffraction patterns that are needed to identify all of the crystal structures present in a data set. The identified crystal structures can then be mapped onto the composition diagram using the grouping of samples obtained via cluster analysis, resulting in the creation of a structural phase diagram.

In Chapter 7 we present a technique called Non-negative Matrix Factorization (NMF) and apply it to the Fe-Ga-Pd XRD data. We find that NMF can be used to decompose the experimentally observed diffraction patterns into a much smaller number of basis patterns. The crystal structures corresponding to these basis patterns are then identified and the distribution of structures is plotted on the composition diagram. The advantages of using NMF compared to cluster analysis are that the basis patterns produced can have a significantly lower noise level than the experimental patterns, and the technique naturally allows for the identification of samples that are composed of a mixture of different crystal structures.

In Chapter 8 we provide a summary of the work presented in this dissertation and the main conclusions of each section.

Part I

Near-Field Microwave Microscopy

Chapter 2

Introduction to Near-Field Microwave Microscopy

Near Field Microwave Microscopy (NFMM) is a technique in which an antenna generating a microwave frequency electromagnetic field is used to probe the electrical or magnetic properties of a material nearby the antenna. The antenna is generally much smaller than the free space wavelength at the test frequency (in this case 12 cm at 2.5 GHz), and the material under test is generally close enough to the antenna that it is well within the near-field regime of the electromagnetic field created by the antenna[1]. Operating in the near-field regime provides two advantages. First, it allows for spatial resolutions that break the diffraction limit. This is critically important because the samples to be tested and features of interest are frequently much smaller than the wavelength of the probing radiation. Second, it greatly simplifies modeling the interaction between the antenna and the material under test. This simplification is possible because one can calculate the electric and magnetic fields using the electrostatic and/or magnetostatic approximations. These approximations reduce the difficulty of modeling the tip-sample interaction by removing the need to consider propagating, time dependent electromagnetic waves.

NFMM is most commonly used for mapping the high frequency dielectric properties of materials.[19, 20, 2, 3, 4] In our own research group, NFMM has been

[1]The near field region is usually defined as the region that is less than $2D^2/\lambda$ away from the antenna, where D is the size of the radiating feature of the antenna and λ is the free space wavelength at the antenna's operating frequency.

used extensively to map the dielectric properties of thin films from combinatorial material libraries.[5, 6, 7, 8, 9, 10] Among the other applications of NFMM are dopant profiling,[22] surface conductivity measurement,[11] high speed scanning probe imaging,[23] magnetic permeability measurement,[12, 13, 14] investigation of tunnel junction nonlinearity,[21] and potentially single-spin sensitive experiments[24, 25].

There are many different antenna designs used to perform NFMM, each specialized to a specific type of measurement. When choosing a near field antenna design, one faces three main design choices. The first choice is whether to select a probe designed for electrical or magnetic measurements. Probes designed for electrical measurements generally have an electric field anti-node and a magnetic field node in the region of probe-sample coupling. In the case of an electric field probe, the coupling between the probe and the sample is accomplished by bringing the sample under test into the region containing the electric fringe field between two electrodes. Probes designed for magnetic measurements generally have an electric field node and a magnetic field anti-node in the region of probe-sample coupling. The simplest example of such a probe consists of a wire loop through which a microwave current is driven. The second design choice is whether to choose a resonant or non-resonant design. In the resonant design, one gains additional sensitivity to materials properties at a specific frequency, whereas in the non-resonant design one can probe a wide range of frequencies. The final tradeoff is in the size of the antenna; larger antennas generally provide a higher signal-to-noise ratio because of a larger area of contact with the sample, while smaller antennas provide higher spatial resolution at the cost of a lower signal-to-noise ratio.

In this work, we focus on expanding the capabilities of one particular NFMM

probe, the open ended coaxial resonator. The coaxial resonator has a sharp tip that extends from the end of a coaxial cavity and couples to the sample under test. This type of design is optimized for electric field sensitive measurements (e.g. permittivity), as there is an electric field anti-node and a magnetic field node at the probe tip. It is also optimized for high sensitivity, narrow band measurements, as it is based on resonant detection. Lastly, when used for dielectric imaging, it is optimized for high spatial resolution, as the electric field from the sharp tip interacts with only a small area of a sample. When operating in the dielectric imaging mode, the spatial resolution of this probe geometry is on the order of the radius of curvature of the end of the probe tip[2]. The highest reported spatial resolution for a NFMM in the literature is $\sim$2.5 nm. This high spatial resolution was achieved using a hybrid NFMM-STM built at the University of Maryland by Atif Imtiaz under the direction of Professor Steven Anlage[17]. In their work, an open ended half wave coaxial resonator was used to perform NFMM while an integrated STM was used to maintain a constant tip-sample distance of $\sim$1 nm.

2.1 The Coaxial Resonator

In this work we focus on a microwave microscope topology that uses an open ended coaxial resonant cavity with a pointed tip used to interact with the sample surface. Figure 2.1 shows a schematic of the resonator.

The resonator is usually operated in its fundamental mode, which is the $\lambda/4$ quasi Transverse Electro-Magnetic (TEM) mode. Figure 2.2 shows the electric and mag-

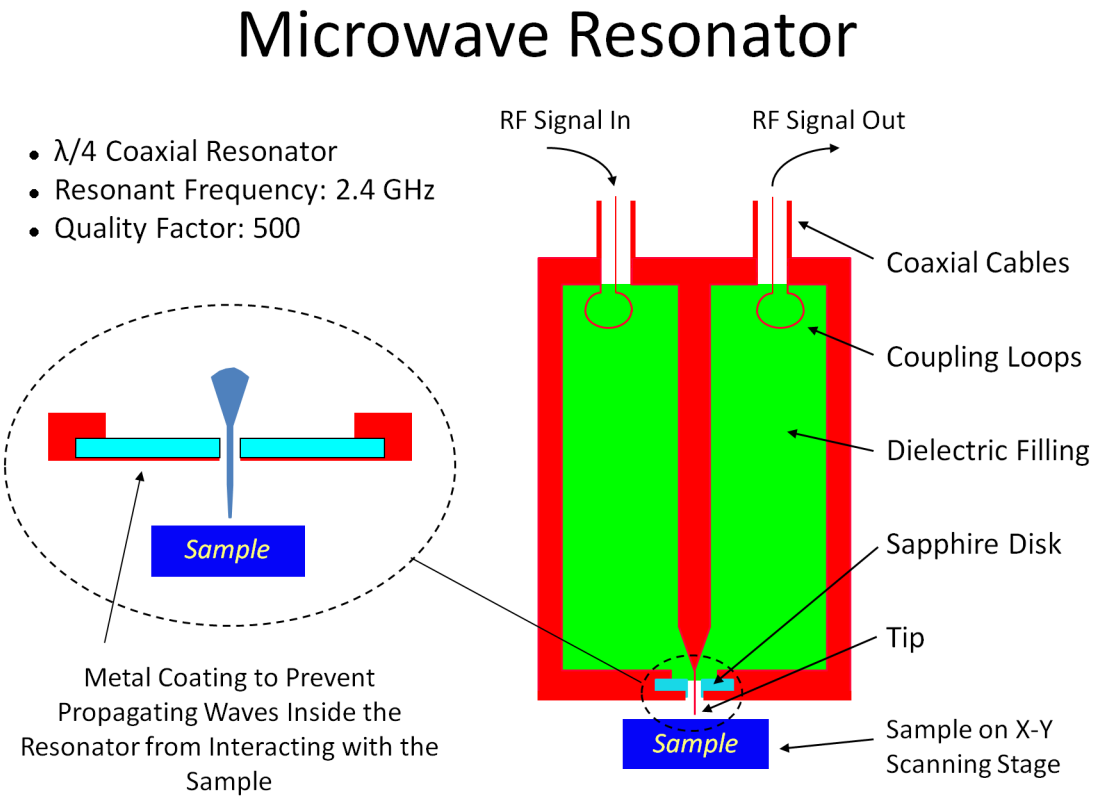

Figure 2.1: A general schematic of the microwave resonator that is used in our NFMM. The body of the resonator is essentially a short piece of coaxial waveguide ($\sim$1 cm long) that is shorted out at one end (the upper end in the figure) and almost closed at the other end. This geometry produces an electric field anti-node at the open end of the cavity, making this a good probe of the electrical properties of a sample. At the open end of the resonator, a sharp tip is connected to the center conductor and protrudes out of the resonator. To measure the permittivity of the sample, the change in the resonant frequency and quality factor of the resonator are observed as the tip is brought into contact with the sample.

netic field distributions inside the resonator for the fundamental mode. The electric field is strongest at the open end of the resonator, while the magnetic field is strongest near the closed end of the resonator. The strong electric field and sharp probe tip make this resonator very good for performing high sensitivity, high resolution imaging of the dielectric properties of a material[10]. The high sensitivity is obtained because a relatively large fraction of the electric field energy stored in the resonator is in the space around the probe tip. This means that if a sample with a large dielectric constant is brought into the region of the tip, the capacitance between the tip and the resonator body will be markedly increased. However, if a sample has a dielectric large loss tangent, then a large amount of the energy stored in the resonator will be dissipated.

In Figure 2.1 we see that microwave transmission lines are coupled to the resonator at the closed end using a single-turn wire loop. The strong azimuthal magnetic field at the base of the resonator is the reason that we use magnetic dipole antennas (wire loops) to couple the microwave transmission lines into the resonator. The use of inductive coupling between the resonator body and the microwave transmission lines also allows for low frequency electrical isolation between the resonator body and the microwave lines. This allows us to make a separate direct connection to the resonator body. This directly connected lead can then be used to add a low frequency bias voltage between the resonator and a sample, or to measure the low frequency current that flows between the tip and the sample.

In general, there are two pieces of information that can be obtained from the microwave resonator: the resonant frequency, f_{r}, and the quality factor, Q. In order

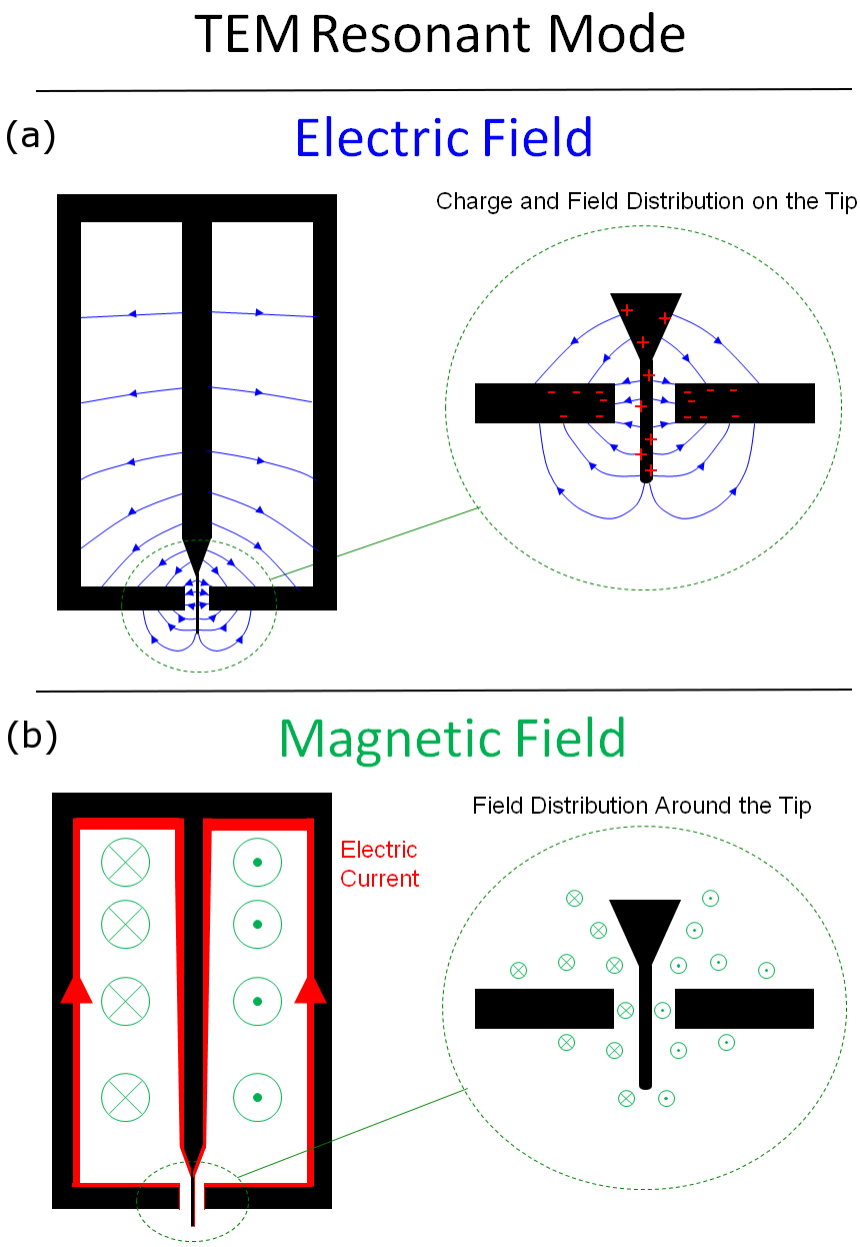

Figure 2.2: Cross sections of the resonator showing schematics of the microwave fields for the fundamental excitation mode. The electric field has a node at the closed end of the resonator and an anti-node at the open end, while the magnetic field has an anti-node at the closed end and a node at the open end. There is a sinusoidal time dependence to both fields (the resonant frequency is $\sim$2.5 GHz), and the magnetic field is 90 degrees out of phase with the electric field. The magnetic fields are perpendicular to the symmetry axis of the resonator and the electric fields are nearly so, making this a quasi-TEM mode.

to obtain these values we employ quadrature homodyne detection, which is discussed in greater detail in section 2.3. When the tip is brought into contact with a sample, the f_r and Q generally decrease due to the loading of the resonator by the sample under test. In order to understand this behavior and to convert these shifts into information about the physical properties of the sample, one needs a model of the resonator and the interactions between the resonator and the sample. The equivalent circuit model for the unloaded resonator is discussed in more detail in section 2.2.

The f_{r} and Q are very sensitive to the tip-sample distance. In order to maintain a constant tip-sample distance while scanning, NFMM is frequently combined with other scanning probe techniques such as atomic force microscopy (AFM) or scanning tunneling microscopy (STM). For the coaxial resonator geometry, the possible mechanisms of coupling to the sample surface are illustrated in Figure 2.3. For non-conducting samples, AFM is the usual choice for tip-sample distance control. For conducting samples, it is possible to use AFM or STM.

2.2 Circuit Model for the Unloaded Microwave Resonator

Experimentally, the information we obtain from probing a sample with the resonator is a shift in the f_{r} and Q of the resonator. In order to convert these shifts into information about the sample it is helpful to introduce a model of the resonator as well as a model of the tip-sample interaction. We model the unloaded (no tip sample interaction) resonator as a simple series circuit comprised of an inductance (L_R), a capacitance (C_R), and a resistance (R_R). The tip sample interaction is then modeled

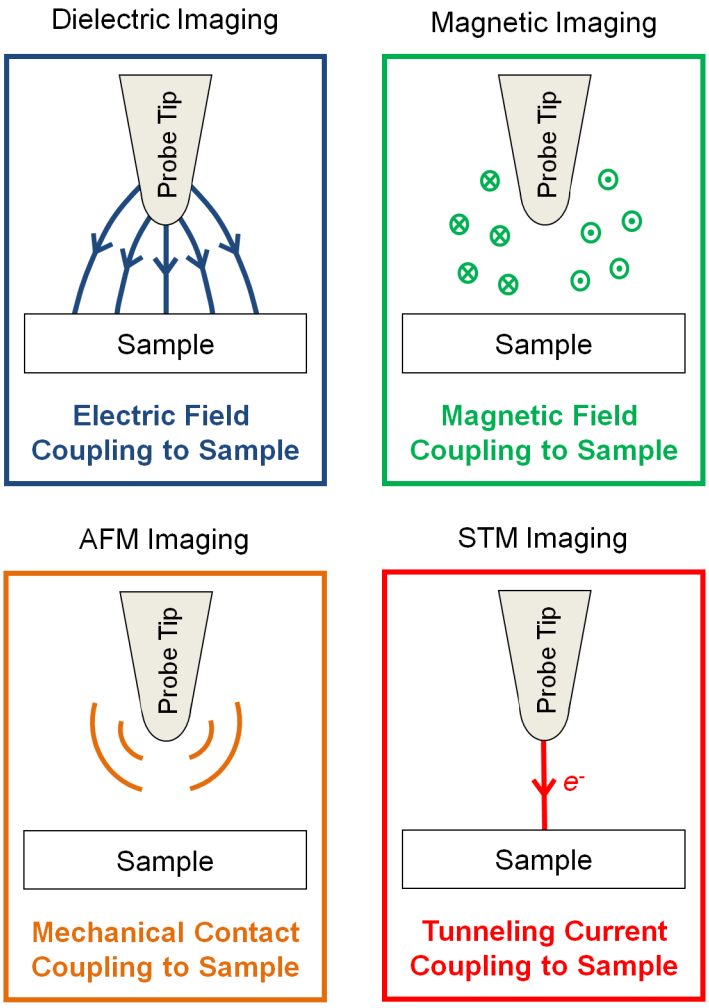

Figure 2.3: Schematic of the tip-sample coupling mechanisms for the four different imaging modes possible using a coaxial resonator.

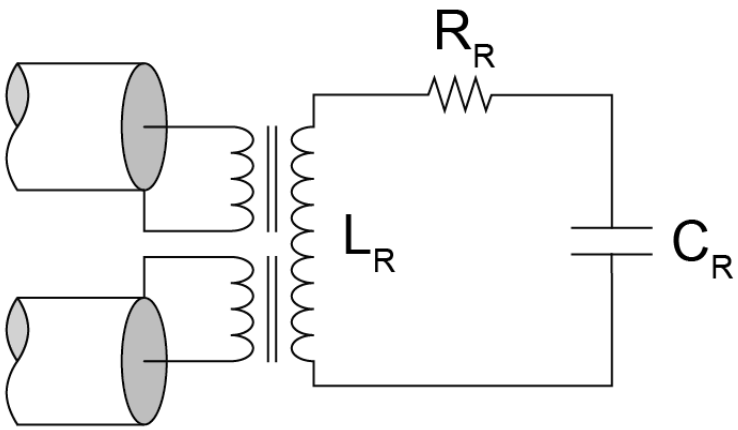

Figure 2.4: A lumped element model of the microwave resonator without any tip-sample interaction. Two coaxial cables are inductively coupled to the resonator; one cable is used to excite the resonator and the other is used to measure the excitation.

by adding additional circuit components to this basic LCR circuit. The values of these circuit elements are then calculated using the experimentally obtained shifts in the f_{r} and Q of the resonator, and the physical parameters of interest are calculated from the values of these circuit parameters using a model of the tip-sample interaction.

The circuit model of the resonator without any tip-sample interaction is pictured in Figure 2.4. The values of the circuit parameters L_R, $\mathrm{C_R}$, and R_R are calculated by approximating the resonator as a short length of coaxial cable. Using this approximation, we can easily calculate the capacitance per unit length or inductance per unit length of a short length of coaxial cable using Gauss' law or Ampere's law respectively. By multiplying this distributed capacitance and inductance by the length of the resonator, we could then come up with an order of magnitude approximation of the capacitance and inductance of the resonator[2]. However, these values would not be quite correct because the electric and magnetic fields inside the resonator are not uniform along its length. In particular, the electric field has a node at the closed end

of the resonator where the inner and outer conductors are connected and an anti-node at the open end of the resonator. In the fundamental mode, which is our usual mode of operation, there are no other nodes along the length of the resonator. Thus, to calculate the effective capacitance and inductance of the resonator we integrate along the length of the resonator while accounting for this field distribution. The integrand is then the distributed capacitance or inductance multiplied by the waveform of the field inside the resonator, in this case a quarter of a sine wave. The result of this integral is that there is an extra factor of one half in the values of the inductance and capacitance compared to what we would expect given a short length of cable with uniform fields.

$$L_R = \frac{1}{2}\frac{\mu_0\mu_r \log[b/a]}{2\pi} l \tag{2.1}$$

$$C_R = \frac{1}{2}\frac{2\pi\epsilon_0\epsilon_r}{\log[b/a]} l \tag{2.2}$$

Where ϵ_0 is the free space permittivity, ϵ_r is the relative permittivity of the dielectric filling of the resonator, a is the diameter of the inner conductor, b is the diameter of the outer conductor, l is the length of the resonator, μ_0 is the free space permittivity, and μ_r is the relative permeability of the resonator filling. Figure 2.5 shows a schematic of the resonator geometry parameters (a, b, and l). The value of the capacitance calculated in this way may also be a bit low because it does not include the effects of the fringing electric field at the open end of the resonator. In order to obtain more precise values for the lumped element circuit parameters, one could use a numerical technique such as finite element analysis to simulate the field

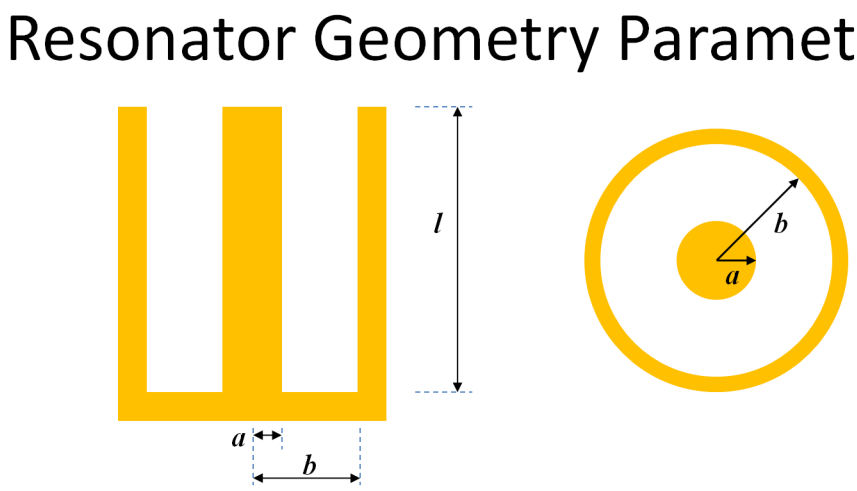

Figure 2.5: A schematic of resonator geometry parameters.

distribution inside the resonator. However, by leaving the length of the resonator as a free parameter, we can easily tune L_R and C_R to match the resonant frequency of our resonator.

The lumped element resistance of the resonator is slightly more complicated. In order to calculate the lumped element resistance, we must consider the distribution of current along the length of the resonator as well as the skin depth of the currents in the surface of the resonator body. Again, this gives the resistance one would expect based on current flowing in a coaxial cable, with the additional factor of $1/2$ to account for the fact that there is a node in the current at the open end of the resonator. For the lumped element resistance, we must also account for energy losses caused by currents in the "cap" at the closed end of the resonator. The outer and inner walls of the resonator contribute the first term of Equation 2.3 while the cap contributes the second term.

$$R_R = \frac{1}{2}\frac{1}{2\pi\sigma\delta}(\frac{1}{b}+\frac{1}{a})l + \frac{1}{2\pi\sigma\delta}\log[b/a] \tag{2.3}$$

Where σ is the conductivity of copper, and δ is the skin depth at the resonant frequency. In practice, the actual lumped element resistance is a bit higher due to oxidation and roughness of the copper surface. Resistive dissipation is the main energy loss mechanism in the resonator, however there are also losses associated with energy radiated into the far field as well as losses associated with energy transmitted into the coupling ports. These additional losses of energy act to increase the effective resistance of the resonator. Thus, Equation 2.3 represents a lower bound on the lumped element resistance.

Using these lumped element circuit values, the unloaded resonance frequency, f_0, and unloaded quality factor, Q_0, are simply those of a simple series LCR circuit.

$$f_0 = \frac{1}{2\pi\sqrt{L_R C_R}} \tag{2.4}$$

$$Q_0 = \frac{1}{R_R}\sqrt{\frac{L_R}{C_R}} \tag{2.5}$$

These equations are useful for designing a resonator with a specific resonant frequency. However, once the resonator has been fabricated, the f_0 and Q_0 are unlikely to exactly match these values. In order to calculate the lumped element capacitance and inductance for an actual resonator we leave the length, l as a free parameter and fit the experimentally observed f_0. In order to match the experimentally observed Q_0, we leave the lumped element resistance as a free parameter. The geometry of the

	a (mm)	b (mm)	l (mm)	f_0 (GHz)	Q_0 (unitless)	L_R (nH)	C_R (pF)	R_R (Ohm)
NFMM-AFM (Used in Ch. 3)	0.55	5.00	12.9	2.41	440	2.84	1.52	0.098
NFMM-STM (Used in Ch. 4)	0.95	3.00	12.4	2.51	580	1.43	2.82	0.039

Table 2.1: Lumped element circuit parameters for the unloaded equivalent circuit model. The geometry factors, a, b, and l describe the coaxial resonator and are the inner conductor radius, outer conductor radius, and effective length, respectively. The parameters a, b, f_0, and Q_0 are measured; l and R_R are fitting parameters; and L_R and C_R are calculated using Equations 2.1 and 2.2, respectively.

resonators used in Chapters 3 and 4, the experimentally observed f_0 and Q_0, as well as the calculated lumped element circuit values are displayed in Table 2.1.

Using the equivalent circuit model, the resonator can be treated as a damped, driven harmonic oscillator. The governing equation is the equation of motion for the current in a driven LCR circuit.

$$A_0 \cos(\omega t) = \ddot{I} + \frac{\omega_r}{Q}\dot{I} + \omega_r^2 I \tag{2.6}$$

Where A_0 is the driving amplitude, I is the current in the LCR circuit, $\omega_r = \frac{1}{\sqrt{LC}}$, $Q = \frac{1}{R}\sqrt{\frac{L}{C}}$, ω is the driving frequency, and t is time. The general solution to this equation is a phase shifted simple harmonic motion.

$$I(\omega, t) = I_i \sin(\omega t) + I_q cos(\omega t) = |I| \sin(\omega t - \phi) \tag{2.7}$$

Where I_i is the in-phase component of the current and I_q is the quadrature component of the current. Note that the term "in-phase" refers to the fact that at resonance this term generates a microwave signal at the output port of the resonator that is in phase with the driving signal at the input port. For $Q \gg 1$, we can approximate I_i,

I_q, $|I|$, and ϕ as follows.

$$
\begin{aligned}
I_i &= \frac{A_0}{4Q}\frac{1}{(\omega-\omega_r)^2+(\omega_r/2Q)^2} && (2.8)\\
I_q &= \frac{-A_0}{2\omega_r}\frac{(\omega-\omega_r)}{(\omega-\omega_r)^2+(\omega_r/2Q)^2} && (2.9)\\
|I| &= \frac{A_0}{2\omega_r}\frac{1}{\sqrt{(\omega-\omega_r)^2+(\omega_r/2Q)^2}} && (2.10)\\
\tan(\theta) &= -\frac{2Q}{\omega_r}(\omega-\omega_r) && (2.11)
\end{aligned}
$$

2.3 Microwave Circuitry

In order to measure the f_{r} and Q of the resonator, we use quadrature homodyne detection. The microwave components used in this detection scheme are shown in Figure 2.6, while the full microwave circuit is shown in Figure 2.7. The idea behind quadrature homodyne detection is to compare the microwave signal that has traversed a path including the resonator to a microwave signal that has traversed a path that is identical to the resonator path, but without the resonator. The difference in the amplitude and phase of these two signals is then used to obtain information about the state of the resonator. The beauty of this technique is that since the branch of the circuit containing the resonator is identical to the branch of the circuit without the resonator (the reference path), we do not need to work too hard to correct for the phase shift of the microwave signal that accrues as the signal propagates through the cables connecting the various components. Once we know the initial f_{r} and Q of the resonator, we will see that we can also use this technique to track shifts in f_{r} and Q

in real time.

The critical element of the homodyne detection circuit is the microwave mixer. A microwave mixer is a non-linear element that multiplies two microwave signals together in real time. In an ideal mixer, the mixer output is composed of signals at the sum and difference frequencies of the two input signals.

$$A_0 \sin(\omega_0 t + \phi_0) * A_1 \sin(\omega_1 t + \phi_1) = \frac{A_0 A_1}{2}[\cos((\omega_0 - \omega_1)t + (\phi_0 - \phi_1)) - \cos((\omega_0 + \omega_1)t + (\phi_0 + \phi_1))] \quad (2.12)$$

When both of the inputs to the microwave mixer are at the same frequency (as is the case in homodyne detection), the mixer output has a DC component and a component at twice the input frequency. We are interested in using the microwave mixers in order to convert the information carried by the microwave signals down to a DC signal, so that we can easily measure it using an analog to digital (A/D) converter. The output of the microwave mixer is therefore sent through a low pass filter in order to remove the high frequency component. The output of the filter is then $1/2 A_0 A_1 \cos(\phi_0 - \phi_1)$. If the amplitude and phase of one of the signals are known, then the mixer output provides information about the amplitude and phase of the second signal. However, the output of a single mixer does not contain all of the information about the second signal. For example, if the two input signals are out of phase by 90 degrees, then the mixer output is always zero. We could then deduce the relative phase of the two signals is 90 degrees, but we could say nothing about their

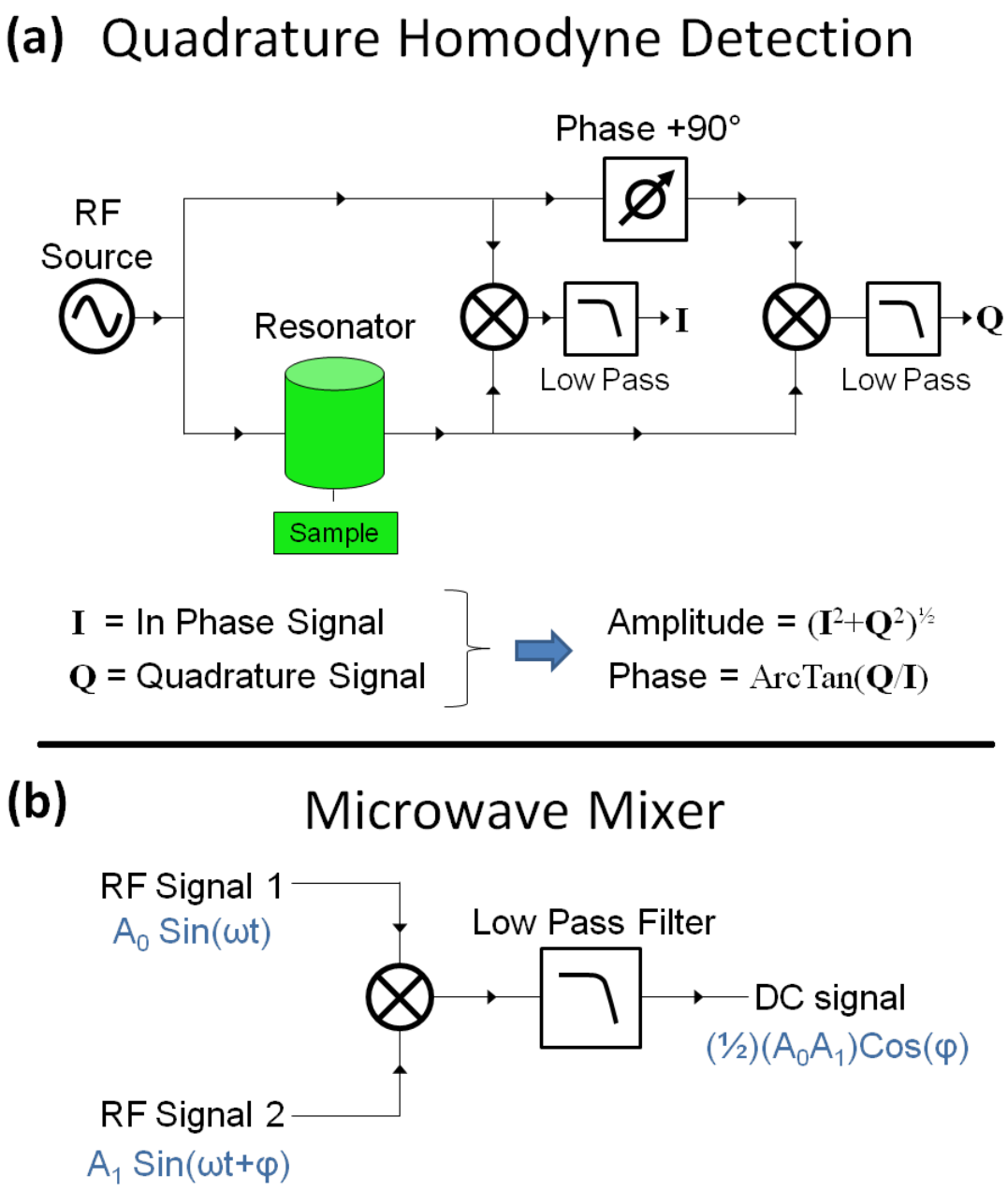

Figure 2.6: Part (a) shows a schematic of the microwave components used to perform quadrature homodyne detection. Part (b) shows the microwave mixer alone. A microwave signal is split between two paths, one path passes through the resonator and the other is used as a reference signal. Two microwave mixers are used in quadrature in order to capture both the in-phase and 90 degree phase shifted components of the signal coming from the resonator.

amplitudes.

In order to obtain all of the information about the second signal, we need a second mixer. One of the inputs to the second mixer is phase shifted by 90 degrees. The output of the second mixer is then $1/2 A_0 A_1 \sin(\phi_0 - \phi_1)$, providing complementary information to the first mixer. The outputs of these two mixers are called the in phase (I_{mix}) and quadrature (Q_{mix}) signals.

$$I_{mix} \propto A_1 \cos(\phi) \tag{2.13}$$

$$Q_{mix} \propto A_1 \sin(\phi) \tag{2.14}$$

Where ϕ is defined as $\phi_0 - \phi_1$. The amplitude and phase of the second signal (in this case the signal from the resonator) can then be easily calculated using these two DC signals.

$$A_1 = \sqrt{I_{mix}^2 + Q_{mix}^2} \tag{2.15}$$

$$\tan\phi = Q_{mix}/I_{mix} \tag{2.16}$$

In practice the microwave circuit contains a few extra components. The full microwave circuit is shown in Figure 2.7. The signal from the RF source is split into two branches using a directional coupler, with the majority of the power directed towards the resonator. Following the branch containing the resonator, we have only

an amplifier, the microwave resonator, and some coaxial cables. The power of the microwave signal at the output of the amplifier is 8.6 dBm. The resonator is only weakly coupled to the transmission lines (this weak coupling maximizes the Q of the resonator), so the power output from the resonator is $\sim$25 dB less than the power at the resonator input.

Following the other branch from the directional coupler, we encounter a delay line and a phase shifter. The delay line is a length of cable chosen to match the total length of cable in the branch containing the resonator. The function of this delay line is to make the electrical length (the number of wavelengths in a cable) of the two branches the same. If the two branches have different lengths, then the number of wavelengths that fit into each path will be dependent on the driving frequency. As the driving frequency is varied, this would lead to a phase shift between the signals at the end of the two paths. Ideally, we would like relative phase at the end of the two paths to tell us exclusively about the phase of the excitation of the resonator. However if the electrical lengths of the two branches are not the same, then the relative phase also contains information about the difference in cable lengths. Of course, in practice it is difficult to match the path lengths exactly. The small path length difference results in a small phase shift between the signal from the resonator branch and the signal from the reference branch. In order to compensate for this phase shift, we add a variable phase shifter into the circuit.

According to the equivalent circuit model described in Section 2.2, we can understand the resonator by treating it as an LCR circuit. Therefore, below its resonance frequency the inductor acts as a short and the resonator primarily acts as a capaci-

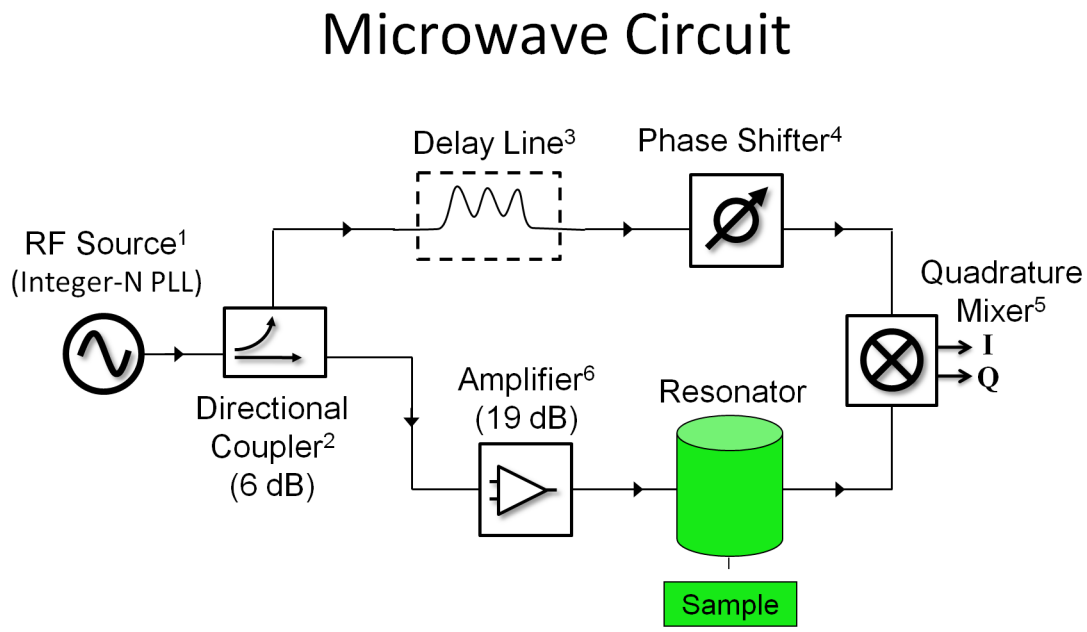

Figure 2.7: A schematic of the microwave components of the microscope. The outputs of the microwave mixer are fed to an analog to digital converter built into the microscope controller, which uses this information to track the f_r and Q of the resonator.

tor. In this case, the signal coming out of the resonator should lead the signal going into the resonator and we should see a phase shift -90 degrees. When driving the resonator significantly above the resonant frequency, the resonator acts primarily like an inductor and we see a phase shift of +90 degrees. At resonance, the resonator acts as a real impedance, producing no phase shift. The width of the transition is given by the bandwidth of the resonator, which is simply $\Delta f = f_r/Q$.

Figure 2.8 (a) shows the signals from the IQ mixer as the microwave driving frequency is swept through the resonant frequency of the microwave resonator. Figure 2.8 (b) shows the amplitude and phase of the signal coming from the resonator calculated using Equations 2.15 and 2.16. The initial f_r and Q can be found using any of these curves. The f_r is the frequency corresponding to the maximum of the in-phase mixer signal, the maximum of the amplitude, and the zero crossings of the quadrature mixer signal and the phase. The bandwidth of the resonance can also be calculated based on any of these curves. For our case, we calculate the bandwidth by finding the frequency range between the maximum and the minimum of the mixer quadrature signal. The Q of the resonator is then simply the resonant frequency divided by the bandwidth. For the resonator shown in Figure 2.8, the f_r of the resonator is 2.506 GHz and the Q is 440.

It is possible to calculate the f_r and Q as a function of the tip-sample interaction by sweeping the driving frequency and measuring these resonance curves for each tip position and for each sample, however when scanning the surface of a sample in real time, this process would be very slow. In order to measure f_r and Q in real time, we use a two step approach. The first step is to use a feedback loop to keep

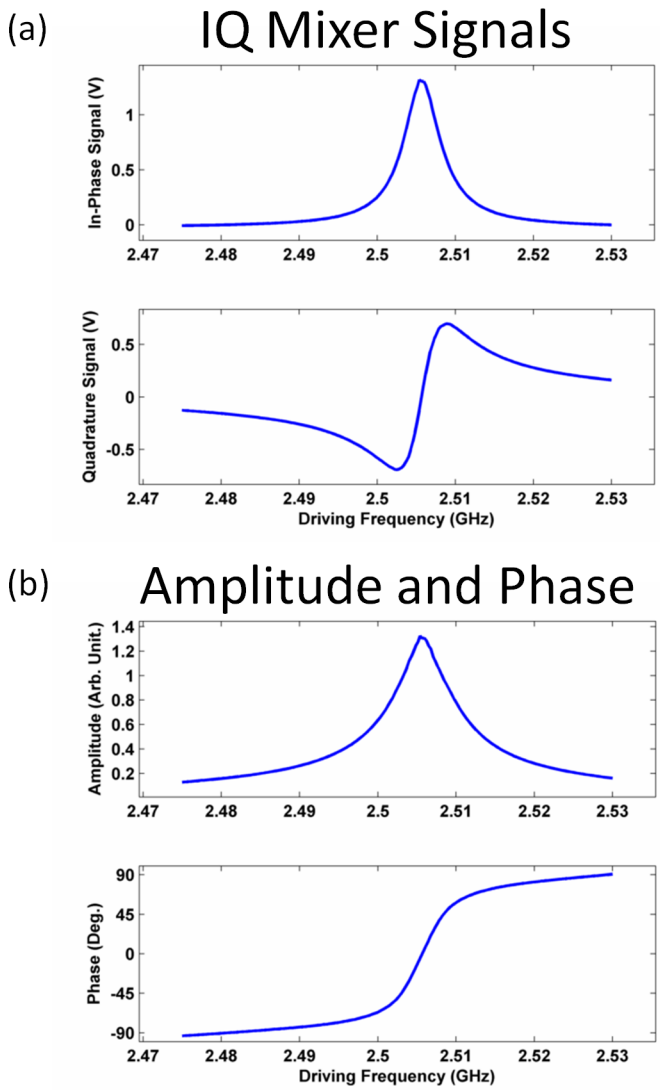

Figure 2.8: Microwave frequency sweeps for the unloaded (no sample near the tip) resonator. Part (a) shows the in-phase (I) and quadrature (Q) signals from the IQ mixer as the driving frequency is swept. Part (b) shows the corresponding amplitude and phase of the signal coming from the resonator calculated using Equations 2.15 and 2.16. Bases on these curves, the f_r of the resonator is 2.506 GHz and the Q is 440.

the microwave driving frequency near the resonance frequency. This feedback loop uses the quadrature mixer output as an input to a PID controller. The output of the PID controller is then used to control the driving frequency. This keeps the driving frequency close to the resonant frequency. Unfortunately, the microwave frequency source does not have infinite frequency resolution (it is an integer-N PLL with a channel spacing of ∼1kHz), so there is always a small deviation of the driving frequency from the resonant frequency. Fortunately, we can calculate the f_r and Q based on the microwave mixer signals for small deviations of the driving frequency from the resonant frequency.

$$f_r = f\left(1 - \frac{f_0^2}{f^2}\frac{V_0}{2Q_0}\frac{V_q}{V_i^2 + V_q^2}\right) \tag{2.17}$$

$$Q = Q_0\frac{f_0^2}{f^2}\frac{V_i^2 + V_q^2}{V_0 V_i} \tag{2.18}$$

Where V_i is the in-phase microwave mixer signal, V_q is quadrature microwave mixer signal, Q_0 is the unloaded quality factor of the resonator, f_0 is the unloaded resonant frequency, f is the driving frequency, and V_0 is the amplitude of the in-phase mixer signal when driving the unloaded resonator at resonance.

Chapter 3

FMR using NFMM-AFM

3.1 Abstract

In this chapter we explore the possibility of using the open ended coaxial resonator geometry to perform Ferromagnetic Resonance (FMR) spectroscopy. The coaxial resonator geometry is excellent for high spatial resolution characterization of the dielectric properties of materials.[2, 3, 5, 10] If it is also possible to use this geometry to characterize the magnetic properties of materials, then the utility of the coaxial resonator geometry would be considerably expanded. Since NFMM is a microwave technique, we choose to characterize the magnetic properties of our sample using FMR spectroscopy.

As an example system, we explore a single crystal Gallium doped Yttrium Iron Garnet ($Ga_xY_3Fe_{5-x}O_{12}$, or Ga:YIG) disk. YIG is a ferrimagnetic insulator that is very popular in microwave devices due to is relatively low spin damping. This low spin damping allows for narrow FMR resonance linewidths, which in turn allow the fabrication of narrow bandwidth tunable microwave generators, bandpass and bandstop filters, as well as phase shifters.

FMR absorption spectra are obtained by positioning the probe tip of the microwave resonator over the Ga:YIG disk, sweeping a DC magnetic field oriented normal to the disk plane, and recording the absorption of microwave energy by the

sample. Measurement of the FMR absorption spectrum is then repeated with the tip positioned over many different parts of the sample.

In order to identify the features of the absorption spectra, we build a model the RF magnetic field produced by the probe tip and perform simulations of the micromagnetic dynamics using the RKMAG software.

It is found that the absorption lines of the FMR spectra correspond to the excitation of magnetostatic spin wave modes. The resonance field and intensity of the microwave absorption for any given spin wave mode depend on the tip position, providing information about the magnetic properties of the sample.

3.2 Introduction to FMR

FMR spectroscopy is a fundamental tool in the investigation of magnetic materials, providing information about the crystalline anisotropy, shape anisotropy, magnetic homogeneity, and dampling of spin precession inside a ferromagnetic sample[38, 39]. FMR spectroscopy is based on the resonant absorption of microwaves by spins in a ferromagnetic sample[40]. The resonance condition is met when the microwave photon energy matches the electron energy level splitting caused by the effective magnetic field inside the sample.

Before considering the case of a spin in a ferromagnetic sample, it is instructive to consider the resonance of a single free spin. For an electron spin in a uniform applied magnetic field, there is a splitting between the energy levels of the up and down state.

This energy gap is called the Zeeman energy, E_Z.

$$E_Z = g_e \mu_B H \tag{3.1}$$

Where g_e is the electron g-factor ($g_e \approx 2$), μ_B is the Bohr magneton, and H is the applied magnetic field. If the energy of an incident photon matches the level splitting, there can be resonant absorption of the photon by the spin.

$$\hbar\omega \;\; = \;\; g_e \mu_B H \tag{3.2}$$

Where ω is the angular frequency of the photon and $\hbar$ is the Plank constant. The resonance frequency for non-interacting spins is therefore a simple linear function of the applied field.

$$\omega = \gamma H \tag{3.3}$$

Where γ is the gyromagnetic ratio ($\gamma \approx 2.8$ MHz/Oe). When considering a ferromagnetic sample, the field that a spin inside the sample sees is significantly more complicated.

$$\mathbf{H}_{eff} = \mathbf{H}_0 + \mathbf{H}_{exch} + \mathbf{H}_d + \mathbf{H}_a \tag{3.4}$$

Where $\mathbf{H}_{eff}$ is the effective magnetic field, $\mathbf{H}_0$ is the external applied field, $\mathbf{H}_{exch}$ is the effective field due to the exchange interaction between adjacent spins, $\mathbf{H}_d$ is

the field due to the long range dipolar interaction between spins within the sample, and $\mathbf{H}_a$ is the anisotropy field due to coupling between a spin and the crystal lattice in which it is embedded (spin-orbit coupling). The equation of motion for a spin inside of a ferromagnetic sample can be captured phenomenologically by the Landau-Lifshitz-Gilbert equation[41, 42].

$$\frac{\mathrm{d}\mathbf{M}}{\mathrm{d}t} = -\gamma \mathbf{M} \times \mathbf{H}_{eff} - \beta \frac{\gamma}{M} \mathbf{M} \times (\mathbf{M} \times \mathbf{H}_{eff}) \tag{3.5}$$

Where $\mathbf{M}$ is the magnetic moment of a spin, $\mathbf{H}_{eff}$ is the effective magnetic field, and β is a dimensionless parameter that describes the damping of spin precession. If a spin is not aligned with a static magnetic field, the first term on the right hand side of this equation describes the precession of the spin around the static field. The second term describes the tendency of this precession to decay such that the spin eventually aligns with the static field.

Calculation of the magnetic resonance frequencies for an arbitrarily shaped sample is in general non-trivial. However for some high-symmetry geometries the resonance condition for the uniform precession mode (all spins precessing with the same phase) are well known[40]. The resonance equations for these cases are presented in Figure 3.1.

There are two ways of performing FMR spectroscopy. First, one may fix an applied DC magnetic field and sweep the microwave frequency. Second, one may fix the microwave frequency and sweep an applied magnetic field. The latter approach is usually preferred due to the higher sensitivity obtainable using resonant microwave

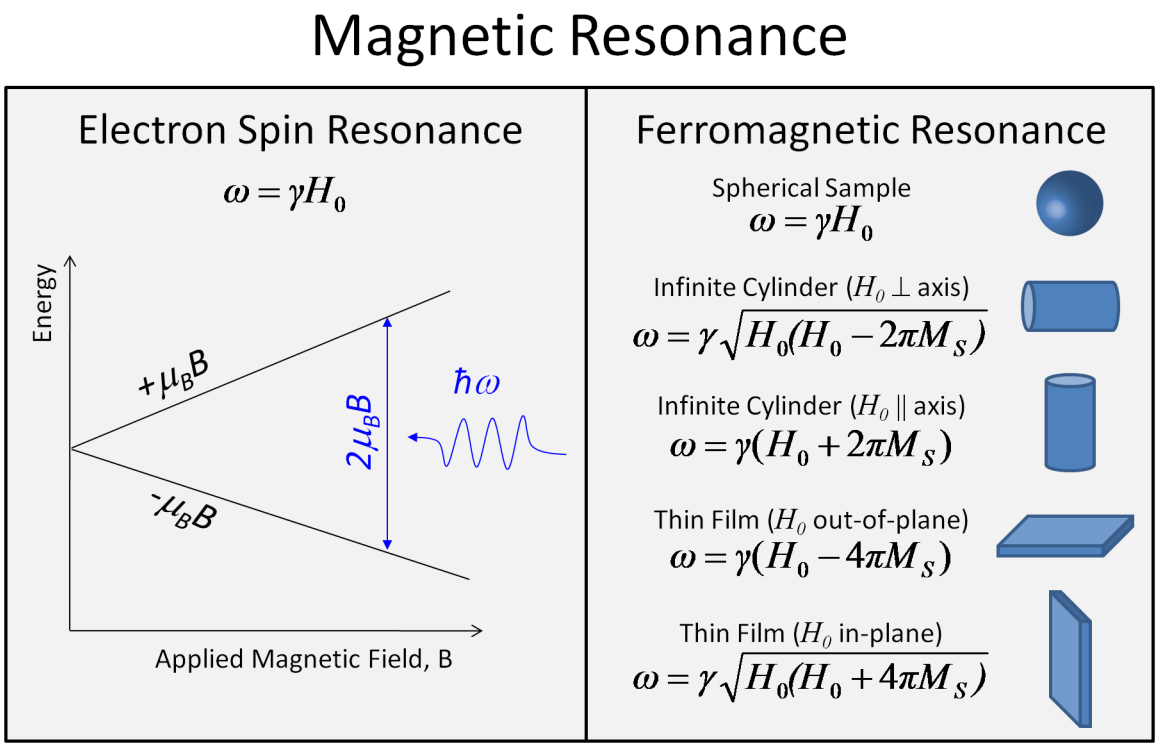

Figure 3.1: On the left, the resonant frequency of non-interacting spins is presented. Resonant absorption of photons can occur when the spacing between electron energy levels matches the photon energy. In a magnetic material, the resonance condition is modified due to the demagnetizing field created by the sample magnetization. On the right, the resonant frequency of the uniform precession mode is presented for some high-symmetry cases. These equations assume that the crystalline anisotropy is zero and that the sample magnetization is aligned with the applied DC magnetic field, H_0.

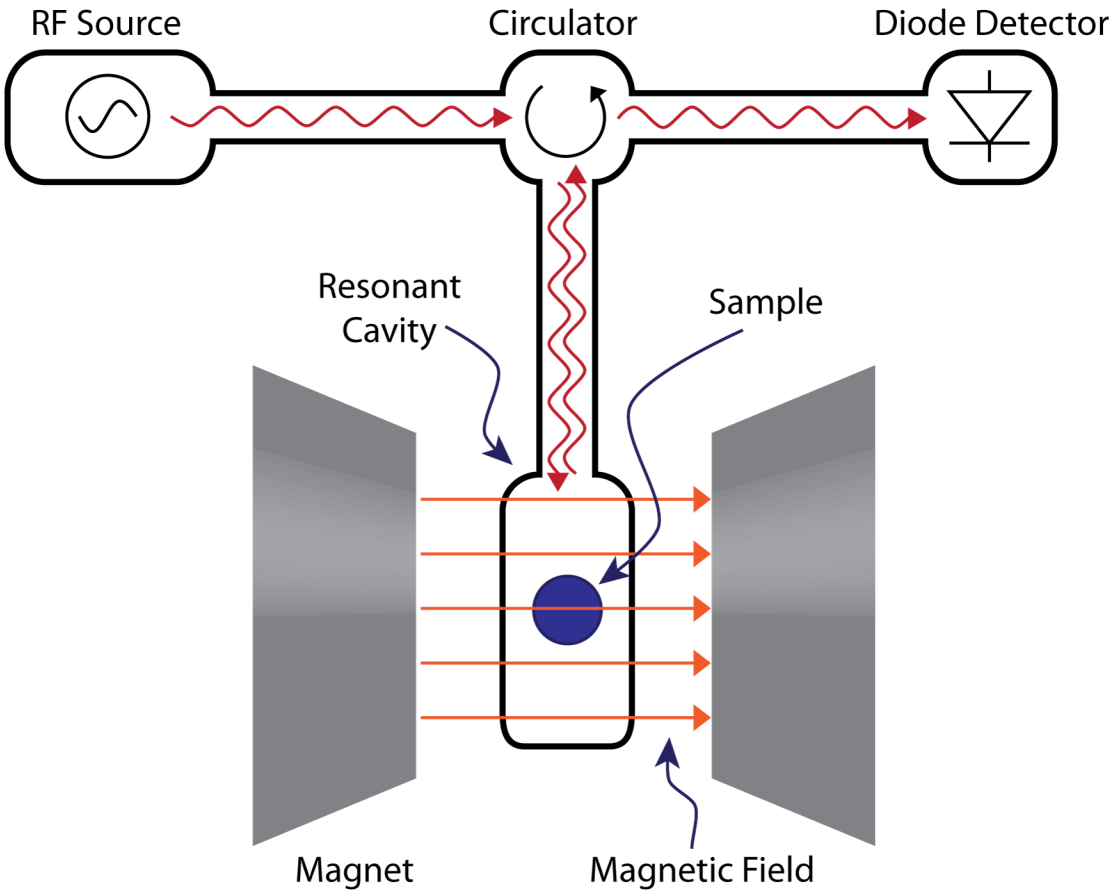

Figure 3.2: Schematic of a traditional FMR spectroscopy measurement. The sample is loaded into a resonant microwave cavity, the magnetic field is swept, and the absorption of microwaves by the sample is measured using a diode detector.

cavities and the relative simplicity of sweeping DC magnetic fields compared to sweeping the microwave frequency.

Traditional FMR measurements are performed by placing a sample into a waveguide or resonant microwave cavity, sweeping an applied magnetic field, and measuring the absorption of microwaves by the sample. A schematic of this configuration is presented in Figure 3.2. The results of these traditional FMR measurements give an average of the properties of the entire sample. In order to improve the spatial resolution of this technique, we place the sample outside of a resonant cavity and then use

near field microwave microscopy to couple the resonator to the sample.

Several different research groups have explored the possibility of performing scanning FMR spectroscopy using a NFMM. The first such experiment used an aperture in the wall of a resonant cavity in order to couple microwaves into a colossal magnetoresistive thin film placed outside of a resonant microwave cavity[43]. This was followed quite closely by the development of a loop-type probe at the end of a coaxial resonator[44, 26]. The spatial resolution and sensitivity of the aperture approach has since been refined by using a small slit aperture[47]. The loop type probe has also been used more recently in a non-resonant geometry, allowing for broadband microwave characterization[45, 46].

The experimental work most similar to the FMR spectroscopy presented in this dissertation was done by Toshu An et al. [48]. In An's work, FMR absorption spectra were obtained at various points over a ferrimagnetic disk using an open ended coaxial probe operating at 10 GHz. The main experimental difference between An's work and the work presented here is in the direction of the applied magnetic field; in An's work the magnetic field is applied in the in-plane direction of the sample, while in our work the magnetic field is applied out-of-plane. This results in a different set of spin wave modes becoming excited in the sample, leading to different patterns of RF energy absorption across the sample. An's work also used an open-ended transmission line, while our experiment used a coaxial resonator. The use of resonant detection allowed us to probe a smaller sample and achieve higher sensitivity. We have also performed extensive modeling of the RF magnetic field around the probe tip and the interaction of this field with the sample, as discussed in section 3.6.

3.3 NFMM-AFM System

Figure 3.4 shows a picture of the microscope used to perform scanning FMR. The system is designed as a hybrid between a NFMM and a shear mode AFM. The most interesting data is generally obtained in the microwave data channels, which contain the f_r and Q of the microwave resonator.

The f_r and Q of the microwave resonator are very sensitive to the tip-sample distance. To avoid any kind of convolution between the topography of the sample surface and the microwave channels, shear mode AFM is used to maintain a constant soft contact between the tip and the sample surface. The shear mode AFM is implemented by gluing the tip to one tine of a quartz tuning fork, which can be seen in Figure 3.3. The tuning fork oscillation is in the plane of the sample.

Figure 3.3 shows an image of the end of the microwave resonator. The probe tip extends from a small hole in the end of the resonator. A quartz tuning fork is glued to the end of the tip in order to form a shear force atomic force microscope (AFM). A Hall probe is mounted near the tip in order to measure the out-of-plane magnetic field near the tip.

The full NFMM-AFM microscope can be seen in Figure 3.4. The resonator is mounted on fixture that has an integrated motorized micrometer and a piezoelectric positioner. These are used for sample approach and topography feedback, respectively. The sample under test is mounted on a Delrin disk (not shown), which rests on top of the AC magnetic field coil support. A permanent magnet is mounted below the sample in order to apply DC magnetic field that is near the resonance field for

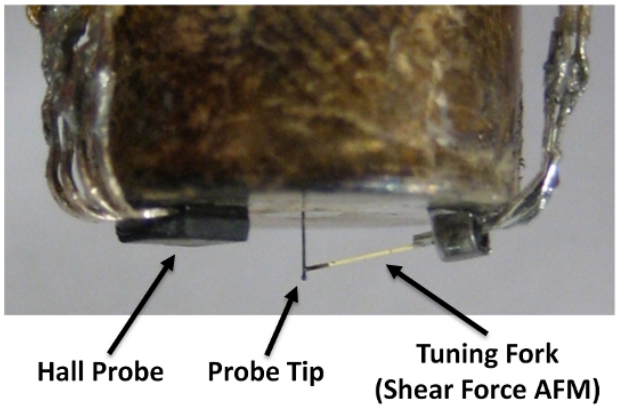

Figure 3.3: The probe end of the microwave resonator. A Hall probe mounted near the tip allows measurement of the magnetic field along Z direction (out of the sample plane). The probe tip is 2 mm long and made of tungsten. A small ball is formed at the end of the tip by electrical arcing before it is mounted in the resonator. The tip is glued to one tine of a quartz tuning fork in order to form a shear mode AFM.

the sample under test. A large electromagnet surrounding the permanent magnet is used to sweep the DC magnetic field. The electromagnet produces a magnetic field of 40 Gauss per Ampere of current. This coil is not water cooled, so heating is an issue if large currents are applied. The practical current limit is ± 5 Amps, allowing the DC field to be swept by 400 Gauss. A smaller wire coil inside of the main coil is used to modulate the DC field in order to perform lock-in measurements. The sample is scanned along with the electromagnets using a scanning stage actuated by motorized positioners. The travel range of the XY stage is $1/2$ inch in either direction, with a positioning accuracy of one micron. An optical microscope is used to view the position of the tip over the sample.

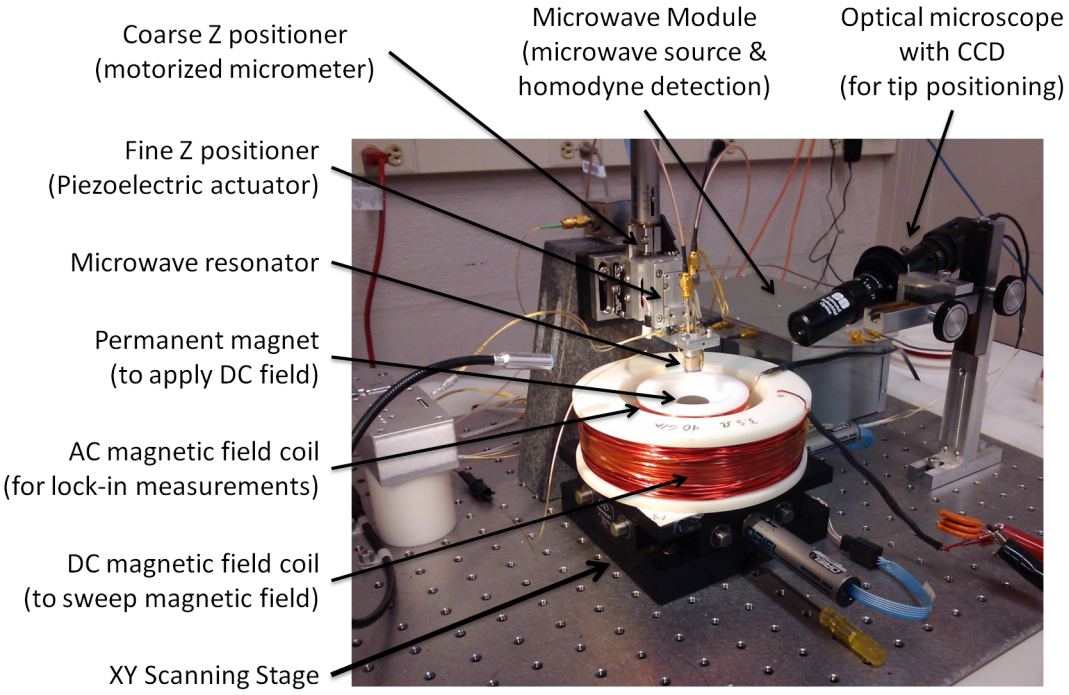

Figure 3.4: The NFMM-AFM used to perform scanning FMR spectroscopy. The coarse positioners in the X, Y, and Z directions each have a travel range of 1/2 inch. The fine Z positioner (12 μm travel) is used to maintain soft contact between the tip and the sample surface once the surface has been approached using the coarse Z positioner.

3.4 Scanning FMR Experiment Details

As the DC magnetic field is swept through a field at which FMR occurs, the spins in the sample undergo resonant absorption of microwaves. This absorption of microwave power by the sample decreases the Q of the resonator. At resonance, the in-phase microwave mixer output is proportional to the Q of the resonator. We can therefore calculate the power dissipated by the sample based on the in-phase microwave mixer output. In practice, we measure the derivative of the in-phase mixer signal with respect to the applied field using a lock-in amplifier (model SR830), and then integrate to get the power dissipated in the sample.

$$P_{abs} \propto \int \frac{dI_{mix}}{dH} dH \tag{3.6}$$

Where P_{abs} is the power absorbed by the sample, dI_{mix}/dH is the output of the lock-in measuring the in-phase mixer signal, and H is the applied magnetic field. For a derivation, see A.1. The information about the sample is carried by the field at which resonance occurs and the shape of the absorption peak, therefore it is not critically important to calibrate the constant of proportionality. Instead, the power absorbed by the sample is displayed in arbitrary units.

Figure 3.5 shows a schematic of the probe tip, sample, and magnetic field configuration for this experiment. A permanent magnet mounted below the sample provides a DC magnetic field of ∼1000 Oe oriented out of the sample plane. An electromagnet is then used to sweep the magnetic field from 1,000 to 1,150 Oe. This field range captures all of the FMR absorption lines that are above the noise floor of our system. A

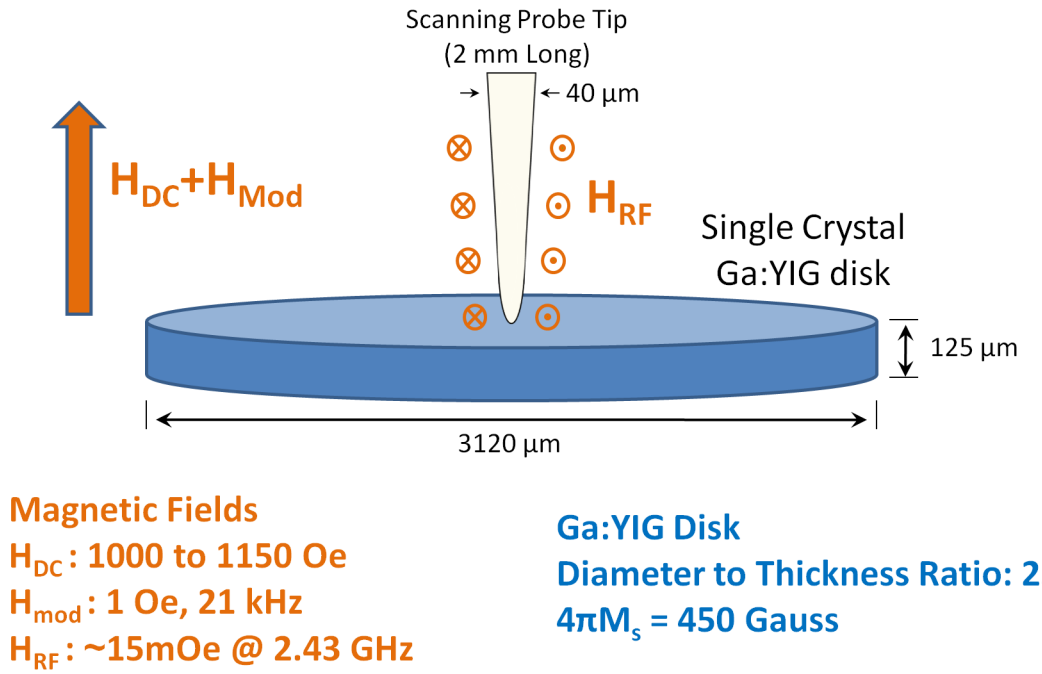

Figure 3.5: Schematic of magnetic field, sample, and probe tip configuration for scanning near-field FMR spectroscopy.

second coil is used to add a small (1 Oe) modulation to the out-of-plane DC magnetic field at 21 kHz. This modulation allows us to perform lock-in measurements on the microwave mixer outputs.

At each location where an FMR spectrum is to be recorded, the sample is laterally positioned beneath the probe tip and the tip is brought into contact with the sample surface using motorized actuators. When the tip reaches the sample surface, the oscillation of the tuning fork is damped due to the mechanical interaction between the vibrating tip and the sample surface. A constant contact force between the tip and the sample is maintained by using the amplitude of the tuning fork oscillation as a feedback signal for PID controller. The PID controller outputs a signal to a piezoelectric actuator that moves the tip up or down in order to maintain a constant

tuning fork oscillation amplitude. The piezoelectric actuator has a travel range of 12 μm in the Z direction, which is sufficient to compensate for any drift that might occur during a field sweep.

Once the tip is in contact with the sample, the DC magnetic field is swept by driving a current through the larger electromagnet pictured in Figure 3.4. As the magnetic field is swept, several channels of data are recorded. Among these channels are the environment temperature, the Hall probe output voltage (which is proportional to the out of plane DC magnetic field), the microwave in-phase and quadrature mixer signals, and lock-in measurements on the microwave in-phase and quadrature mixer signals.

Lock-in amplification is used in order to increase the signal to noise level of the measurements of the mixer in-phase and quadrature signals. The reference signal for the lock-in measurements is the voltage across the small modulation coil, which is a sinusoidal signal at 21 kHz.

3.5 Scanning FMR Data

Figure 3.6 shows two absorption spectra obtained using the method described in section 3.4. The spectra taken over different parts of the sample look quite different.

Figure 3.7 shows the absorption of microwave power as the tip is scanned over the disk from bottom to top. The field at which any given absorption peak occurs shifts as the tip is scanned over the sample. The intensity of absorption also changes.

Figure 3.8 shows the intensity of microwave absorption as a function of tip position

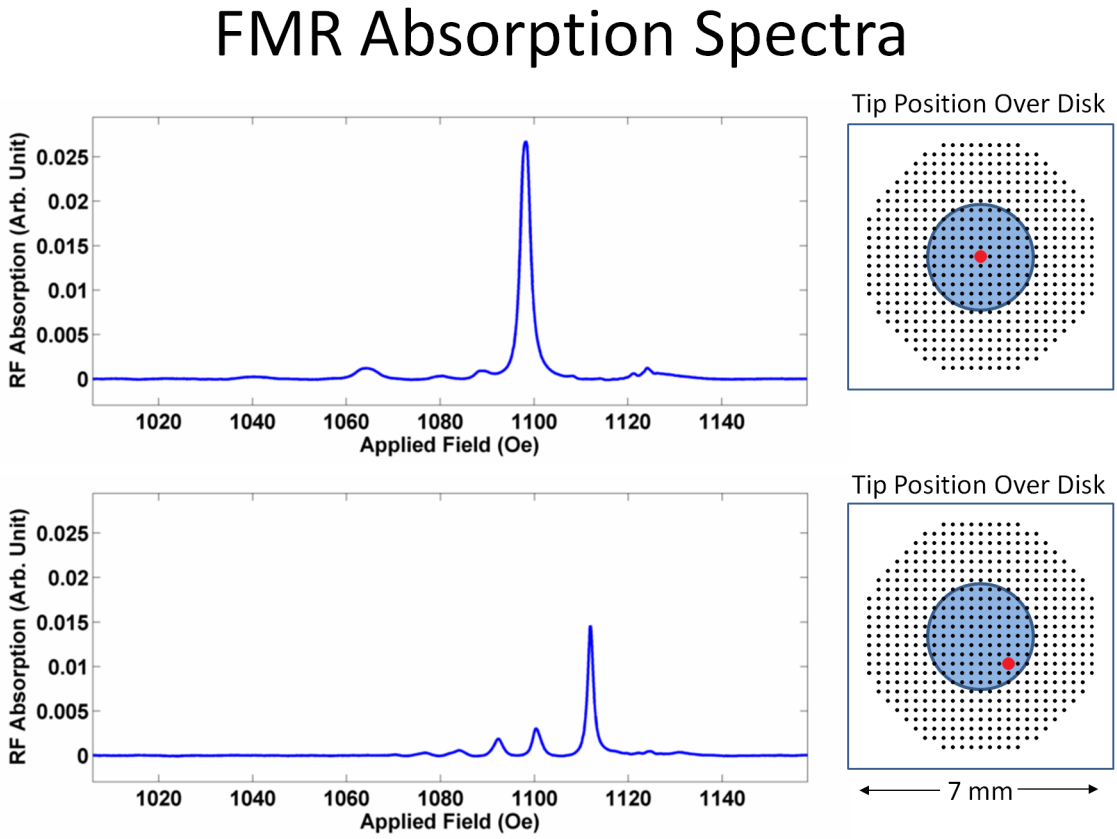

Figure 3.6: On the left are FMR absorption spectra measured with the tip positioned in two different locations over the sample. On the right, the location of the tip over the sample is marked for each spectrum. The tip position is indicated in red, the disk location is indicated in blue, and the grid of all points where FMR spectra were collected is marked in black.

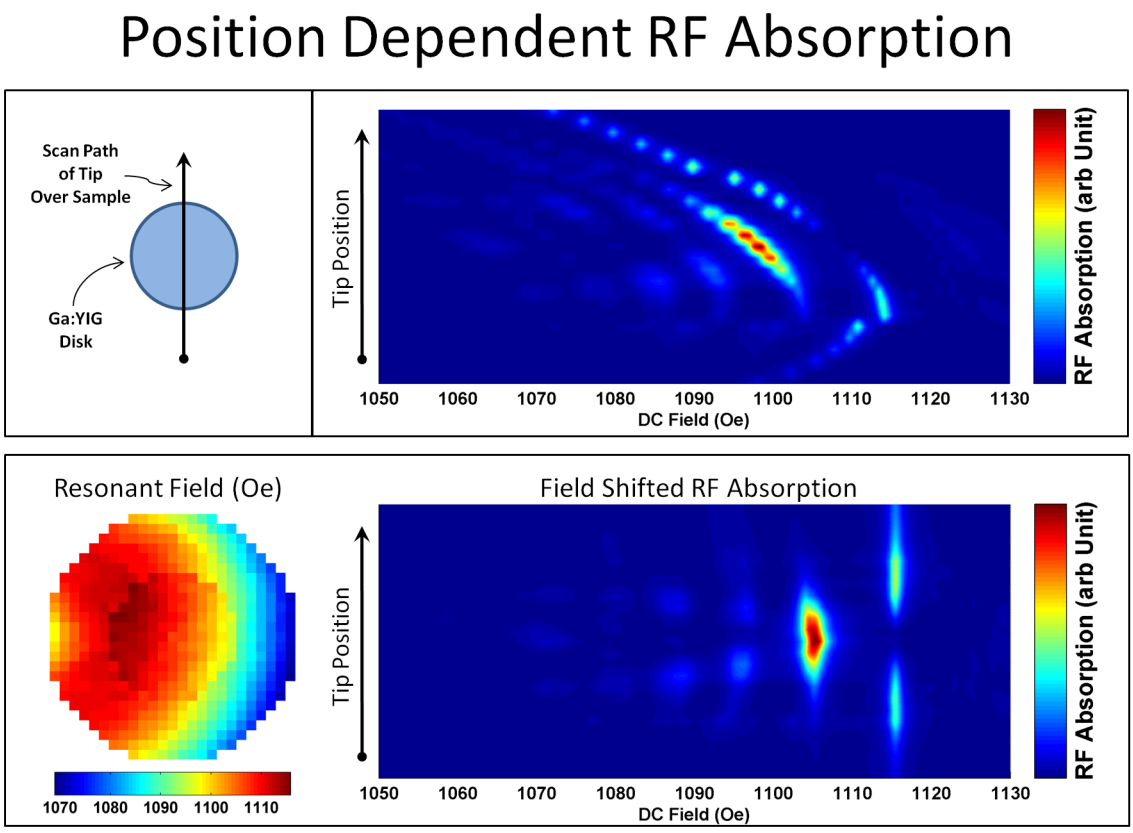

Figure 3.7: FMR absorption spectra as a function of tip position. At the top left, a schematic of the scan path of the tip across the disk is presented. At the top right, the corresponding FMR spectra are displayed. Both the resonant field of any given peak and the intensity of absorption change as the tip is scanned over the disk. On the bottom left, the resonant field for the absorption peak occurring at the highest applied magnetic field is shown. At the bottom right, a field offset has been added to each of the spectra in order to align the peaks and make the variation in the intensity of absorption as a function of tip position more clear.

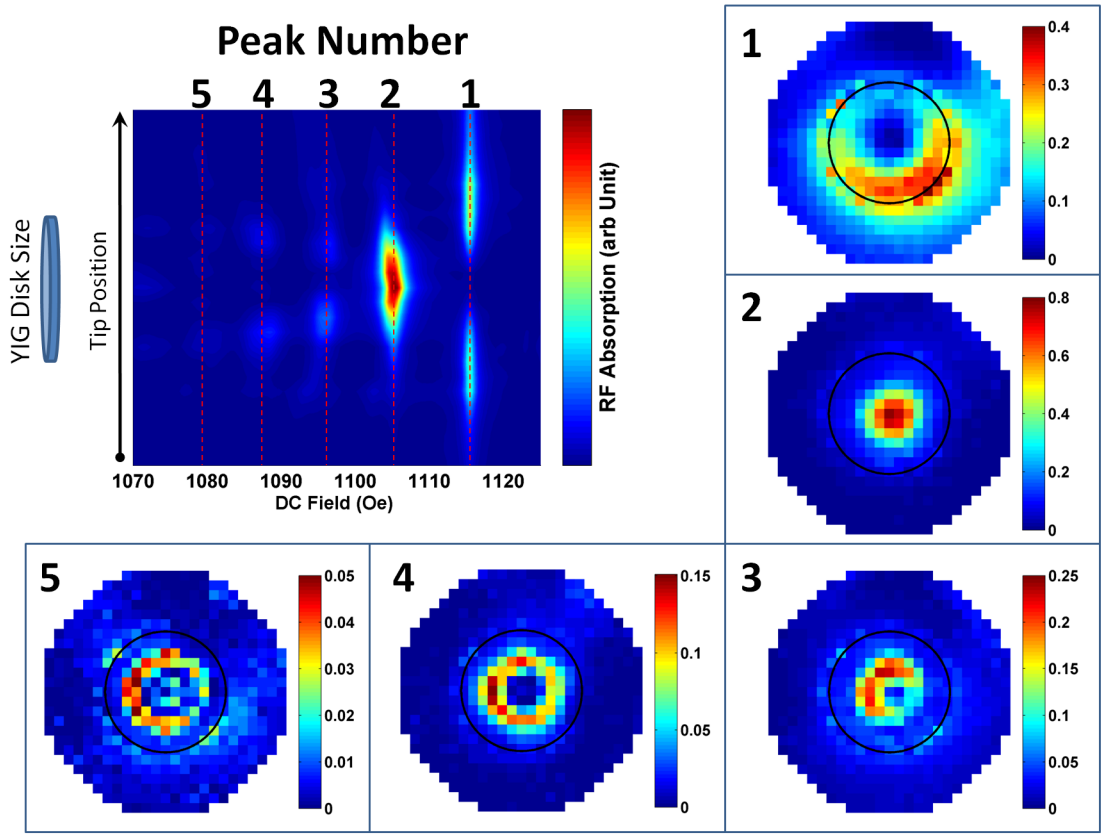

Figure 3.8: The intensity of each FMR absorption peak as a function of tip location. The black circle in each numbered plot indicates the perimeter of the Ga:YIG disk.

for all of the points scanned. For each peak, the local maximum of the specified absorption line is plotted.

3.6 Modeling and Simulation

In order to identify the meaning of the RF energy absorption lines, we performed simulations of the experiment using the RKMAG software[36]. This software breaks the Ga:YIG disk down into many small cells[1]. Each cell is assigned a single magnetic moment that represents the magnetization within the volume of the cell. As long as

[1]We used a cell size of 50 x 50 μm in the XY plane and 125 μm in the Z direction. The total number of cells in the disk is ~3,000.

the motion of all of the spins within a cell are very similar, this is a reasonable approximation. The Landau-Lifshitz-Gilbert equation (Equation 3.5) is then linearized using perturbation theory under the assumption that the sample magnetization only undergoes small deviations from its equilibrium configuration. Using the linearized Landau-Lifshitz-Gilbert equation, RKMAG then solves for the eigenmodes of the coupled cells. This procedure is explained in detail in references and [36, 37].

This technique is highly advantageous for the case of a scanning FMR experiment because one must only solve for the eigenmodes once, then one can calculate the absorption of microwave energy as a function of microwave frequency for any microwave field configuration (meaning any tip geometry or position). The disadvantage of this method is that it cannot be used for high-power microwave excitations where the spin dynamics are non-linear.

One alternative to this eigenvalue approach is to simulate the spin dynamics by numerical integration of the Landau-Lifshitz-Gilbert equation. This alternative is very computationally expensive because one must run the simulation for enough time for a steady state to be established. One must then re-run the entire simulation for each tip position over the sample and each applied DC field. The advantage of numerical integration is that it can be used for arbitrarily large microwave powers and for an arbitrary initial configuration of the spins within the sample. One could also simulate more complicated spin dynamics, such as those resulting from a pulsed DC or microwave field.

3.6.1 Model of the RF Magnetic Field

Once the eigenmodes of the disk have been calculated using RKMAG, it is necessary to specify the microwave field intensity and direction at each cell within the disk in order to calculate to absorption of microwave energy. In order to do this, we built an analytic approximation of the RF magnetic field generated by the tip. The general procedure in this approximation is as follows. First, we approximate that the charge along the length of the tip is uniform. Since the length of the tip is much less than the free space wavelength, the uniform charge distribution is a reasonable approximation[2]. The charge per unit length on tip is approximated by calculating the charge on the center conductor of a coaxial capacitor of the same dimensions as the resonator, containing the same amount of energy as the driven resonator. The uniform charge distributed along the length of the tip induces an image charge in the shielding structure at the end of the resonator. This shielding structure is approximately a plane, and can therefore be removed from the problem by replacing it with the image charge of the tip, creating a short dipole antenna. This scheme is illustrated in Figure 3.9. The time varying charge distribution on the tip creates a current along the length of the tip. Once this current has been calculated, we make the magnetostatic approximation (again, a reasonable approximation because of the small tip size compared to the free space wavelength) and integrate the Biot-Savart law to obtain the magnetic field in the region below and around the tip.

In cylindrical coordinates (r, θ, z) with the effective antenna in Figure 3.9(b)

[2]The length of the tip is $\sim$2 mm, while the free space wavelength at 2.4 GHz is 12.5 cm, which means the tip is 1/63 of the free space wavelength.

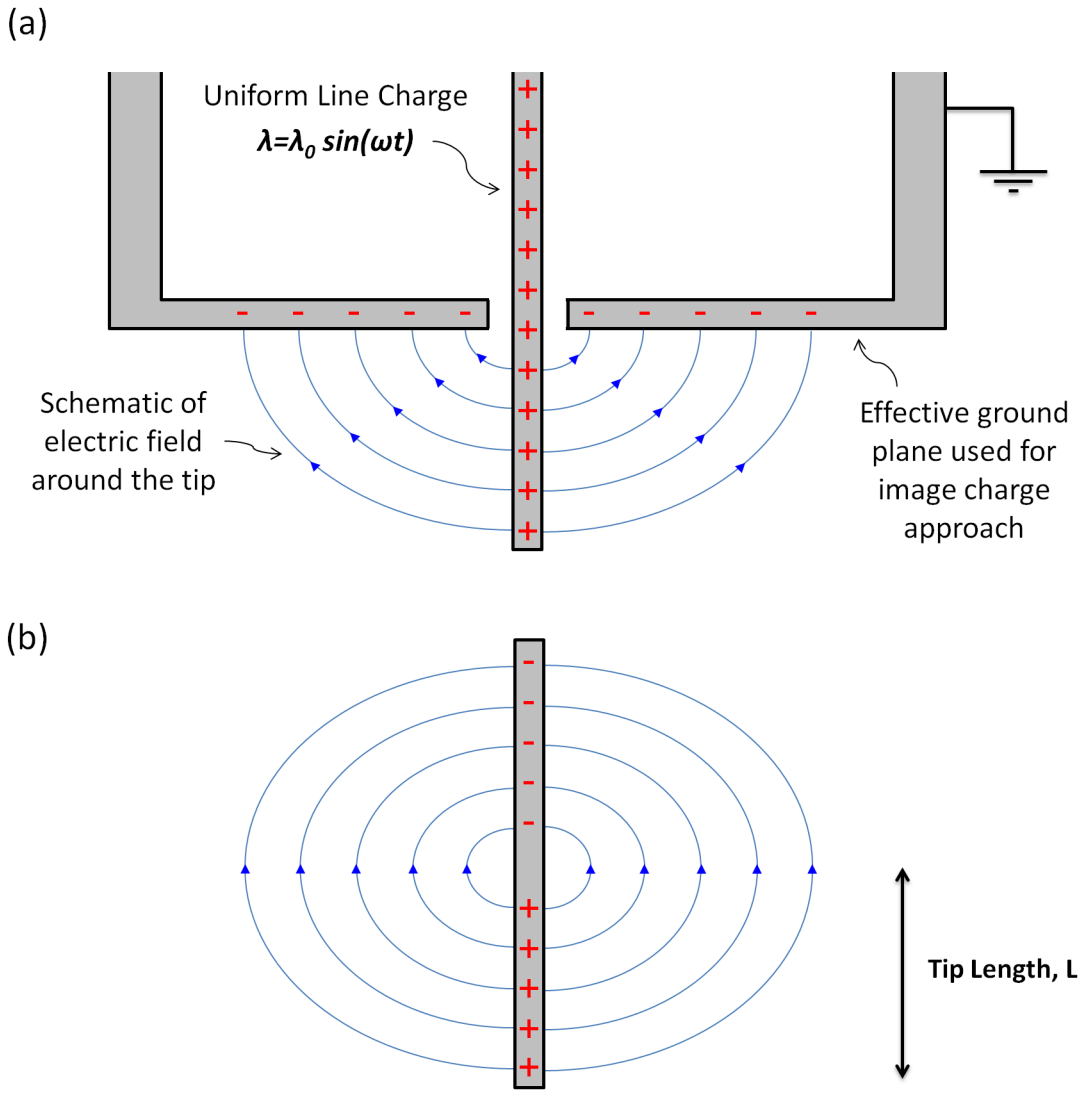

Figure 3.9: Part (a) shows a schematic of the end of the microwave resonator along with the charge distribution and associated electric field lines. The resonator body is treated as a grounded plane, allowing use of the image charge technique to simplify the charge distribution. Part (b) shows the simplified charge distribution created by treating the end of the resonator body as a ground plane and replacing it with an image charge of the probe tip.

oriented along the z axis and centered at the origin, the charge distribution can be written as:

$$\lambda(r,\theta,z,t) = \lambda_0 S(z)\delta(r)H(L-|z|)sin(\omega t) \tag{3.7}$$

Where λ_0 is the charge per unit length on the tip, $S(x) = \begin{cases} -1 & x \geq 0 \\ \\ +1 & x < 0 \end{cases}$, $\delta(x)$ is the Dirac delta function, $H(x) = \begin{cases} 1 & x \geq 0 \\ \\ 0 & x < 0 \end{cases}$, ω is the angular frequency, L is the length of the tip, and t is time. This charge distribution oscillates at the resonant frequency, inducing a current on the tip. The ends of the effective antenna are current nodes, and the current is a maximum in the middle of the effective antenna. Since the charge is assumed to be linearly distributed, the magnitude of the current linearly increases from the ends of the effective antenna, reaching a maximum in the middle.

$$I(r,\theta,z,t) = (L-|z|)\lambda_0\delta(r)H(L-|z|)\omega cos(\omega t) \tag{3.8}$$

This is precisely an electrically short (i.e. small compared to the wavelength) electric dipole antenna. Making the magnetostatic approximation, we calculate the magnetic field by using the Biot-Savart Law and integrating over the current.

$$\overrightarrow{B} = \frac{\mu_0\lambda_0\omega}{4\pi}\left(\sqrt{1+(\frac{L-z}{r})^2} + \sqrt{1+(\frac{L+z}{r})^2} - 2\sqrt{1+(\frac{z}{r})^2})\right)\hat{\theta} \tag{3.9}$$

In order to estimate the magnitude of the magnetic field, we now need the charge per unit length along the tip, λ_0. To find this value, we calculate the charge per unit length on a coaxial capacitor that contains the same amount of energy as the energy stored in the resonator. We begin with the equation for the charge stored in a capacitor.

$$q = \sqrt{2C_R E_{stored}} \tag{3.10}$$

Where q is the charge stored in the capacitor and C_R is the effective capacitance of the lumped element resonator in given in 2.2. The energy stored in the resonator is simply the quality factor times the energy dissipated per cycle.

$$E_{stored} = QE_{lost} \tag{3.11}$$

At equilibrium, the power input to the resonator is the same as the power leaving the resonator, so we can calculate the energy lost per cycle.

$$E_{lost} = P_{in}/f_r \tag{3.12}$$

Where f_r is the resonant frequency. The power input to the resonator can be calculated using the power of the microwave source and the transmission coefficient of one port of the resonator.

$$P_{in} = P_{source}T \tag{3.13}$$

Q (unitless)	f_r (GHz)	P_{source} (dBm)	T (unitless)	L (mm)	λ_0 (nC/m)	V_{tip} (mV)	B_{max} (mOe)
440	2.42	8.6	.1	2	∼1.6	∼70	∼15

Table 3.1: The charge density on the tip, λ_0, electrical potential, V_{tip}, and maximum magnetic field near the probe tip, B_{max}, are calculated using equations 3.15, 3.16, and 3.9 respectively. The parameters are the resonator quality factor, Q, the resonator resonant frequency, f_r, the power of the microwave source, P_{source}, the power transmission coefficient, T, and the tip length, L.

Where P_{source} is the microwave source power and T is a transmission coefficient, describing the fraction of power from the source that is not reflected back to the source (the resonator is only weakly coupled to the RF source). Putting all of this together, we have a more useful equation for the charge.

$$q = \sqrt{2C_R Q P_{source} T / f_r} \tag{3.14}$$

For a coaxial capacitor, the charge per unit length is simply the total charge divided by the length of the coaxial capacitor, or in this case, the length of the resonator, l.

$$\lambda_0 = \frac{1}{l}\sqrt{2C_R Q P_{source} T / f_r} \tag{3.15}$$

Having obtained the charge per unit length on the tip, we can also estimate the electrical potential of the tip relative the the outer body of the resonator using the value of our resonator capacitance.

$$V_{tip} = q / C_R \tag{3.16}$$

Figure 3.10 shows the calculated magnetic field just beneath the end of the tip for

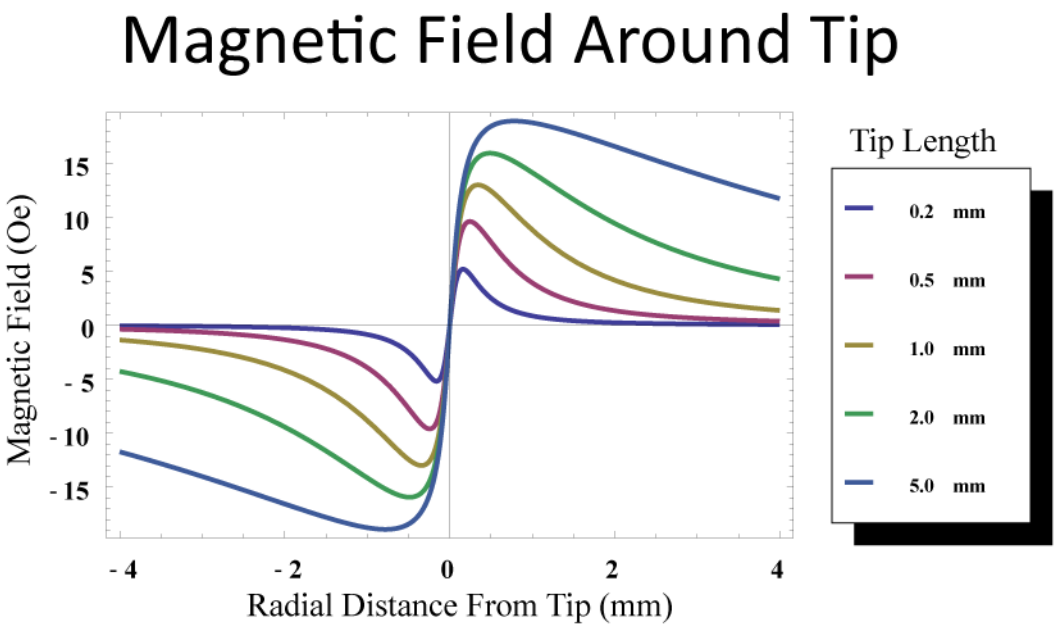

Figure 3.10: The RF magnetic field just under the tip calculated for several different tip lengths using Equation 3.9. The field has a component only in the azimuthal direction. The actual tip length for this experiment is 2 mm, plotted in green. The magnetic field confinement would be better for shorter tips, but at the cost of decreased field intensity.

several different tip lengths.

Figure 3.11 shows the RF magnetic field around the probe tip for a 2 mm long tip, as used to obtain FMR spectra in this experiment.

3.6.2 Magnetostatic Spin Wave Modes

The calculated magnetostatic spin wave modes, calculated microwave absorption as a function of tip position, and experimentally observed microwave absorption for the two strongest RF energy absorption lines are presented in Figures 3.12 and 3.13.

In Figure 3.12 (a), we see the uniform precession spin wave mode. The amplitude of precession of the spins inside the disk is indicated by the size of the small circles within the disk, while the relative phase between spins is indicated by the direction

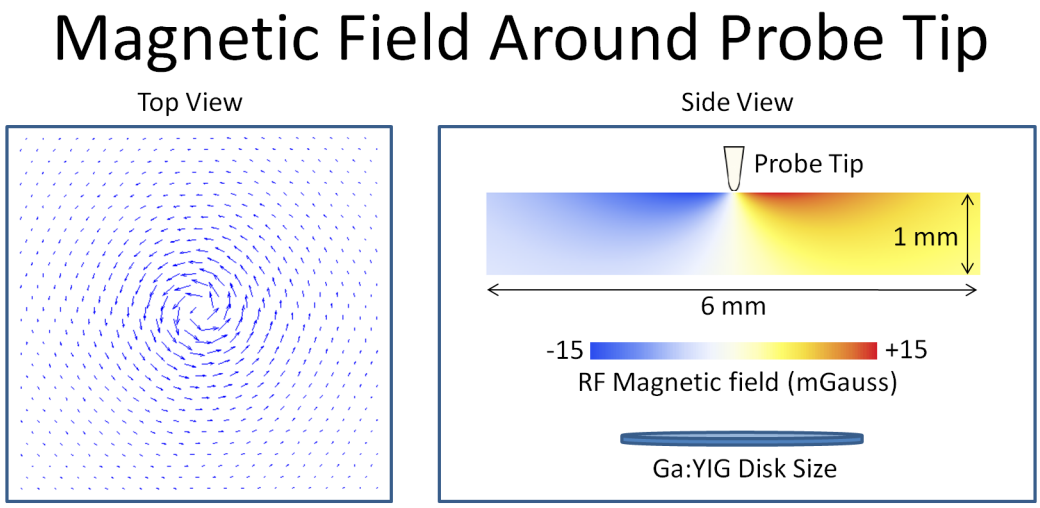

Figure 3.11: The magnetic field under the probe tip calculated using Equation 3.9. The magnetic field is zero directly under the tip, increases radially to a maximum value approximately 0.5 mm from the tip, then decays.

of the line inside each small circle. In this case all of the spins precess in phase, and we call this the uniform precession mode. The amplitude of spin precession is a maximum at the center of the disk and zero at the edges. We find that when the tip is positioned over the center of the disk, there is only minimal absorption of microwave energy. This is because when the tip is positioned in the middle of the sample, the microwave magnetic field reverses direction as one moves across the diameter of the disk, while the phase of the spin precession for this mode does not. The result is that there is no net excitation of the spins in the sample. In contrast, when the tip is near the edge of the disk, the direction of the RF magnetic field is fairly uniform across the region of the sample where the spin precession amplitude is largest. In this configuration, the spins in the sample are excited by the RF magnetic field and there is a corresponding increase in the absorption of microwave energy.

The observed RF absorption in Figure 3.12 (d) does not quite match the absorp-

tion profile calculated using RKMAG (displayed in part (c) of the same figure). One likely explanation for this is that the presence of the tuning fork glued to the probe tip distorts the RF magnetic field such that it does not quite match the field produced by the model presented in section 3.6.1. This would break the symmetry of the RF field around the probe tip, which we would expect to also break the symmetry of the absorbed microwave energy profile.

In Figure 3.13 (a) we see the spin wave mode profile for the absorption line labeled peak 2 in Figure 3.8. This mode has a node in the amplitude of spin precession at the center of the disk as well as at the edge of the disk. The phase of the spin precession winds through one complete cycle as one moves around the disk in the azimuthal direction. In this case, we find that the maximum absorption of microwave energy occurs when the tip is positioned in the center of the disk and decreases monotonically as one moves away from the center of the disk. In Figure 3.13 (b) we see the configuration of the RF magnetic field when the tip is positioned at the center of the disk overlaid on top of the spin wave mode profile. When the tip is positioned at the center of the disk, the direction of the microwave magnetic field matches the phase of the spin wave throughout the disk. This configuration leads to optimal excitation of this spin wave mode, and thereby maximal absorption of microwave energy.

Figure 3.14 shows a comparison of the simulated FMR absorption spectra and the measured absorption spectra. The absorption of microwave energy as the tip is scanned across the sample displays good qualitative agreement, verifying that the observed peaks in the FMR spectra correspond to magnetostatic spin wave modes. The

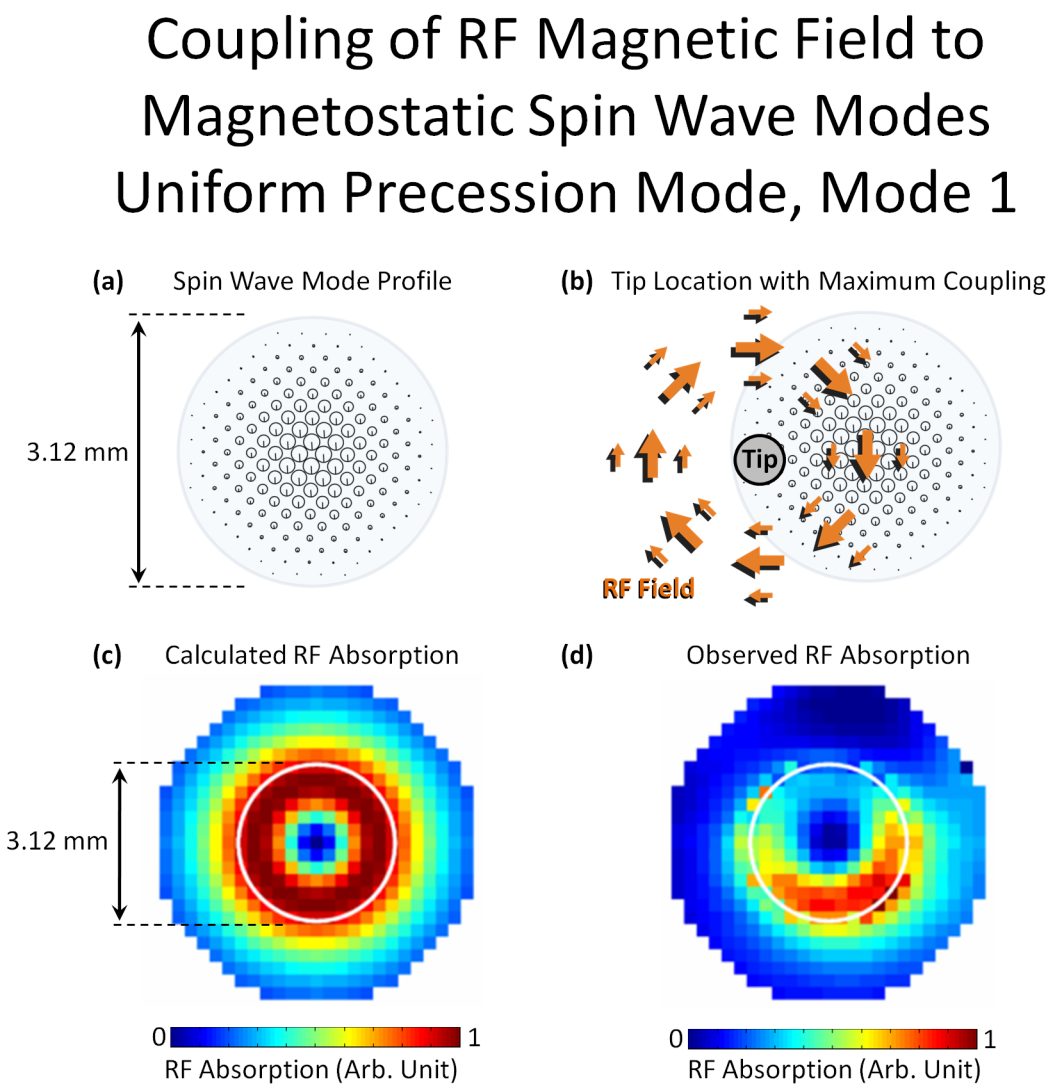

Figure 3.12: Part (a) shows the excitation of spins for the lowest energy spin wave mode in the Ga:YIG disk. The amplitude of precession of the spins inside the disk is indicated by the size of the small circles within the disk, while the relative phase between spins is indicated by the direction of the line inside each small circle. In this case all of the spins precess in phase, and we call this the uniform precession mode. Part (b) shows a schematic of the RF magnetic field near the tip, with the tip positioned near the edge of the sample. Part (c) shows the calculated absorption of microwave energy as a function of tip position when the resonance condition for this mode is met. Part (d) shows the experimentally observed absorption of microwave energy for this mode. The white circle in parts (c) and (d) indicates the perimeter of the Ga:YIG disk.

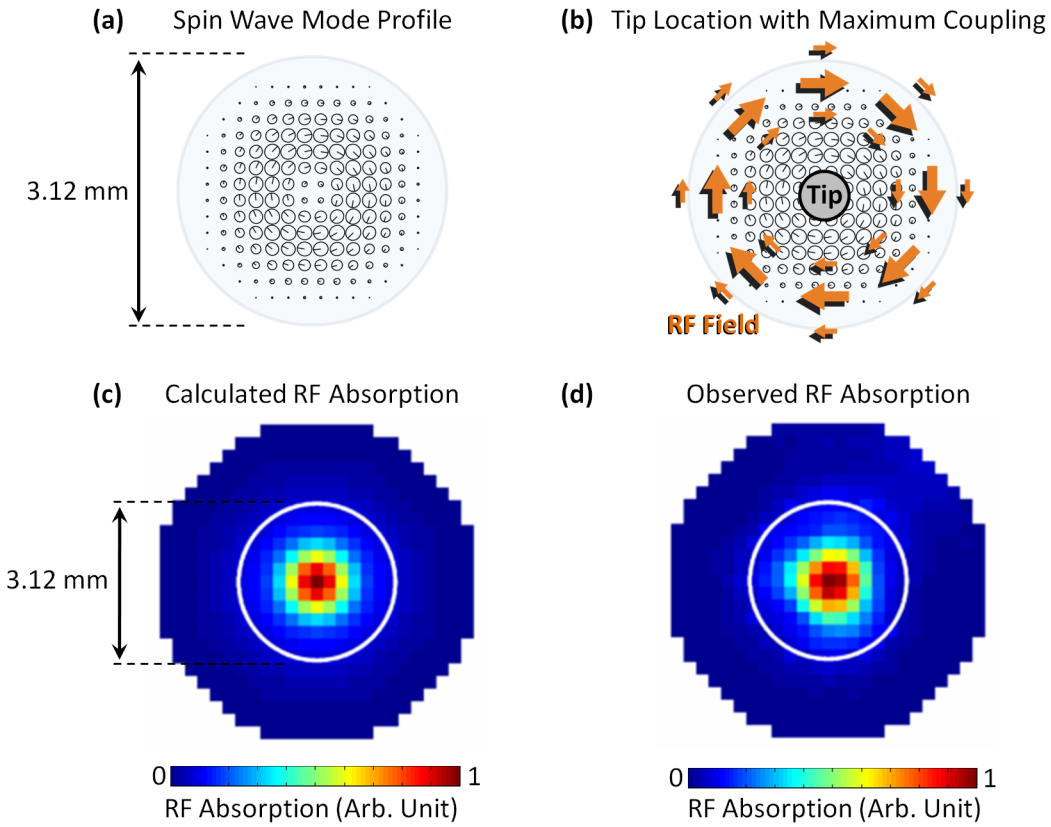

Figure 3.13: Part (a) shows the excitation of spins for the second lowest energy spin wave mode in the Ga:YIG disk. The amplitude of precession of the spins inside the disk is indicated by the size of the small circles within the disk, while the relative phase between spins is indicated by the direction of the line inside each small circle. Part (b) shows a schematic of the RF magnetic field near the tip with the tip positioned in the center of the sample. Part (c) shows the calculated absorption of microwave energy as a function of tip position when the resonance condition for this mode is met. Part (d) shows the experimentally observed absorption of microwave energy for this mode. The white circle in parts (c) and (d) indicates the perimeter of the Ga:YIG disk.

main discrepancies between the simulated and experimental data are that simulated data does not show any shift in the resonance field as the tip is scanned across the sample, and that the field at which resonance occurs are not the same. We attribute this shift in the resonance field in the experimental data to a gradient in the magnetization of the measured sample. The difference in the resonance field we attribute to a mismatch between the average magnetization of the sample and the magnetization that is used in the simulation.

3.7 Conclusion

The nominal spatial resolution for performing FMR spectroscopy using the coaxial resonator NFMM geometry is on the order of the length of the tip ($\sim$2 mm in this case), which sets the length scale for the spatial confinement of the RF magnetic field. This spatial resolution is much lower than the spatial resolution for dielectric imaging for the same tip geometry (which is on the order of the radius of curvature of the tip end, typically $\sim$1 μm), however it is sufficient for screening wafer scale combinatorial libraries, where the sample size is typically a few mm.

The amount of microwave energy absorbed by the sample for a particular FMR resonance line depends on the tip position over the sample; however it does not correspond to the excitation of spins directly beneath the tip. Indeed, the maximum absorption of microwave energy occurs when the tip is positioned above a spin wave node, in which case the spins directly below the tip are at rest. This behavior arises from the highly non-uniform RF magnetic field produced by the tip, which consists

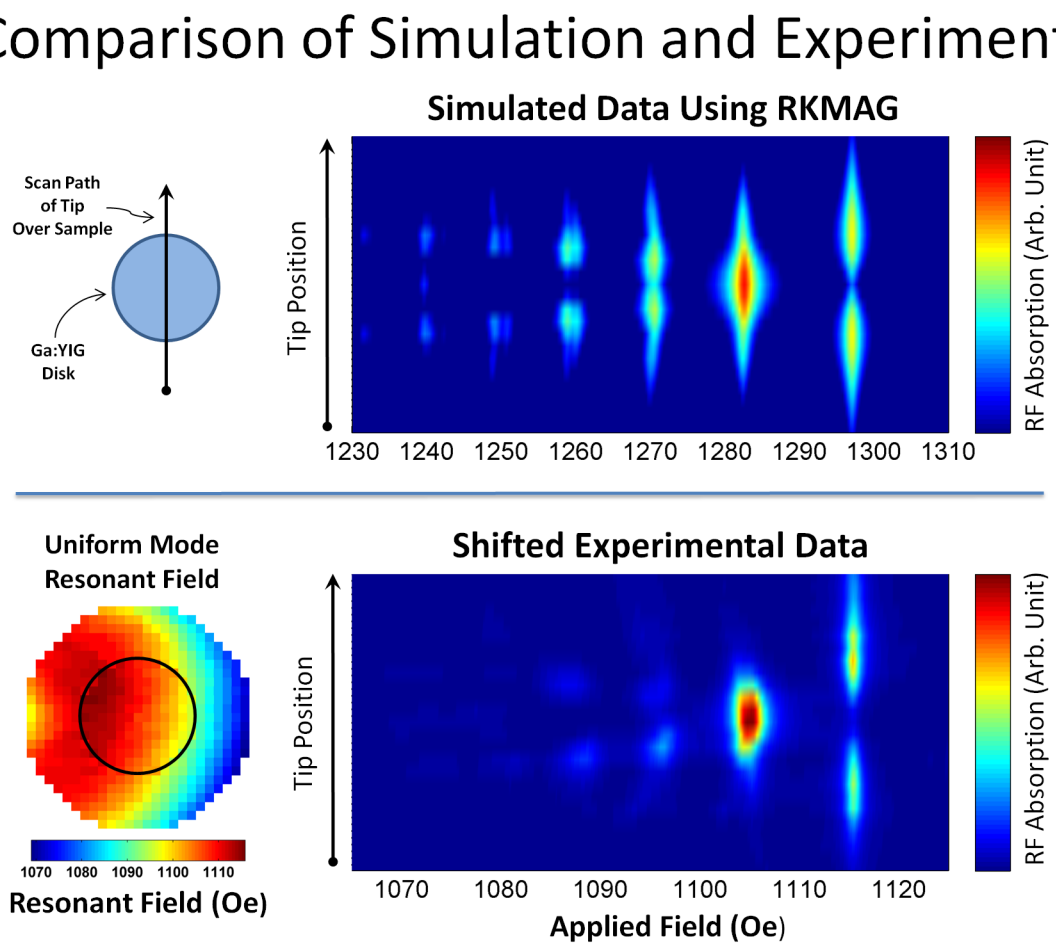

Figure 3.14: A comparison between the energy absorption spectra calculated using RKMAG and the experimentally observed absorption spectra. To make the spatial dependence of the absorption intensity more visible, the experimentally observed spectra have been shifted in order to align the field at which the uniform mode peak occurs. In the un-shifted data, the uniform mode peak occurs at the fields displayed at the bottom left. The black circle indicates the location of the Ga:YIG disk.

of field lines that circle the tip and are oriented in the plane of the sample.

One of the interesting features of the scanning FMR spectroscopy data obtained in this experiment is that the resonance field shifts as the tip is scanned over the sample. We attribute this shift to a gradient in the sample magnetization. This gradient changes the effective magnetic field within the sample, resulting in a shift in the resonant field. This leaves open the possibility of backing out the magnetization gradient within the sample. The investigation of this possibility is left to future work.

Chapter 4

Hybrid NFMM-STM

4.1 Abstract

In this chapter, we show that the spatial resolution of NFMM can reach atomic resolution when the tip-sample distance is small enough to allow tunneling between the tip and the sample. Atomic resolution imaging is demonstrated using a hybrid instrument that is capable of performing as both a scanning tunneling microscope (STM) and near-field microwave microscope (NFMM) simultaneously. The microwave channels of the microscope correspond to the resonant frequency and quality factor of a coaxial microwave resonator that is built in to the scan head. The microscope is capable of simultaneously recording the low frequency tunnel current 0–10 kHz and the information from the microwave channels. When the tip-sample distance is within the tunneling regime, we obtain atomic resolution images using the microwave channels. We attribute this atomic contrast to GHz frequency current through the tunnel junction. Images of highly oriented pyrolytic graphite (HOPG) and Au(111) are presented.

4.2 The NFMM-STM System

Combining NFMM with STM provides two advantages. First, the combination of NFMM and STM can potentially enhance the spatial resolution of NFMM. NFMM

achieves subwavelength spatial resolution by bringing the microwave field source to a distance that is much less than the wavelength from the sample under study, overcoming the diffraction-limited spatial resolution barrier.[26] STM can be used to controllably bring the probe tip to within a nanometer of a conducting surface, maximizing the spatial resolution of NFMM. Second, STM can be used to measure electrical properties at subangstrom length scales.[27] This enables simultaneous measurement of the microwave near-field interactions and the low frequency electrical properties of the sample.

Figure 4.1 shows a schematic of the main components in our NFMM-STM system. The microwave driving frequency is maintained at the resonant frequency of the microwave cavity using phase sensitive detection, as discussed in Section 2.3. Fine approach of the tip to the sample, XY scanning, and closed loop topography feedback are accomplished by means of a piezoelectric tube. The piezo tube provides $\sim$1x1 μm^2 scanning range in the XY plane and a 0.8 μm travel range in the Z direction. Typically, the driving voltage for the scanner is in the range of $\pm$150 Volts. The electrodes on the piezo tube are patterned into four quadrants around the outer circumference and one single electrode on the inner surface. The Z position of the tip is controlled by the voltage applied to the center electrode, and the XY scanning is controlled by applying voltages to the outer electrodes. For STM operation, the sample is biased and the tunnel current is measured using a lead directly connected to the microwave resonator. The tunnel current is measured using a model 1211 current preamplifier by DL instruments.

Figure 4.2 shows a schematic of the resonator inside of the NFMM-STM system.

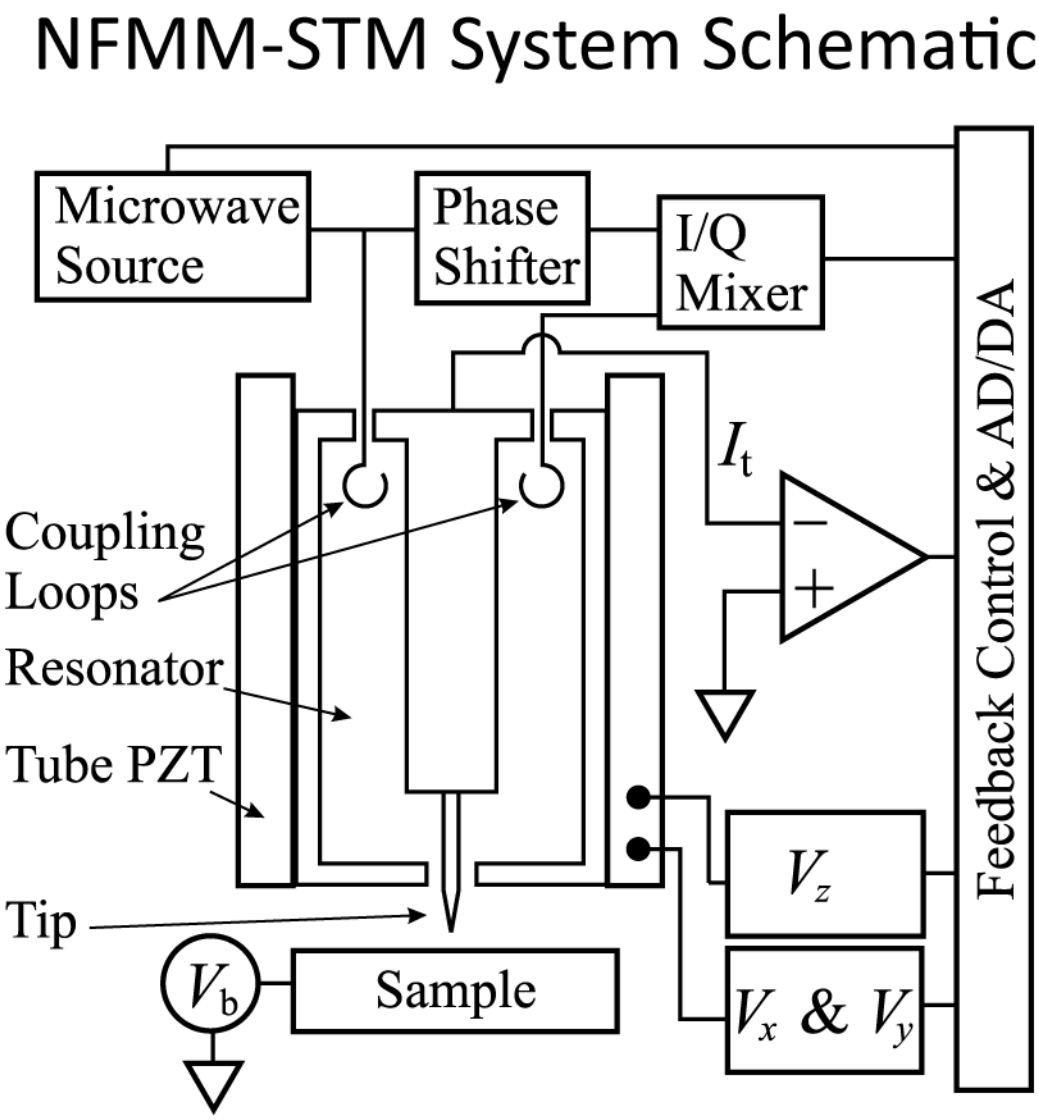

Figure 4.1: Schematic of hybrid NFMM-STM

The center conductor of the resonator has a well full of indium solder, into which a copper tube has been placed. The inner diameter of the copper tube nearly matches the diameter of the STM tip that is mounted inside of it. The STM tip[31] is held in place by a making a slight bend in the tip wire before it is placed into the copper tube. On the closed end of the resonator, there is a directly connected lead for measuring tunnel current as well as input/output ports for microwave signals. Each microwave port consists of a coaxial cable that is inductively coupled to the resonator. The inductive coupling is achieved by forming a single turn loop from the center conductor to the outer conductor of the coaxial lead and placing the loop into the resonator. During a scan, a DC bias voltage is applied to the sample. This experimental set-up allows us to measure the low frequency tunnel current between the tip and sample while simultaneously monitoring the f_{r} and Q of the resonator. The resonator is filled with a sapphire crystal[1] in order to reduce the resonant frequency from $\sim$9 GHz down to $\sim$2.5 GHz, matching the capabilities of our microwave source.

Figure 4.3 shows a schematic of the scan head for the hybrid NFMM-STM system. Coarse approach is accomplished by means of a slip-stick inertial stepper motor (Attocube Model ANPz100/LT/HV), which provides 6 mm of travel in the Z direction. This motor has a stage (where the resonator is mounted) that is held into a base using straight shaft gripped by static friction. In order to step the stage towards the sample, a piezoelectric element slowly extends the stage towards the sample, and then rapidly contracts. Since the mass of the stage is much larger than the mass of the mounting shaft, the result of the rapid piezo contraction is that the position of the

[1]The permittivity of sapphire is 9.4.

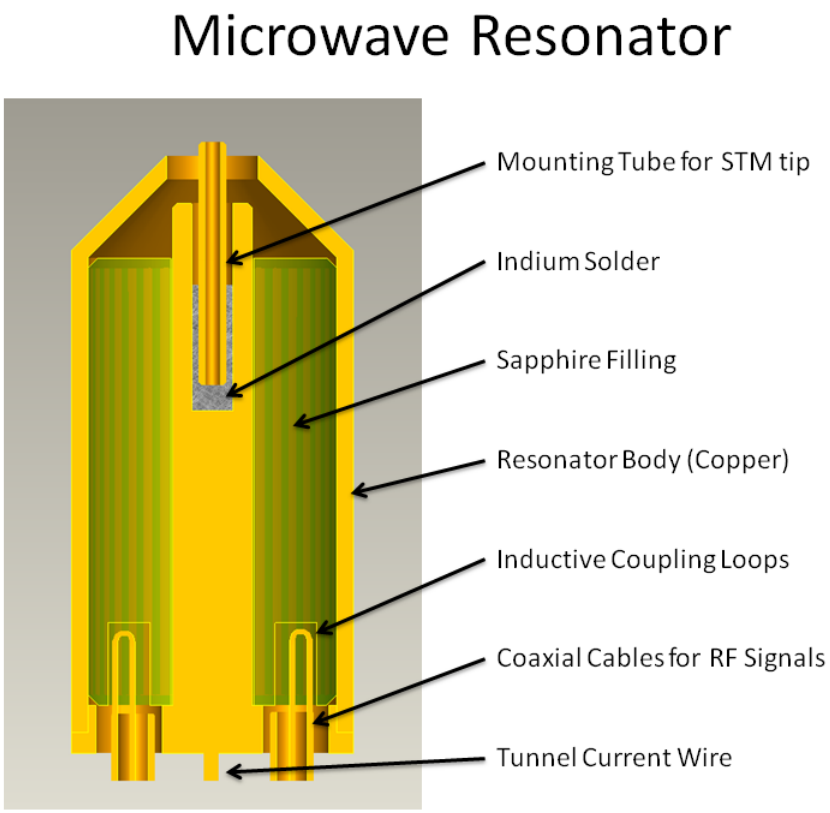

Figure 4.2: A cross section schematic of the microwave resonator in the NFMM-STM system. The measured resonant frequency is ∼2.5 GHz. The unloaded (i.e. without tip sample interaction) quality factor is ∼600. There is a small variation in these parameters depending on the tip that is used.

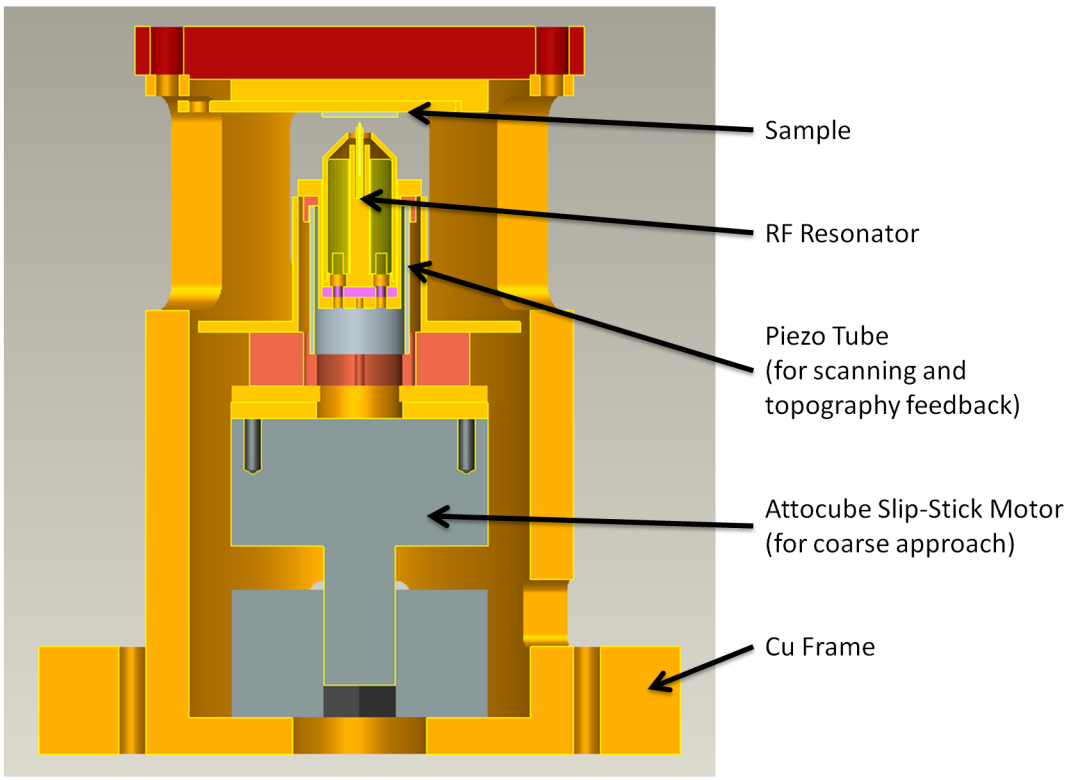

Figure 4.3: A cross section schematic of the scan head for the NFMM-STM system.

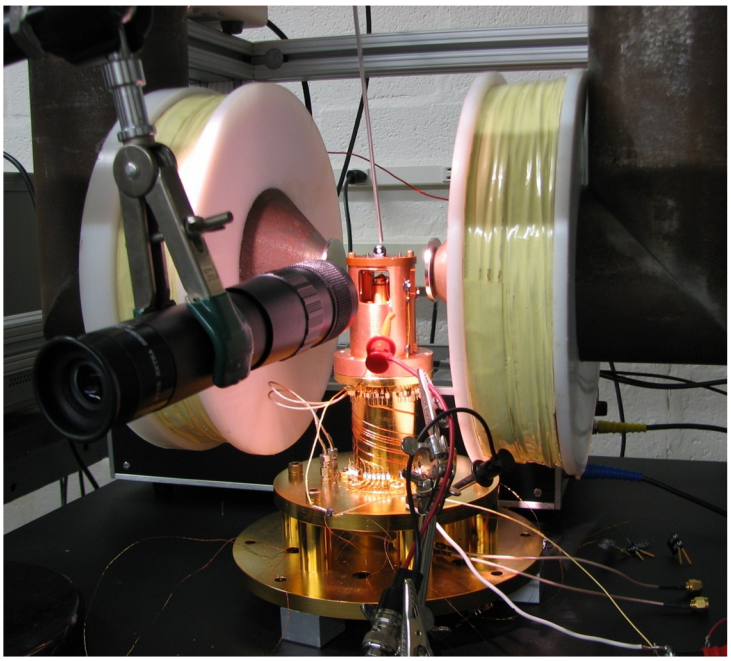

Figure 4.4: A photograph of the scan head of the NFMM-STM mounted inside an electromagnet.

stage remains roughly constant while the shaft breaks the hold of static friction and slips up towards the sample stage. In order to step the motor away from the sample, the piezo is driven to expand very rapidly, and then contract slowly.

The scan head is mounted onto a gold plated copper frame that is designed to be mounted into a cryostat. Outside of the cryostat, the scan head is mounted inside of an electromagnet, which can be used to apply magnetic fields in the range of ± 1200 Gauss. This configuration was originally intended to be used to detect spin resonance in single molecules deposited onto a conducting sample surface. However we found that there are several magnetic components inside the scan head (which was

manufactured originally by Intematix Corporation). The presence of these magnetic components causes the tip to move relative to the sample when a magnetic field is applied, making it very difficult to observe the behavior of an adsorbed molecule as a function of applied magnetic field. Particularly troublesome is the steel center conductor of the microwave cables, which are nearly impossible to replace due to the extensive use of epoxy in the construction of the scanner. A completely new scan head that contains no magnetic components is currently being fabricated. This new scanner should be suitable for magnetic field sweeps in the near future.

In the tunneling regime, the separation between the tip and the sample is on the order of one nanometer and the tunnel current changes dramatically if the tip-sample distance is changed even by the diameter of a single atom. If ones goal is atomically resolved images, then lateral vibrations of the tip in the in-plane direction of the sample must be reduced to below the diameter of an atom. The elimination of mechanical and electromagnetic noise is therefore critical to obtaining high-resolution images.

Three big noise sources in the NFMM-STM system are the mechanical vibration of the floor, acoustic noise in the air, and pickup of electromagnetic noise. High frequency electromagnetic shielding is particularly important because the microwave resonator operates in the unregulated industrial, scientific, and medical radio band (2.4-2.5 GHz), which among other things is used for Wi-Fi networks and microwave ovens.

In order to minimize the effects of the floor vibration, the scan head and the electromagnet are mounted in an air table. Each leg of the air table is resting on an

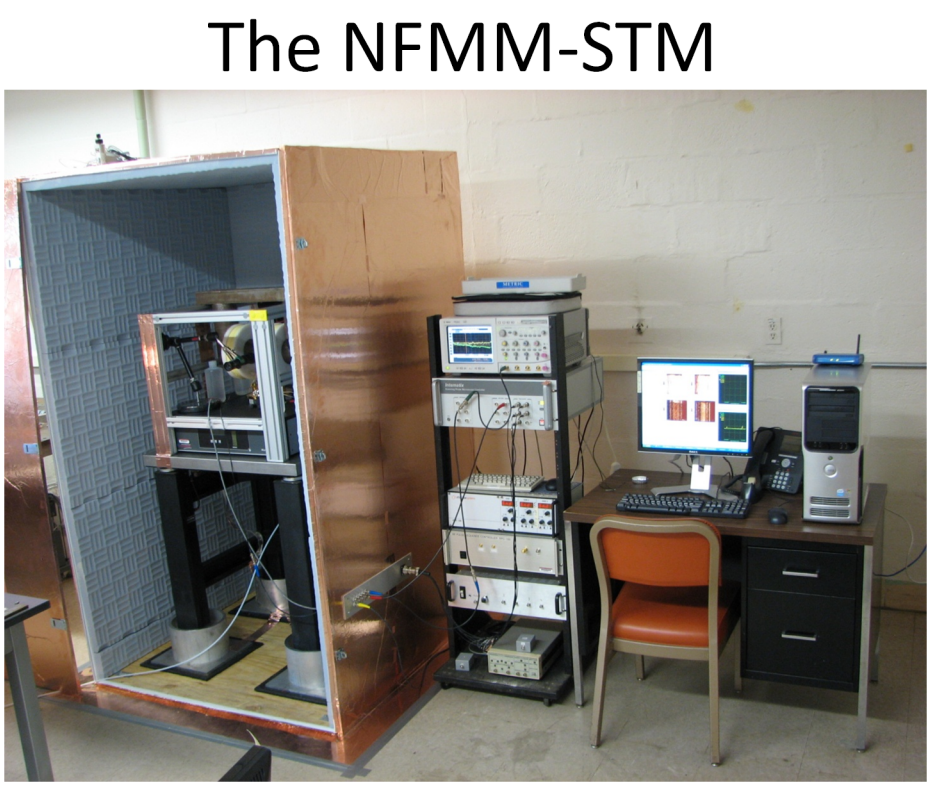

Figure 4.5: The experimental setup for the NFMM-STM system. The scan head is mounted on top of an air table, which is in turn mounted on top of sand boxes. Electromagnetic and acoustic isolation are achieved by a shield room that is closed during normal operation. The shield room consists of plywood coated with copper foil (.0014 inch thick) on the outside and sound absorbing foam panels on the inside.

aluminum cylinder filled with sand, and these aluminum cylinders are in turn resting on half inch thick rubber tiles. An active vibration isolation platform (Halcyonics Micro 60) is also present; however, we generally leave it turned off because it generates electromagnetic interference.

Acoustic and high frequency electromagnetic noise are shielded out using an isolation booth built around the air table. The booth is constructed primarily out of plywood. The interior surface is lined with sound insulating foam panels, while the exterior of the booth is covered in copper foil that is .0014 inch thick. Any gaps in the copper foil are filled using conducting copper tape. This isolation booth was a key factor in pushing the noise floor low enough to be able to resolve single atoms using the NFMM-STM.

4.3 NFMM-STM Experiment

The unloaded resonator has a nominal f_r of 2.5 GHz and a nominal Q of 600, with some small variation depending on the STM tip that used. As the tip is approached to the sample surface, the microwave near-field interaction between the tip and the sample results in changes in f_r and Q. Figure 4.6 shows the behavior of f_r, Q, and the tunnel current, I_t, as the tip is approached to the sample surface. There are two distinct regimes, one corresponding to the nontunneling regime (black) and one corresponding to the tunneling regime (red). In the nontunneling regime, Q is almost unaffected by the tip-sample distance; in the tunneling regime, Q drops suddenly as I_t increases. The decrease in Q is attributed to dissipation of microwave energy through

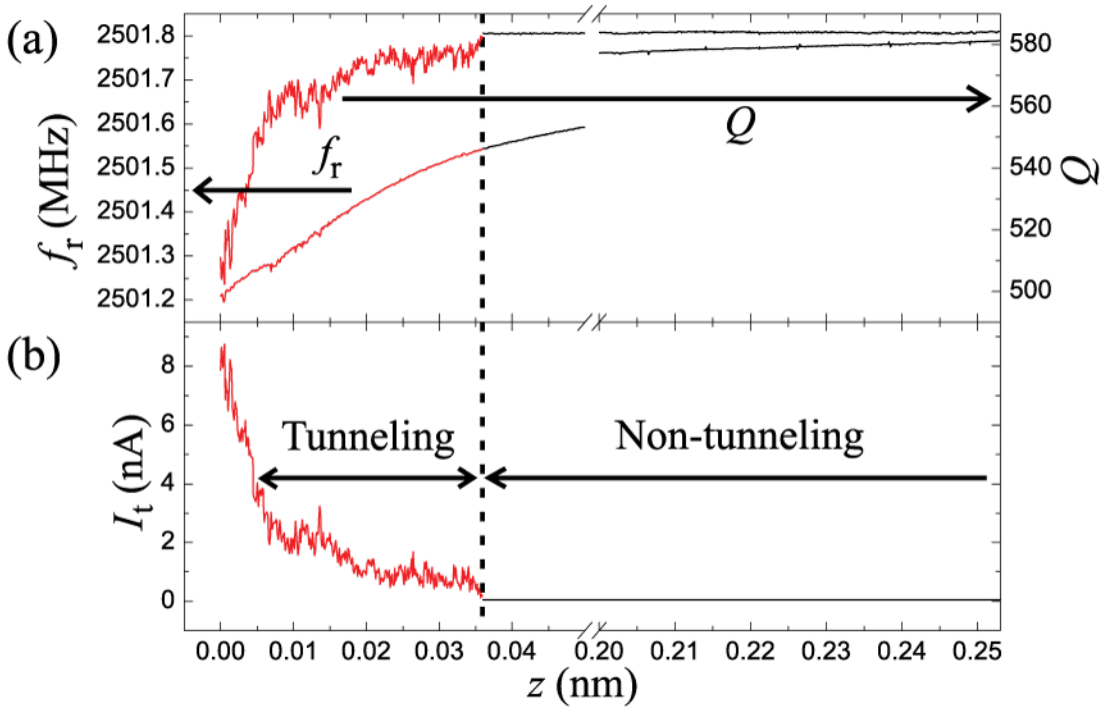

Figure 4.6: Approach curves of (a) the microwave channels, f_r and Q and (b) STM channel, I_t as a function of tip height, Z. Plots are in red when tunneling occurs. All plots are simultaneously acquired on a single tip-sample approach.

the tunnel junction. On the other hand, we do not see a slope discontinuity for f_r at the onset of tunneling. This is because f_r depends mostly on the reactive component of the tip-sample junction, which is not affected by the onset of tunneling.

In order to track the f_r and Q of the resonator during a scan, we employ quadrature homodyne detection.[32] Using this detection scheme allows us to rapidly compute the f_r and Q during a scan without sweeping the microwave driving frequency at each image pixel. The resonator responds to changes in the tip-sample impedance on a time scale given by the decay time of transients in the resonator, $\tau_\mathrm{decay} = Q/f_\mathrm{r}$. For our system, the upper limit on the bandwidth of the microwave channels is $1/\tau_\mathrm{decay} \approx 4$ MHz, which is far above the bandwidth of our STM (0-10 kHz). Thus, the limiting

factor in the scan speed is the bandwidth of the STM current amplifier.

In Figure 4.7, we simultaneously collect STM topography and microwave signals while scanning a 300 x 300 nm^2 area of Au(111). Figures 4.7(a) and 4.7(b) show STM images of tip height, Z and I_t. Figures 4.7(c) and 4.7(d) show the microwave signal images of f_r and Q, respectively. These images were obtained in the STM constant current mode, which regulates the tip-sample distance such that a set point of 1 nA (with V_{bias} = 100 mV) is maintained. Since the tunnel junction resistance is constant in constant current mode, we observe negligible contrast in the Q channel. On the other hand, the f_r image clearly shows the same surface steps as the STM tip height image. The f_r of the cavity is proportional to $1/L_{eff}C_{eff}$, where L_{eff} and C_{eff} are the effective inductance and capacitance of the resonator. Qualitatively, as the tip moves away from the sample, the effective tip-sample capacitance decreases, increasing the f_r of the cavity. Thus, under constant current STM operation, the f_r channel is a convolution of the topography information obtained by STM and the microwave interactions with the sample.[33] For highly conducting samples, it is possible to take advantage of this fact to perform tip-sample distance feedback using the f_r of a NFMM.[34] However, if one wishes to see variations in materials properties without convolving the sample topography, then it is necessary to scan an atomically flat sample without changing the tip-sample distance.

In order to avoid convolution of the NFMM channels with topographic features, we next focused on an atomic scale area ($\sim$1 x 1 nm^2) of HOPG. Scanning a small area allows us to utilize constant height (open loop) mode without damaging the probe tip, while the atomically flat surface of HOPG provides a topography free surface. In order

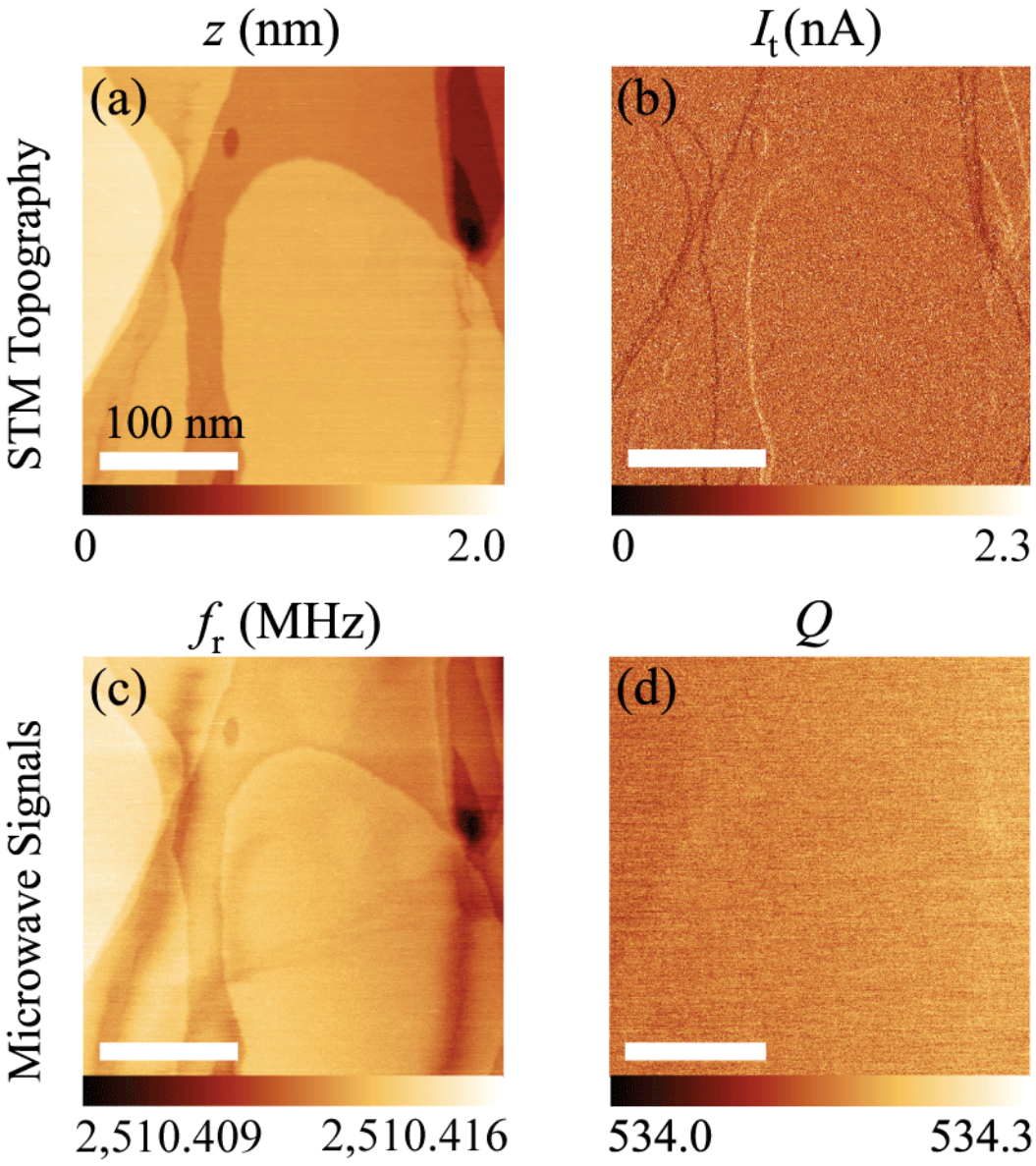

Figure 4.7: Large-scale images of Au(111) taken in STM constant current operation. (a) Tip height, Z, (b) tunnel current, I_t, (c) resonance frequency, f_r, and (d) quality factor, Q images. All images are acquired simultaneously. The images have been pre-processed by matching the median height between scan lines.

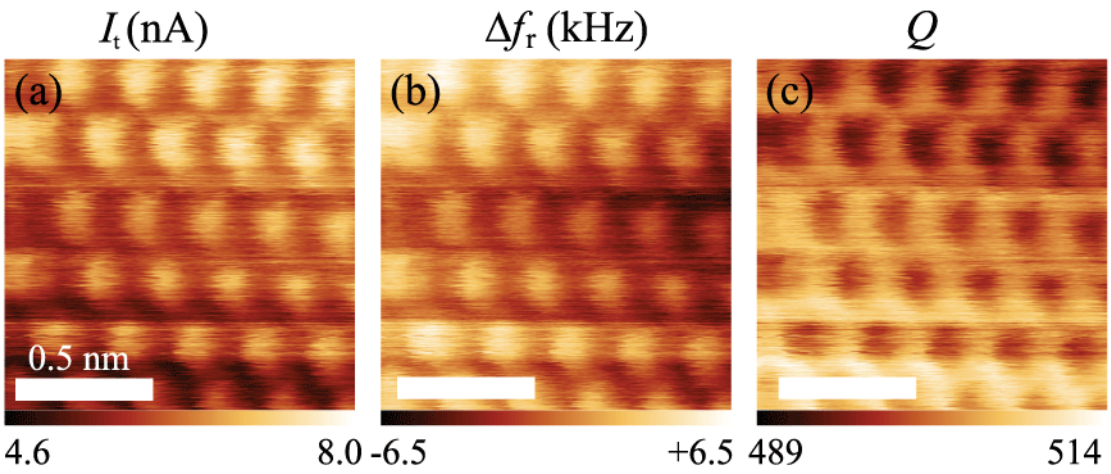

Figure 4.8: Atomic resolution images of HOPG taken in STM constant height operation. (a) Tunnel current, I_t, (b) resonance frequency shift, f_r, and (c) quality factor, Q images. All images were acquired simultaneously at a scan speed of 20 line/s with a bias voltage of 100 mV. The mean resonance frequency is f_r =2.501486 GHz.

to image HOPG, we first used constant current (closed loop) operation to optimize the bias voltage, tunnel current, and scan speed such that good signal-to-noise was achieved in the STM topography, f_r, and Q channels. Once the scan parameters were optimized, we opened the tip-height feedback loop and recorded scan images in constant height mode.

In Figure 4.8, one can see individual graphite atoms in I_t, f_r, and Q, respectively. The average tunnel current is 6.2 nA with a mean atomic corrugation (peak to trough) of 1.1 nA. The average f_r is 2.501486 GHz with a mean atomic corrugation of 4 kHz. The average Q is 502 with a mean atomic corrugation of 5.5. Using the atomic corrugation of f_r, we find the corresponding effective capacitance change in the resonator, $\delta C_{eff} = 2C_{eff} \times \delta f_r/f_r = 9 \times 10^{-18}$ F, where $\delta f_r/f_r = 1.6 \times 10^{-6}$ and $C_{eff} = 2.8 \times 10^{-12}$ F. Slight lattice distortion is due to relaxation of the piezo tube scanner during scanning.

In order to verify that we are truly imaging the surface of the HOPG using the microwave impedance between the tip and sample, it is very important to rule out any kind of cross-talk between the STM and microwave channels. In general, there are two possible ways that "artificial" atomic contrast could occur in the microwave channels. The first possible source of cross-talk is through the topography feedback loop, as discussed in regard to Figure 4.7. If the tip-sample distance is controlled by the STM tunnel current, and the tunnel current changes as the tip is scanned over some atomic corrugation, then the height of the tip above the sample will also change. As this tip-sample distance varies, the microwave near-field interaction between the tip and sample will also change, resulting in atomic contrast in the microwave channels. This cross-talk mechanism is a particular problem for microwave microscopy because the microwave channels are very sensitive to the tip-sample distance. In order to avoid this scenario, we operated the STM in open-loop mode so that the height of the tip does not depend on the tunnel current.

The second possible source of cross-talk would be some kind of direct coupling between the tunnel current signal and the microwave channels (e.g., capacitive coupling between signal lines). In order to rule out this possibility, we disconnected the DC bias voltage from the sample and disconnected the STM tunnel-current amplifier from the resonator. In this configuration, we approach the tip to the sample using the resonator Q as a feedback signal, stopping the tip-sample approach when the Q is decreased by about 10%. Figure 4.9 shows atomic resolution images obtained on Au(111) using this method. We found that we were able to obtain atomic resolution images in the microwave channels even without the STM circuitry connected to the

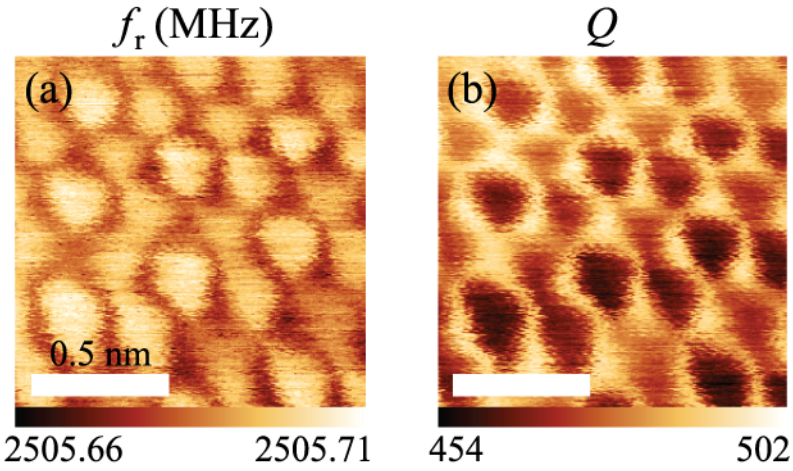

Figure 4.9: Atomic resolution images of Au(111) taken in only microwave microscopy mode. The STM bias voltage line and the current preamplifier are completely disconnected from the scan head, eliminating the possibility of crosstalk between these imaging modes.

system. As a result, the atomic resolution signal observed in the microwave channels can not be caused by cross-talk between the low frequency STM tunnel current and the microwave channels.

By ruling out artifacts caused by STM feedback or signal cross-talk, we conclude that the images of f_r and Q carry information about the impedance of the tunnel junction at 2.5 GHz. Furthermore, since the atomic contrast occurs only when the tip is within tunneling distance of the sample, we conclude that the atomic contrast in the microwave channels is due to gigahertz frequency current through the tunnel junction.

4.4 Conclusion & Future Work

STM is a fundamental tool for the investigation of conducting surfaces at sub-nanometer length scales. Unfortunately, the tunnel current sampling bandwidth of

traditional STM is limited to 10 kHz, due to the bandwidth of the tunnel current amplifier. Our NFMM has a theoretical bandwidth limit of 4 MHz and operates at 2.5 GHz. These two properties allow for collection of more information than traditional STM alone. For example, the large bandwidth of the NFMM allows it to sample the tunnel junction impedance much more quickly than traditional STM. This increased bandwidth can be used to perform rapid imaging, displacement detection up to megahertz frequencies, and shot noise thermometry.[23] Furthermore, phenomena that induce modulations in the tunnel current near the operational frequency of 2.5 GHz may be detected through resonant amplification in the microwave cavity. Such phenomena include single electron spin resonance[24, 25] and spin-transfer torque oscillations[35]. The work presented here represents a step toward bringing the spatial resolution of these microwave measurements to the atomic scale.

Part II

Multivariate Analysis of Combinatorial XRD Data

Chapter 5

Introduction to Multivariate Analysis of XRD Data

5.1 Motivation

In the mapping of composition-structure-property relationships, one piece of information of paramount importance is the phase and crystal structure distribution. There are scanning XRD techniques that can be employed to obtain a large number of diffractograms from combinatorial samples [53, 62, 63, 64, 65, 66]. Synchrotron XRD is a natural technique for this task because the high intensity X-ray beam available can be used to quickly step through a large number of positions on a combinatorial library with minimal time to obtain a diffraction spectrum at each point [62, 63, 64, 65]. In-house XRD units require a much longer time to take data per point, but their advantage is that one can perform the experiments locally [53, 55, 66].

Obtaining and analyzing XRD spectra for phase and structure determination is a central part of any materials research exercise, and it should play a significant role in combinatorial materials research as well. Ideally, one would measure and study X-ray spectra of all the materials in a given experiment in order to obtain complete mapping of phase and structural information across the sampled composition space. The traditional approach to analyzing a diffraction spectrum is to perform a Rietveld refinement in order to identify the crystal structure of a sample. The Rietveld refinement process consists of fitting the peaks of an experimental diffraction spectrum with

a theoretical diffraction pattern from a candidate crystal structure. The parameters of the candidate crystal structure are then varied in order to optimize the fit. With suitable experimental data, this process can be used to determine the crystal structure and lattice parameters of a material. A second approach is to fit the peaks of an experimental diffraction pattern with reflections of known compounds measured on the same diffractometer. This is typically done using software such as Jade by Materials Data, Inc. or Topaz by Bruker. Although some software can be automated to fit a large number of X-ray spectra serially, it is a cumbersome process and fitting does not necessarily produce the "correct answers". The very premise of the combinatorial experimentation is that there are potentially new phases with previously unknown crystal structures in the library, therefore any simple fitting procedure using reflections from known phases is not sufficient. The situation is further complicated by the fact that in any compositional phase diagram, there can be multi-phase regions.

Despite such difficulties, XRD analysis remains a most fundamental method in materials science, and one must find a way to effectively incorporate it into the overall combinatorial strategy. To this end, we discuss our methodology and procedures for multivariate analysis of XRD spectra from combinatorial libraries. The ultimate goal of this exercise is to obtain a comprehensive and accurate mapping of phase and structure distribution across composition spreads of rich and complex materials systems containing previously unknown materials phases. In particular, we will discuss two techniques: agglomerative hierarchical clustering analysis and non-negative matrix factorization.

The motivation for using agglomerative hierarchical clustering analysis is to map

out regions of composition space where the crystal structure is similar. This is done by grouping together materials based on the similarity of their experimental diffraction spectra, and then plotting those groups in composition space. Frequently, the edges of these groups in composition space correspond to structural transitions. The grouping together of similar diffraction patterns also allows one to select a single representative member from the group, thereby greatly reducing the time needed to perform structural analysis on all of the experimental diffraction patterns. This technique is discussed in detail in Chapter 6.

The second multivariate technique discussed is called non-negative matrix factorization (NMF). The idea behind NMF is to back out two pieces of information from the experimental data. First, we are interested in the diffraction patterns of the pure phases (i.e. the individual crystal structures) that are present in all of the experimental diffraction patterns. Second, we are interested in the quantifying the contribution of those patterns to each of the experimental patterns. In general, this technique has the advantage of allowing mixtures of different crystal structures within a given experimental diffraction pattern. The disadvantages are that it is more computationally expensive and the solutions found are not guaranteed to be the best possible solutions. This technique is discussed in detail in Chapter 7.

It is worth noting that we have chosen to study XRD data because of a particular need within our group. However the techniques discussed here are also directly applicable to other types of data from combinatorial libraries. For example, cluster analysis and NMF could easily be applied to spectral data from FTIR, Raman spectroscopy, XPS, and mass spectrometry.

As an example system, we look at a region of the Fe–Ga–Pd ternary system.

5.2 Fe-Ga-Pd Experimental Details

The experimental data we use as an example system in the next two chapters comes from the Fe-Ga-Pd ternary metallic alloy system. Our interest in the Fe-Ga-Pd system stems from the fact that the Fe-Ga and Fe-Pd binary phase diagrams contain compositions with unusual magnetic actuator properties. Fe-Ga is a well known material system exhibiting large magnetostriction for Ga content between 20 and 30 atomic percent. The origin of this property is attributed to the complexity of the Fe-Ga binary phase diagram in this region[73]. $Fe_{70}Pd_{30}$ is a ferromagnetic shape memory alloy (FSMA)[74] whose martensitic transition is associated with a magnetic field induced strain of about 10,000 ppm[75]. Fortunately, Ga and Pd both form disordered crystals when they are substituted into the Fe lattice. This means that they can possibly be substituted into the Fe lattice without disturbing the original crystal structure.

Natural thin film composition spreads of Fe-Ga-Pd are deposited at room temperature using an ultra high-vacuum three gun magnetron co-sputtering system with a base pressure of 10^{-9} Torr (10^{-7} Pa) on 3-inch (76.2 mm) diameter (100) oriented Si wafers. The details of the synthesis procedure can be found in references [55] and [71]. The samples are then post annealed at 650°C for two hours in our sputtering chamber. The base pressure during annealing is 10^{-8} Torr. The total processing time (i.e. deposition and heat treatment) of a composition spread library is roughly 3 hours

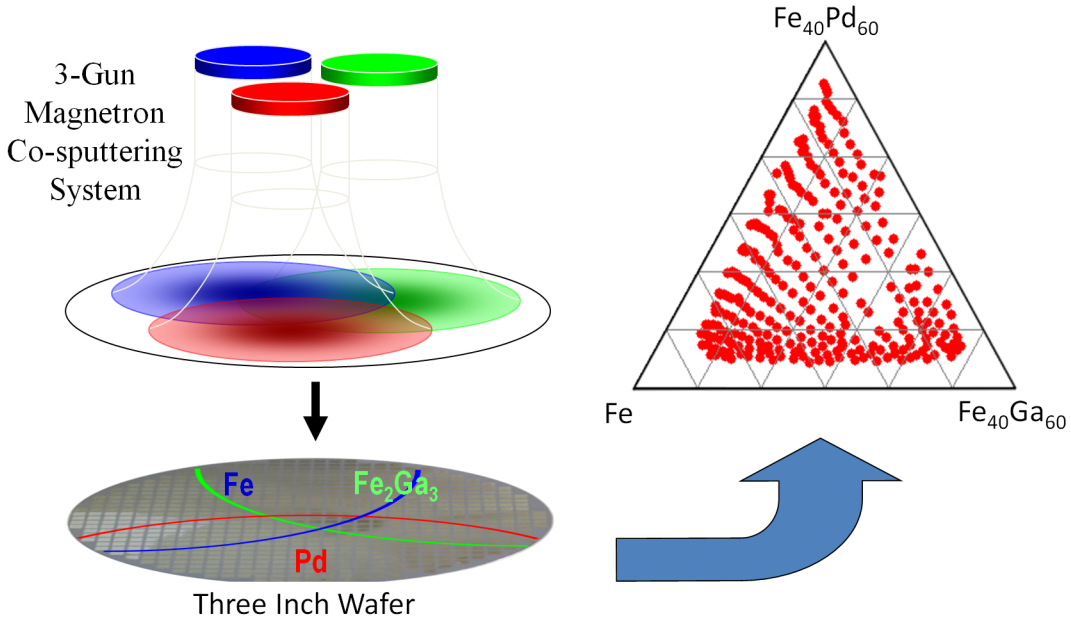

Figure 5.1: Schematic of a thin film composition library made using a 3-gun co-sputtering system. The three targets used in the deposition are Fe, Pd, and Fe_2Ga_3. On the left, a schematic of the deposition profile is displayed; On the right, the region of the phase diagram for which XRD information is obtained from the composition spread library is displayed.

before it is ready for rapid characterization. After the deposition, the composition of the wafer spread is immediately determined via wavelength dispersive spectroscopy (WDS) in atomic percent. This measurement can determine the percent fraction of each atom contained at each point on the wafer to within one percent. Figure 5.1 shows the schematic procedure for the synthesis of a ternary composition spread that covers the relevant part of the phase diagram.

XRD of the fabricated films is performed using the ω-scan mode of a D8 DISCOVER for combinatorial screening (Bruker-AXS). It is equipped with a GADDS two-dimensional detector, which simultaneously captures data for a fixed range of 2θ and ω. The composition spread wafer contains 535 individual 1.75 mm x 1.75

mm squares with continuously changing composition. However, XRD is performed on only 273 of the 535 squares due to time constraints. In order to scan the 2θ range of interest (20 to 90 degrees), microdiffraction is performed in three frames for each square. We use an X-ray beam spot size of 1 mm in diameter. We scan the entire library for one frame before moving to the next frame, so the entire spread library must be scanned three times to cover the entire 2θ range. Once this is accomplished, the microdiffraction data are in the form of 2-D detector images. The raw detector images are then compiled and integrated to obtain the 2θ angles and peak intensities using the D8 GADDS program and a script to automate the process. Figure 5.2 shows the diffractometer used to obtain the diffraction data as well as a sample of the XRD data for the Fe-Ga-Pd ternary system.

Since there is some extraneous information in the XRD spectra (e.g. substrate peaks and background signal) some pre-processing is done on the data before it is analyzed. In particular, background subtraction, cropping, and normalization are performed. Background subtraction is performed by fitting and subtracting a piece-wise polynomial from the data on a spectrum by spectrum basis (i.e. the background determination of one spectrum is not affected by that of any other). After background subtraction, the full measured 2θ range is cropped down to the minimum range such that all of the detected XRD peaks from all the samples (but not from the substrate) are contained in the spectra. For this Fe-Ga-Pd sample, we find that this range is from 37 to 50 degrees.

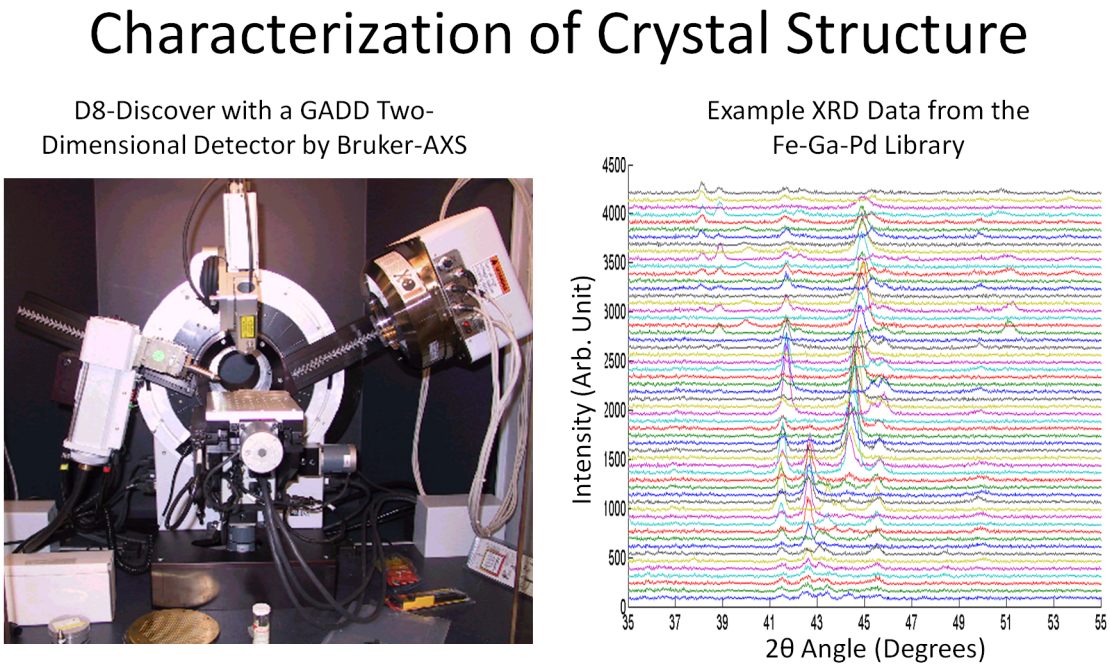

Figure 5.2: An image of the X-ray microdiffractometer used to obtain XRD data for the Fe-Ga-Pd composition spread library. Also shown is a representative subset of the XRD data used to perform cluster analysis and non-negative matrix factorization. The XRD data has been pre-processed to remove the background.

Chapter 6

Agglomerative Hierarchical Cluster Analysis

6.1 Abstract

In this chapter, we discuss a procedure for rapid identification of structural phases in thin film composition spread experiments. As an example system, we focus on a region of the Fe-Ga-Pd ternary metallic alloy system. An in-house scanning X-ray microdiffractometer is used to obtain X-ray spectra from 273 different compositions on a single composition spread library. Agglomerative hierarchical cluster analysis is then used to sort the spectra into groups in order to rapidly discover the distribution of phases on the ternary diagram. The most representative pattern of each group is then compared to a database of known structures to identify known phases. Using this method, the arduous analysis and classification of hundreds of spectra is reduced to a much shorter analysis of only a few spectra.

6.2 Cluster Analysis

Cluster analysis is a technique used to sort objects into groups. Generally, these groups are based on the similarity between the objects that are being sorted, and the number of groups corresponds to the number of classes of objects that are present in the dataset. In our case, our dataset is comprised of materials taken from the Fe-Ga-Pd ternary materials system and we would like to sort these materials according

to their crystal structure.

The process of sorting the spectra into discrete groups consists of deciding on a similarity metric, calculating the similarity between all pairs of spectra, visualizing the similarity matrix, performing cluster analysis to assign the spectra to some number of distinct groups, and then evaluating (and possibly adjusting) the clusters. Once the cluster analysis has been performed, we use the composition information obtained via WDS to draw a ternary diagram. Looking at the distribution of groups on the ternary diagram is akin to looking at a phase diagram, since the groups are based entirely on structure information.

There are many choices one must make along the way to creating this phase diagram. First, one must choose the metric by which the similarity between two spectra is determined. For our case, we chose to use the Pearson correlation coefficient. For two XRD spectra (each of which is represented as a vector of XRD intensities), $\vec{x}$ and $\vec{y}$, with means $\overline{x}$ and $\overline{y}$, the Pearson correlation coefficient takes the form:

$$C_{xy} = \frac{\sum_{i=1}^{n}(x_i - \overline{x})(y_i - \overline{y})}{\left(\sum_{i=1}^{n}(x_i - \overline{x})^2 \sum_{i=1}^{n}(y_i - \overline{y})^2\right)^{1/2}} \tag{6.1}$$

Where C_{xy} is the Pearson correlation coefficient, x_i and y_i are the diffraction intensities at a given diffraction angle, and n is the number of angles at which the diffraction intensity is measured. We compare all pairs of spectra using this metric and arrange this information into a matrix of correlation coefficients, C, the elements of which are C_{xy}. The values of C_{xy} can range from -1 to 1, with a value of 1 indicating an identical pair of spectra, a value of 0 indicating spectra that have no correlation,

and a value of -1 implying that the spectra are anti-correlated. Anti-correlation means that where one spectrum has large values, the other has small values.

In the context of comparing spectra produced by XRD, a correlation coefficient of one means that the peaks in both spectra match up to each other perfectly. If all of the peaks in a pair of XRD spectra match, it is very likely that they have the same crystal structure. A correlation coefficient of zero implies that the peaks in the spectra match up to each other as often as they do not. Such a pair of spectra may have some similarity in their crystal structure. For example they may have the same structure but different crystallinity, or they may correspond to mixtures of the same phases with different volume fractions. In the context of XRD data, a pair of spectra with a correlation coefficient of negative one are very unlikely to share the same crystal structure. This interpretation motivates the definition of a distance matrix, $D = (1 - C)/2$. This matrix contains values ranging from zero to one and represents the dissimilarity among the spectra. A distance of zero between two spectra implies that they are identical, while a distance of one implies that the spectra are unlikely to correspond to the same crystal structure. As long as our choice of similarity metric is a good one, the distance matrix should contain all of the information needed to group the spectra.

The difficulty now lies in trying to understand the relationships among all of the spectra, embodied by the distance matrix, D. To visualize D, each matrix element is interpreted as the distance between two spectra in some Euclidian space. The problem is that this space may have dimensionality as large as n-1, where n is the number of spectra. To see this, first take two points, S_i and S_j, each representing a spectrum.

Place them into a Euclidian space such that they are the distance D_{ij} apart. This is a one dimensional space. Now take a third spectrum, and place it however far it is from the first two (D_{ki} and D_{kj} respectively). The three points form a triangle in two dimensional space. Repeating this process again with another spectrum produces a triangular pyramid in three space. At this point, we can't necessarily fit another point into this space and satisfy the demands that it be the appropriate distance from each other point and that we only use three dimensions. However, we could try to put it in the best possible location such that its distance from each of the other points is the best possible approximation to the actual distances listed in the matrix D. This discards some of the similarity information. However, it gives us a way to visualize the correlation matrix in ordinary three dimensional space. The question now is: how, using three dimensions, can one come up with the best possible approximation of the distribution of these points? This is a classic problem in reducing the dimensionality of a data set. To reduce the dimensionality of a distribution of points in a high dimensional space, we can use principal component analysis (PCA) or we can use metric multi-dimensional data scaling (MMDS). The mechanics of how to perform these techniques are well documented[76, 77] and we will not discuss them here. In this work, we use MMDS to find the best possible (three dimensional) approximation to the (n-1 dimensional) distribution of points embodied by the distance matrix. For the Fe-Ga-Pd system, the three dimensional representation of the distance matrix as approximated using MMDS appears in Figure 6.1. A 3D animation of the plot is also available at www.combi.umd.edu.

Looking at the distribution of points in the MMDS plot, one could start to visually

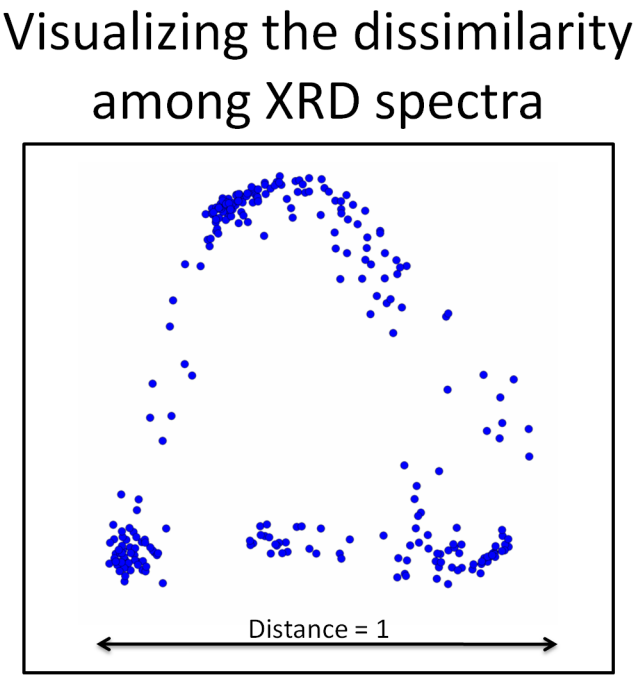

Figure 6.1: A two dimensional representation of the 272 dimensional distribution of points corresponding to the distance matrix. Each point represents a diffraction spectrum. The distance between a pair of points corresponds to the dissimilarity between the corresponding pair of diffraction spectra. This means that spectra that are similar are separated by small distances. Tight groupings of points, such as the those visible in the lower left corner, have similar diffraction spectra and are therefore likely to have the same crystal structure. More elongated distributions, such as the arch of points in the top half of the figure, indicate that there is at least one systematic change occurring in the diffraction spectra as one moves across the arch. For example, such an arch could be caused by a shift in one diffraction peak (a changing lattice constant caused by chemical substitution in the lattice). In the case of a peak shift, adjacent points in the arch correspond to spectra where the peaks are nearly aligned (highly similar spectra), while the points on opposite ends of the arch correspond to spectra that are maximally shifted (and are therefore highly dissimilar spectra).

divide the spectra into discrete groups. However, this process would be somewhat subjective. A more rigorous mathematical method for deciding which spectra to group together is to use a agglomerative hierarchical cluster analysis[78]. Agglomerative hierarchical cluster analysis begins with each object is in its own group. One then proceeds by finding the two groups that have the smallest distance between them and lumping those two groups together to form a new group. This process is repeated until all objects are members of a single group.

This grouping information in agglomerative hierarchical cluster analysis is generally represented using a dendrogram. A dendrogram for the Fe-Ga-Pd system is shown in Figure 6.2. Along the x-axis, each spectrum is represented by a vertical line. At some height, these lines all connect. The height at which they connect is determined by the distance between the spectra, with larger heights corresponding to larger distances. If some spectra are already connected, then the height represents the distance between groups of spectra. To get an intuitive idea of how this dendrogram is made, first take the two most similar spectra and put them in a group together. This is done by connecting them on the dendrogram with a horizontal line at a height corresponding to the distance between them, as described in the distance matrix. In order to proceed further, we next determine the distance between this group of spectra and all of the other spectra. The way that this group-to-group distance is defined is called the linkage method. One of the ways to define the distance between one group of spectra and another is to compute the average of the distances from all of the members of the first group to all of the members of the second group. This is called the group average linkage method, and it is the method used to produce the

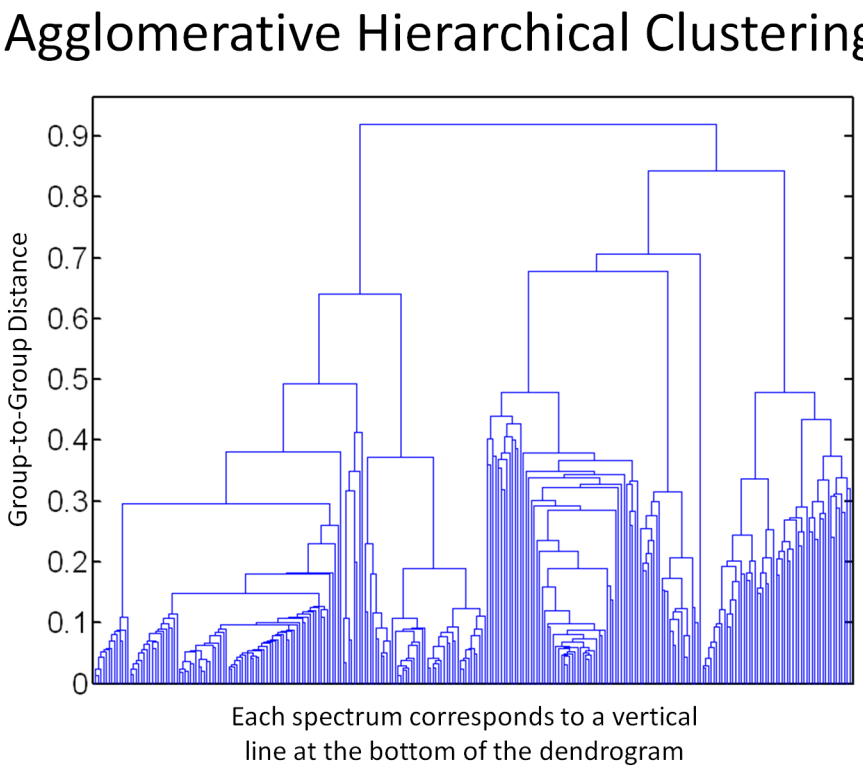

Figure 6.2: A dendrogram representing possible groupings of XRD spectra. Each XRD spectrum is a represented by a vertical line at the base of the dendrogram. The grouping of spectra into larger and larger groups is represented by joining these vertical lines together using horizontal tie lines. The height at which two vertical lines are joined represents the distance between the groups of spectra to be joined, with larger heights corresponding to larger distances. In this figure, the distance between any two groups of spectra is calculated using the average distance from all the members of the first group to all the members of the second group.

dendrograms in Figures 6.2 and 6.3. The process of agglomerating groups is then repeated, each time merging groups of spectra that are more and more dissimilar. Eventually, at the top of the dendrogram, there is only one group.

If one were to stop making groups at some threshold group-to-group distance, then one would be left with a number of groups. This threshold group-to-group distance is called the cut level. By adjusting the cut level, one can adjust the number of groups. If each of these groups is assigned a color, then it is possible to look again at the MMDS plot, with the points colored as they fall into the different groups. Figure 6.3 shows several dendrograms at different cut levels along with the associated groupings of samples in the MMDS plot and on the ternary composition diagram.

If the data fall into well separated clusters in the MMDS plot, then there should be some level in the dendrogram where there is a big step in the linkage height. That is, at some point, there will be a link whose height is clearly larger than all of the links below it. This is where we place our cut level. We can verify that the clusters are reasonable by looking at the clusters in the MMDS plot. If points that qualitatively look like they should form a cluster have indeed been grouped together, then we can have a good degree of confidence in our result. In our case, we choose a cut level of .55. This cut level is shown in the third row of plots in Figure 6.3. For this cut level, the MMDS plot shows three more or less spherical clusters (green, purple, and yellow) and two "boomerang" shaped clusters (red and blue).

Let us first discuss the spherical clusters. Since points that are close together on the MMDS plot correspond to similar spectra, a spherical group should correspond to a single crystal structure. Indeed, our expectation of spherical clusters was the reason

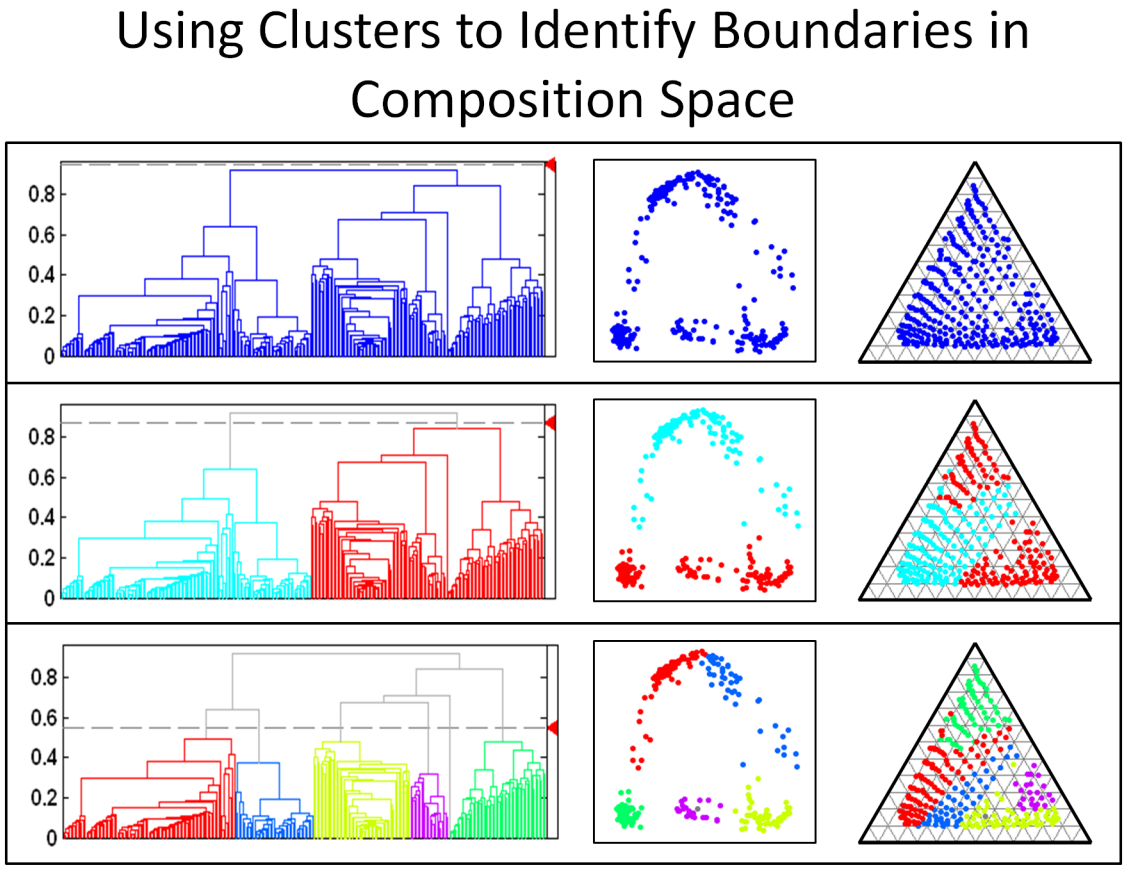

Figure 6.3: Choosing different dendrogram cut levels partitions the samples into different groups. On the left, dendrograms are displayed with cut levels at a group-to-group distance of .87, .83, and .55. The corresponding groups formed at these cut levels are displayed on MMDS plots as well as on the composition diagram.

that we chose the group average linkage method, which tends to create spherical clusters. The reason that all of the points in a spherical group do not collapse to a single point is that there is noise in the spectra, causing some small distance between spectra, even if they correspond to exactly the same crystal structure.

The MMDS plot also contains some arc-like distributions of points. An arc of points represents spectra that are all related to each other, but which are undergoing some systematic change as a function of position along the arc. For example, this may correspond to a set of samples across which a diffraction peak slowly shifts (i.e. a change in a lattice parameter), or it may correspond to a set of samples with a slowly varying mixture of phases.

The group average linkage method is perhaps not an ideal linkage method because it tends to break up the non-spherical clusters. There is a linkage method that is less sensitive to the shape of the group, called the single link method. In this linkage method the distance between two groups of objects is defined to be the distance between the two objects (one from each group) with the minimum distance between them. Applying this method to our data preserves the arc as a single group. Unfortunately, this linkage method is also very sensitive to variations in the signal to noise level among the spectra, as well as the uniformity of sampling in composition space. These sensitivities result in the formation of many small groups, which doesn't fit with our goal of sorting the spectra by crystal structure. We have also tried several other linkage methods, namely the weighted group average method (a.k.a. weighted pair-group method with averaging, or WPGMA), the centroid method (a.k.a. unweighted pair-group method using centroids, or UPGMC), the median method (a.k.a. weighted

pair-group method using centroids, or WPGMC), the complete link method (farthest neighbor), and the ward method (minimum total pair-wise squared distance), all of which gave similar results to the group average linkage method. A new linkage method that is a combination of the group average and single link methods would be ideal, but is left as future work.

Now that we have divided the samples into groups by adjusting the cut level, we would like to confirm that the groups are reasonable by comparing the groupings to the XRD data. We can do this by looking at the XRD spectra as a function of composition as we move across the boundary from one group to another. Figure 6.4 shows two representative examples of such an analysis. In part (a), we see that as we move from the red group to the green group, there is a clear transition in the diffraction spectrum. The peaks present in the red group vanish, and a different set of peaks corresponding to the green group appear. This boundary corresponds to a structural phase transition. In contrast, when we cross the boundary from the red to the blue group, there is no such transition. Instead, we see that there is in fact a single peak that is changing position. Looking back at the bottom of Figure 6.3, we see that the red and blue groups are created by breaking the arc of points visible in the MMDS plot, while the red and green groups are more well separated. Again, we have encountered an error caused by the inadequacy of our linkage method.

As an alternative to developing a new linkage method, we have modified our dendrogram by hand to create three arc-like groups out of the two boomerang-like groups in Figure 6.1. In order to modify the dendrogram in this way, we used PolySNAP, which is software designed for analysis of powder diffraction data. The new dendro-

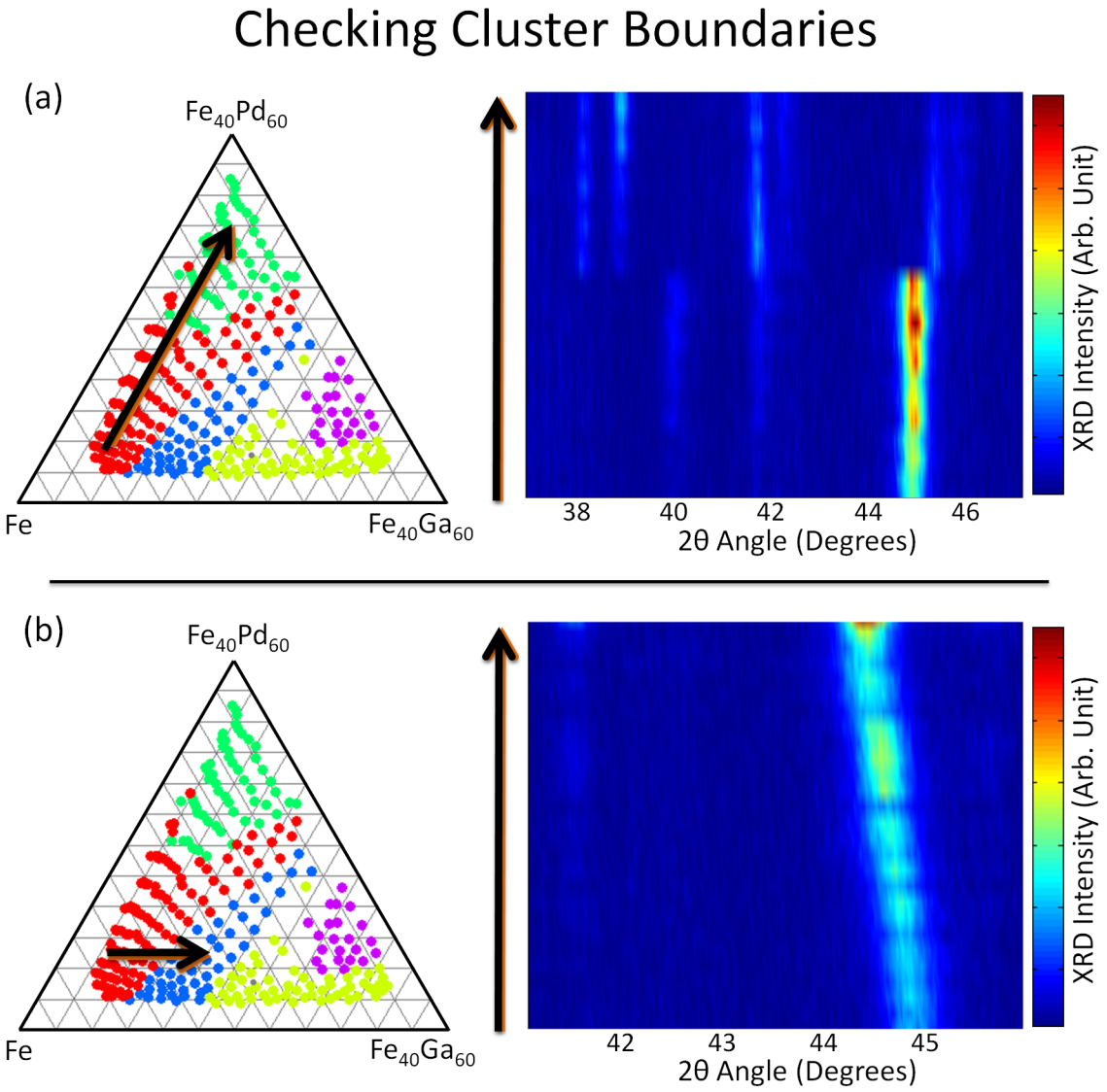

Figure 6.4: Part (a) shows an example of a crystal structural transition across the boundary between the red and green groups. The left plot of part (a) shows a composition diagram with an arrow marking a set of samples. The right of part (a) shows the XRD spectra of all of the compositions under the arrow on the composition diagram, arranged in order along the arrow. Part (b) shows a pair of similarly constructed plots, except this time the transition from the red to blue group does not correspond to a structural transition, but is in fact caused by a change in lattice parameter.

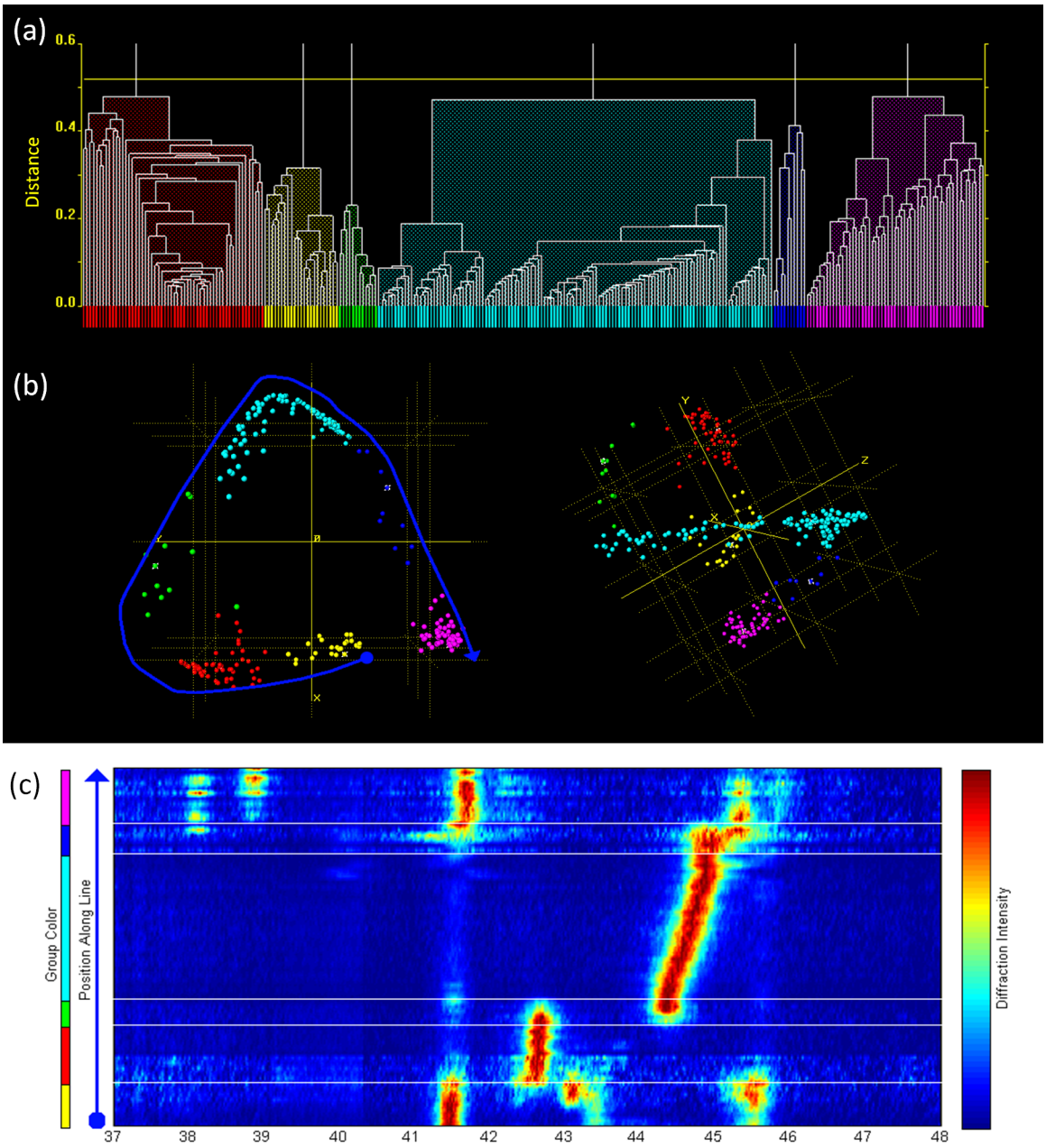

Figure 6.5: A modified dendrogram where the 'arms' of the arc are separated into separate groups. (b) Two views of a 3D MMDS plots showing the distribution of the groups created using the modified dendrogram. (c) The XRD data as a function of position along the blue line.

gram and the resulting distribution of groups in the MMDS plot are shown in Figure 6.5(a) and 6.5(b) respectively. In order to verify that this clustering is reasonable, we follow a path along the distribution (see the blue line in Figure 6.5(b)) and plot the XRD data as a function of position along this line (Figure 6.5(c)). This allows us to see the relationship between the groups that we have created and the actual XRD data. It is clear when looking at the XRD data that the yellow, red, cyan, and magenta groups correspond to unique patterns, while the green and blue groups correspond to transitions from one pattern to another. Furthermore, the cyan group in Figure 6.5 corresponds to spectra that are all of the same phase, but with a peak that is continuously shifting.

From this analysis, we can conclude that using the Pearson correlation coefficient as our similarity metric to create a distance matrix, and visualizing that matrix using MMDS, we can identify clusters of spectra that correspond to unique patterns. In particular, spherical clusters in the MMDS plot correspond to a single pattern, while an arc in the MMDS plot may correspond to a to a transition between two patterns, or to a single pattern where one of the peaks is continuously shifting. Once the clustering analysis is completed, we can move on to identification of the actual crystallographic phases represented by the clusters.

6.3 Results for the Fe-Ga-Pd Ternary System

Identification of known phases was done by comparing the XRD spectrum of the most representative member (i.e. the member with the smallest average distance

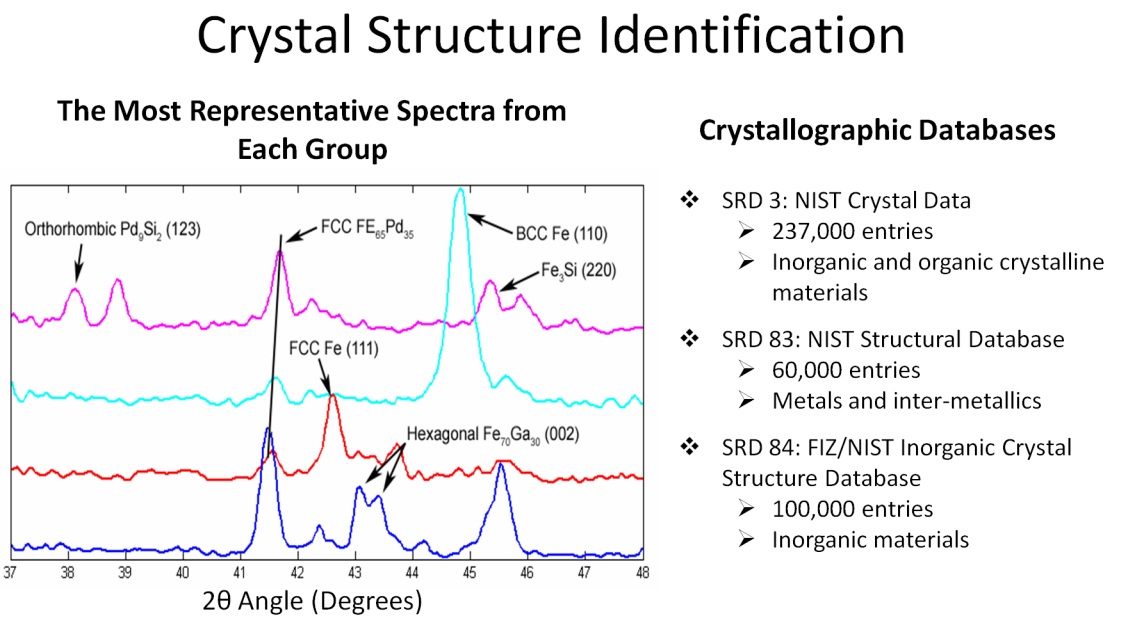

Figure 6.6: The most representative patterns in the yellow, red, cyan, and magenta groups from Figure 6.5. The clustering approach reduces the problem of going through hundreds of spectra and identifying every peak in every pattern to just deciphering the meaning of these few patterns. The peaks are labeled if a possible match to known samples from the NIST crystallographic database was found.

to all other members) of a group of spectra to a set of reference spectra from the crystallographic databases available at NIST. In particular, we used the Inorganic Crystal Structure Database (ICSD), which contains more than 90,000 entries; and the NIST structural database, which contains more than 60,000 entries[79]. The matching conditions we used were as follows: if the composition of the reference pattern was within (or very near) the composition space spanned by a group of XRD spectra, and the peaks were separated by less than 0.4°, then we considered this to be a match.

Figure 6.6 shows a plot of the most representative members of the yellow, red, cyan, and magenta groups. The identified structures denote the basic crystal struc-

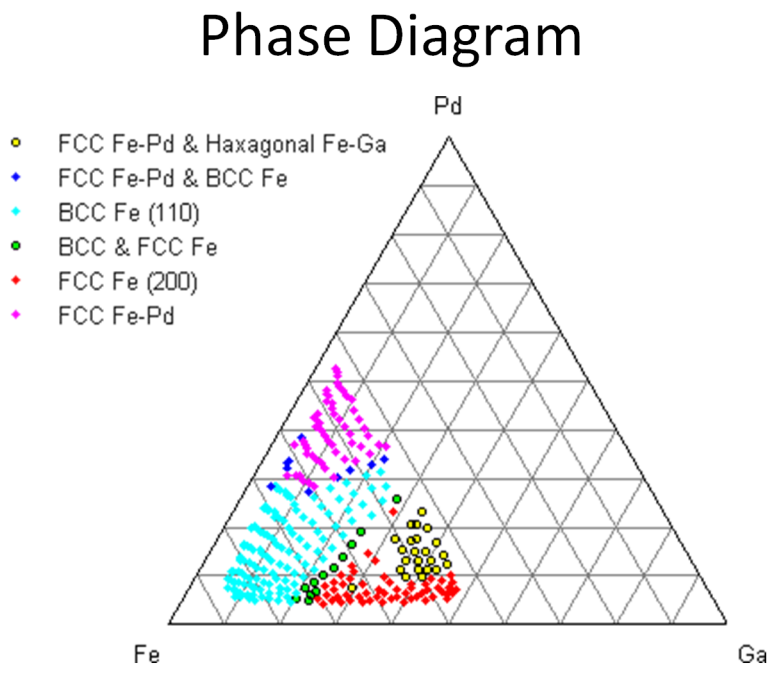

Figure 6.7: The structural phase diagram for the sampled portion of the Fe-Ga-Pd ternary composition space. The compositions are grouped according the the similarity of their diffraction patterns using cluster analysis. The crystal structures are identified by comparing the most representative patterns from each group with a database of reference patterns.

tures of each region. The green and blue groups are not displayed since they represent mixtures of the phases present in the other groups. We would like to note that in some cases, there was no match identified from the database.

Putting the clustering, phase identification, and composition information together yields a map of the distribution of phases for the explored region of the phase diagram (Figure 6.7). We also note that the blue and green groups, which we interpreted as transitions from one phase to another based on the plots in Figure 6.7, do indeed fall along the borders of the other phases. Although the full ternary phase diagram of this system is not available for comparison, the projection of the identified distributions to the two binary (Fe-Ga and Fe-Pd) systems matches the known phase diagrams

reasonably well. According to the published equilibrium phase diagrams, in the Fe-Ga system[80], starting from the pure Fe end, the α-Fe phase persists up to about 80% Fe, beyond which various mixture regions containing the Fe-Ga $L1_2$ phase stretches up to about 50% Fe. The $L1_2$ phase has an FCC structure, which in our study was correctly identified as being isostructural to FCC Fe. In the Fe-Pd system[81], a mixture of α-Fe and $Fe_{0.5}Pd_{0.5}$ (FCT) is known to extend from 100% Fe to about 50% Fe. It is expected that this region would predominantly "appear" as mainly α-Fe. In our study, we find that at approximately $Fe_{0.65}Pd_{0.35}$, the dominant phase switches from α-Fe to FCC $Fe_{0.65}Pd_{0.35}$, which stretches beyond 50% Fe. Our analysis has identified this region (starting at the correct composition) as the FCC $Fe_{0.65}Pd_{0.35}$, which we believe is a quenched phase.

6.4 Conclusion

Combinatorial analysis frequently deals with large datasets that contain a significant amount of degenerate information. This is certainly the case for XRD data from combinatorial data sets, where the crystal structure of many samples is nearly identical. In this chapter we have shown that the application of dimensionality reduction and visualization techniques such as MMDS can help to identify which samples are similar, and thereby speed up the process of mapping out structural phase diagrams. Using agglomerative hierarchical clustering, the process of sorting XRD spectra into groups that correspond to individual crystal structures can be greatly accelerated. By selecting the most representative member of each group of spectra, the arduous

analysis and classification of hundreds of spectra is reduced to a much shorter analysis of only a few spectra.

Chapter 7

Non-negative Matrix Factorization

7.1 Abstract

In this chapter we apply a technique called Non-negative Matrix Factorization (NMF) to the problem of analyzing hundreds of X-ray microdiffraction (XRD) patterns from a combinatorial materials library. An in-house scanning X-ray microdiffractometer is used to obtain XRD patterns from 273 different compositions on a single composition spread library. NMF is then used to identify the unique XRD patterns present in the system and quantify the contribution of each of these basis patterns to each experimental diffraction pattern. As a baseline, the results of NMF are compared to the results obtained using Principle Component Analysis (PCA). The crystal structures of the basis patterns found using NMF are then identified using comparison to reference patterns from a database of known structural patterns. As an example system, we explore a region of the Fe–Ga–Pd ternary system. The use of NMF in this case reduces the arduous task of analyzing hundreds of XRD patterns to the much smaller task of identifying only nine XRD patterns.

7.2 Introduction to NMF

NMF is a relatively new technique that has been applied to problems in several fields. NMF has been used to perform image segmentation,[87] document clustering,[88]

and spectral un-mixing of satellite reflectance data,[89] among other applications. To the best of the authors' knowledge, this is the first time that it has been applied to XRD data. The basic idea of NMF is to deconvolve a large number of non-negative spectral patterns into a smaller number of non-negative basis patterns. The experimental patterns can then be described as a weighted superposition of the deconvolved basis patterns. We have two main reasons why we have chosen to use NMF over other multivariate techniques. First, since NMF describes experimental spectra as a superposition of basis patterns, it can easily handle diffraction patterns that result from mixtures of different crystal structures. This makes NMF a good choice when compared to techniques that sort patterns into discreet groups. NMF therefore represents a significant improvement over our previous work using agglomerative hierarchical cluster analysis.[84] Second, NMF produces basis patterns that can be directly interpreted as diffraction patterns. This makes NMF a more suitable technique when dealing with XRD data in comparison to principal component analysis (PCA) since PCA produces basis patterns that contain negative values.

7.3 NMF of XRD Data

In order to perform the factorization, the XRD data were arranged into an m-by-n matrix, Y, where m is the number of compositions for which XRD patterns were measured (m=273 in this case) and n is the number of angles at which the diffraction intensity was recorded. In this case, the diffraction intensity was measured every 0.02° over the 2θ range from 37° to 50°, so n=651. NMF was then used to find an

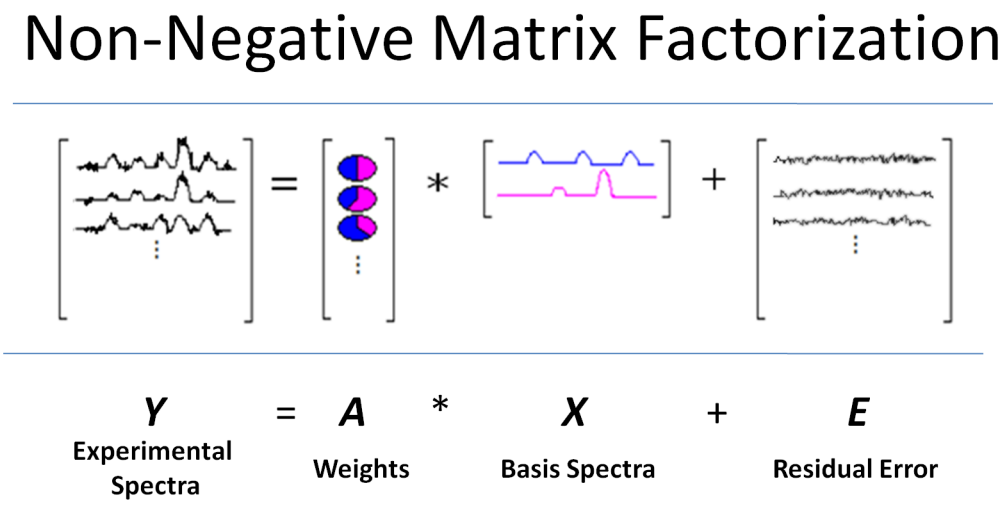

Figure 7.1: The basic idea of NMF is to deconvolve the experimental spectra into a smaller number of basis spectra. The experimental spectra can then be written as a superposition of these basis spectra.

approximate factorization of Y into the product of two smaller matrices, A and X. The matrices A and X are constrained such that they may only contain non-negative values. Any noise in the experimental data or errors in the factorization get accounted for by an error matrix, E, which may contain negative values.

$$Y = AX + E, \text{ Where } A_{ij} \geq 0, \text{ and } X_{ij} \geq 0 \tag{7.1}$$

Figure 7.1 shows a schematic of this equation. The size of matrix A is m-by-r, the size of matrix X is r-by-n, and the size of matrix E is m-by-n, where r is the rank of the factorization. The rank of the factorization corresponds to the number of basis patterns that are to be extracted from the experimental data, and is chosen by the user of the algorithm. Choosing the correct value for r requires some consideration and is discussed below in the comparison of NMF to PCA. For the XRD data set presented

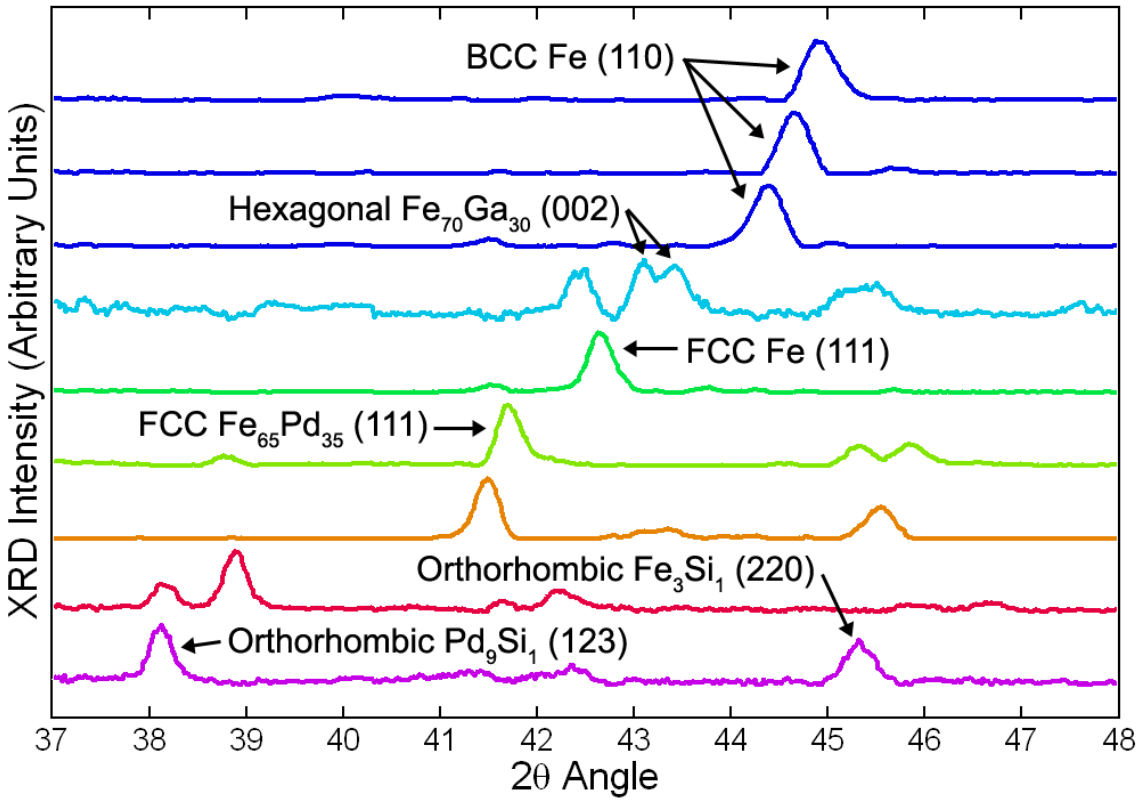

Figure 7.2: The nine basis patterns found using NMF. The patterns are color coded by structural phase. Peaks identified as possible matches to reference patterns are labeled. The spectra are offset vertically for visibility.

here, we found that a rank nine factorization produced a good deconvolution of the experimental diffraction patterns.

Each row of the matrix X contains a basis pattern. Each basis pattern contains a set of peaks that tend to appear together in the experimental data. After the factorization is completed, the basis patterns are normalized such that the largest value in each spectrum is unity. The content of the matrix X is presented in Figure 7.2.

Each row of the matrix A contains the weights, or linear mixing coefficients, of the basis patterns for a particular experimental pattern. Since the basis patterns are

normalized to unit intensity, each matrix element in A corresponds to the intensity of a given basis pattern for a particular experimental pattern. In Figs. 7.3 and 7.6, the relative weights of the basis patterns for a given composition are represented using pie charts. The size of each piece of a pie chart corresponds to the amount of each basis pattern present in a given sample.

Each row of the matrix AX contains a deflated version of an experimental spectrum. The spectra are said to be deflated because there is typically a much smaller number of degrees of freedom in the matrix AX than there is in the matrix Y. The number of degrees of freedom in the matrix AX is the number of matrix elements in A plus the number of matrix elements in X. In contrast, the number of degrees of freedom in Y is the number of matrix elements in Y. For example, in the data set explored here, there are 177,723 matrix elements in Y, but only 8,316 matrix elements for a rank nine factorization AX. Thus, the dimensionality of the parameter space for the deflated matrix AX is less than 5% of that for the experimental data. Ideally, the only difference between the experimental spectra and the deflated spectra should be that the deflated spectra contain much less noise.

Each row of the matrix E contains a residual spectrum, which is the difference between an experimental pattern and the corresponding deflated pattern. Ideally, after the factorization, the residual spectra should only contain noise.

Finding the best solution for A and X is equivalent to minimizing the norm of the error matrix. The problem to be solved by the NMF algorithm can thus be stated as: find A and X such that $\| E \| = \| Y - AX \|$ is a minimum. There are several possible ways of calculating the norm of E and also several possible NMF algorithms

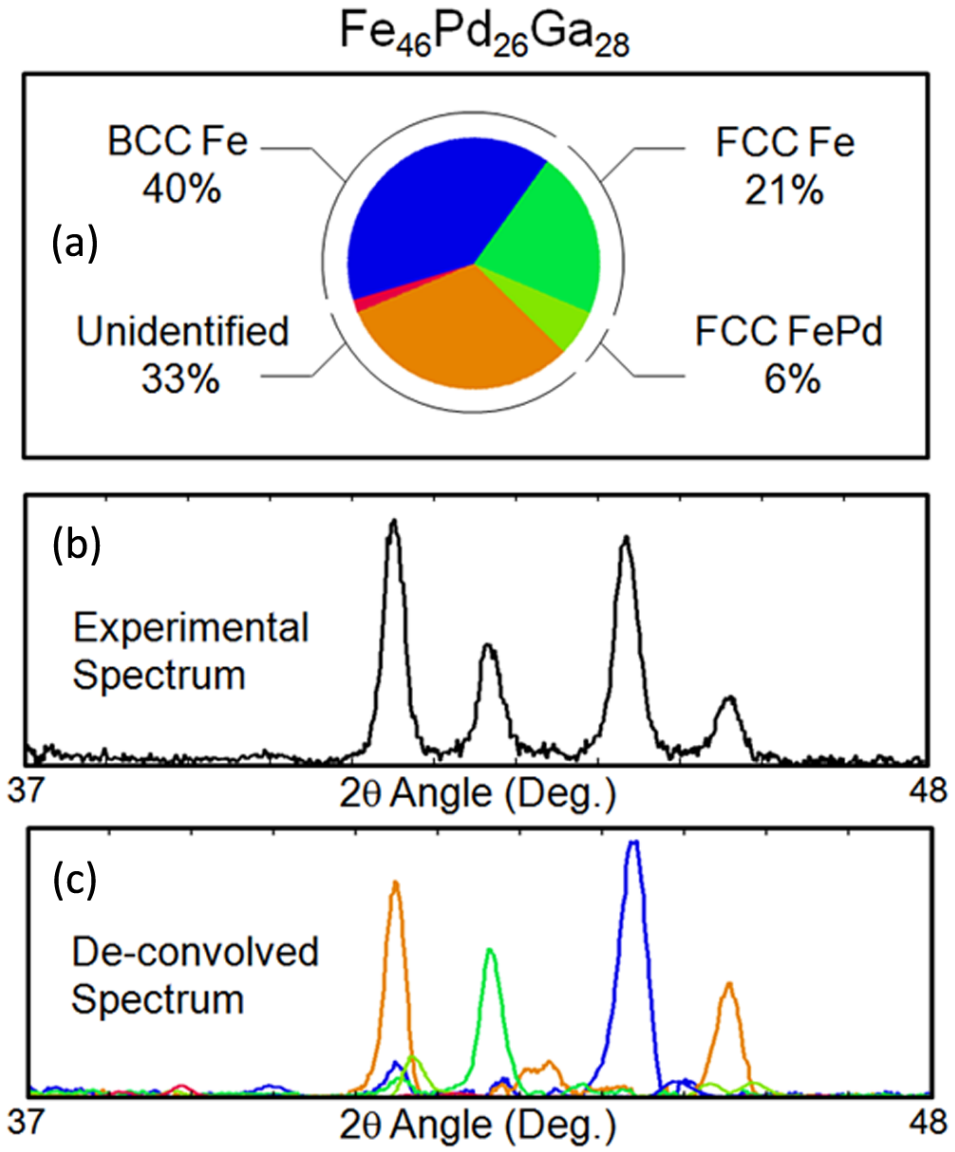

Figure 7.3: Part (a) shows the weights of the basis patterns that are present the sample with nominal composition of $Fe_{46}Pd_{26}Ga_{28}$. Part (b) shows the experimental XRD pattern for this sample. Part (c) shows the weighted basis patterns, which provide a deconvolution of the experimental pattern.

for finding A and X such that E is minimized. In this work, we calculated the norm of E using the squared Frobenius norm, which is simply the sum of the squared matrix elements. An exhaustive discussion of NMF algorithms is beyond the scope of this work and can be found elsewhere.[90] For our work, we used the regularized alternating least-squares algorithm[91] to calculate A and X. The software used to perform the factorization was NMFLAB,[92] which is a third party toolbox for MATLAB.

7.4 Comparison of NMF to PCA

In order to validate the results of the NMF, we must be assured that the NMF algorithm has converged to a global minimum of $\|E\|$, and not merely a local minimum or stationary point. Unfortunately, one of the current limitations of NMF is that convergence to a global minimum is not guaranteed. In order to show that the factorization has converged to very near the global minimum, and in order to choose the correct rank of the factorization, we compare the results of NMF to those of PCA.

The relevant feature of PCA for this work is that for a given rank, PCA finds a matrix factorization that produces the global minimum of the squared Frobenius norm of the error matrix. That is to say, when representing experimental spectra as a linear superposition of basis patterns, PCA produces the best possible approximation to the data using a given number of basis patterns. Since PCA produces a factorization with the minimum possible amount of error, we can assess the quality of the factorization produced using NMF by comparing the amount of information captured by NMF to

the amount of information captured using PCA.

It is worth noting that even though PCA produces a matrix factorization that minimizes the Frobenius norm of the error matrix, it does not produce basis patterns that are physically realizable diffraction patterns. Specifically, the basis patterns produced using PCA contain negative values and are all orthogonal to each other. This is not consistent with the solution we are looking for since the diffraction patterns of a set of crystal structures will only contain positive values and are very unlikely to be orthogonal. For this reason, the basis patterns produced by PCA do not form a useful deconvolution for our work. In contrast, the basis patterns produced using NMF contain only non-negative values and are not constrained to be orthogonal. Thus, they are ideally suited for the task of deconvolving diffraction patterns. Figure 7.4 presents a direct comparison of the basis patterns produced using NMF and PCA.

A comparison of the amount of experimental data accounted for as a function of the number of basis patterns using both PCA and NMF is presented in Fig. 7.5. The amount of error in the factorization is found by calculating the ratio of the absolute area of all of the residual spectra to the area of all of the experimental spectra.

$$Percent\ Represented = 100 * \left[1 - \sum_{i=1}^{n}\sum_{j=1}^{m} \mid Y_{ij} - (AX)_{ij} \mid / \sum_{i=1}^{n}\sum_{j=1}^{m} Y_{ij}\right] \qquad (7.2)$$

The first point to observe in Fig. 7.5 is that below about 20 basis patterns, the percent of data explained using NMF is very close to the amount of data explained using PCA. Thus, in this low-rank region we can be satisfied that the employed NMF algorithm has converged to a point that is very near the global minimum of the

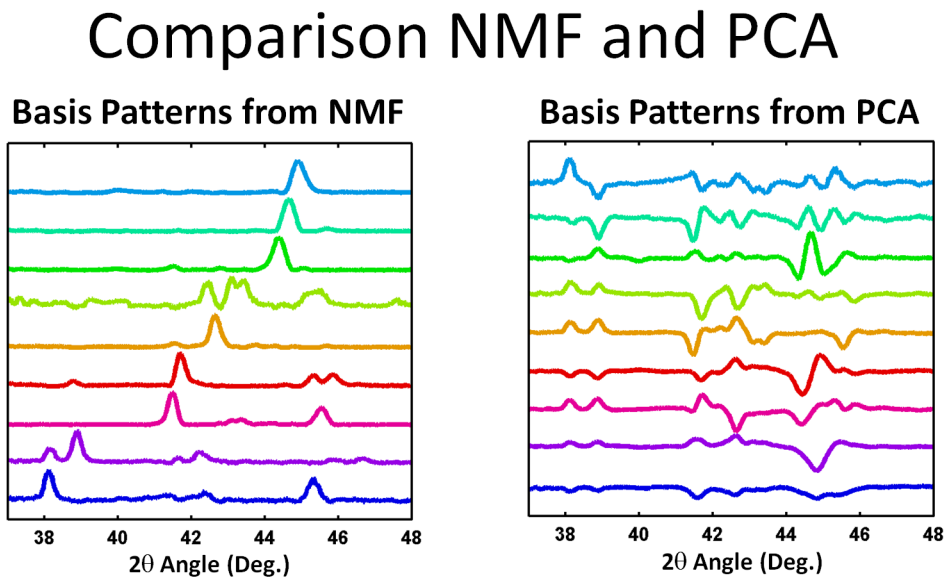

Figure 7.4: A comparison of the basis patterns produced for a rank 9 factorization of the experimental spectra using NMF and PCA. The basis spectra produced using NMF are directly interpretable as XRD spectra, whereas those produced using PCA contain negative values, making their interpretation unclear.

norm of the error matrix. Above 20 basis patterns, the amount of data explained by NMF begins to diverge from the amount explained by PCA, and can even decrease compared to lower rank factorizations. We believe that this decrease is due to the NMF algorithm falling into a local minimum of the norm of the error matrix instead of converging to the global minimum.

There are techniques available that can reduce the tendency to fall into local minima, although none guarantees that the minima are avoided altogether. The most common approach is to choose many different random initializations for A and X, run NMF using each one, and then keep the best result.[90] Another possibility is to pass the results of one NMF algorithm to another algorithm in the hope that they do not both get stuck in the same minimum.[93] Yet a third approach is to choose the

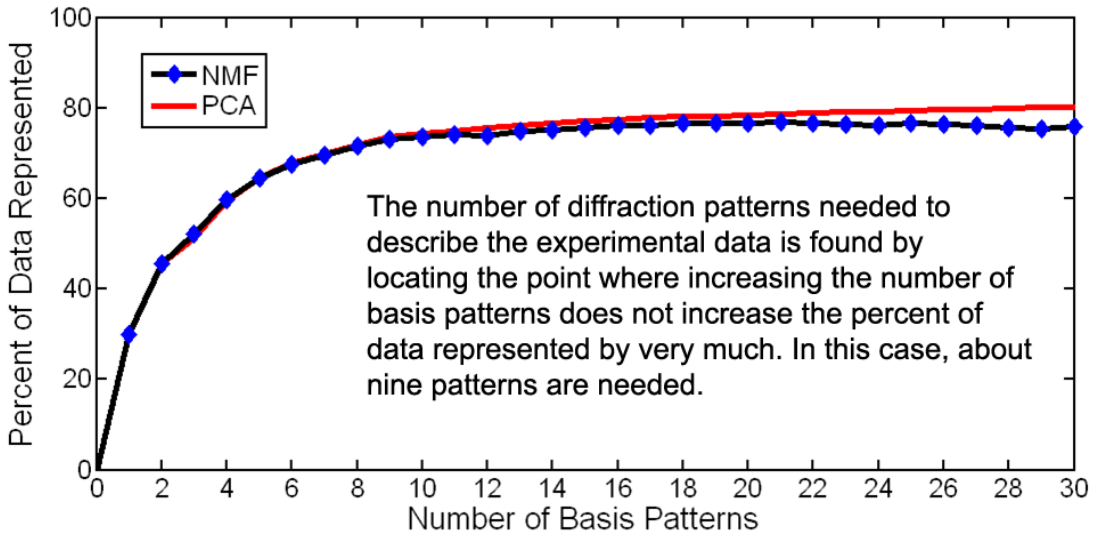

Figure 7.5: The graph above shows the percent of experimental data that can be represented using a given number of basis patterns. The fraction of the data accounted for using NMF is very near that accounted for using PCA, implying that the factorization produced by NMF is valid. The reason why 100% of the data is not accounted for by the factorizations is that there is noise in the experimental data. In this case, noise accounts for about 20% of the experimental data.

initialization of A and X such that they are already near the global minimum.[94, 95] For our case, we are most interested in the low rank factorizations where the local minima did not pose a problem. As a result, we have not focused here on trying to avoid these local minima.

In order to produce an accurate factorization of the experimental data, the correct rank of the factorization must be determined. Determining the correct rank of the factorization corresponds to determining the number of unique patterns that exist in the data. Choosing a rank that is too small will result in basis patterns that are composed of mixtures of pure phase patterns. Choosing a rank that is too large may result in the pattern from a single structural phase being broken up into several basis patterns, each of which contains a subset of the reflections from that structure.

Ideally, by choosing the rank of the factorization to match the number of structures, each basis pattern should represent the diffraction pattern of a single crystal structure. We note that there are some cases where each basis pattern will not represent the diffraction pattern of a single crystal structure. These cases are discussed in Section 7.6.

Using Figure 7.5 we can estimate how many patterns are needed to describe the data. We do this by determining the point where increasing the number of basis patterns does not increase the amount of data explained by very much. In the case of the Fe–Ga–Pd data set, this occurs at about nine basis patterns for both PCA and NMF.

7.5 Discussion & Results for the Fe-Ga-Pd Composition Spread

In Figure 7.2, one can see the nine basis patterns found using NMF for this system. There are several features of these patterns that are worth discussing. The first is that there are several patterns that are only present as mixtures in the experimental data, but show up as separate patterns in the extracted basis patterns. This shows that NMF can identify the correct basis patterns even when there are no end-members present in the data set.

The second feature to note is that in the case of BCC Fe, the NMF algorithm extracts several different patterns that correspond to the same structure but where the position of the peak has shifted. This is one limitation of the NMF algorithm. Since the algorithm has no way of accounting for peak shifts, it identifies each shifted

pattern as a new pattern. In this case, it is up to the materials scientist to identify that the shifted patterns do not correspond to several different structures, but in fact correspond to a single structure that exhibits a change in lattice parameters as a function of chemical composition.

The noise level of the basis patterns is also significantly lower than that present in the experimental patterns. The noise level in any given basis pattern depends on two things. First, it depends on the noise level of the experimental patterns on which it is based. Second, it depends on the number of experimental patterns on which it is based. In general, if a given basis patterns is based on n experimental patterns, then it should have a noise level that is $1/\sqrt{n}$ compared to the noise level of the experimental patterns. In this particular data set, there is considerable variation in the noise level in the experimental data and considerable variation in the number of experimental patterns represented by each basis patterns. As a result of this variation, not all of the basis patterns have better statistics than all of the experimental spectra. For example, the fourth basis pattern from the top in Figure 7.2 has worse statistics than the experimental pattern in Figure 7.3(b) because the basis pattern in Figure 7.2 is based on a smaller number of experimental patterns and those patterns also have a relatively low signal to noise level for the data set.

In order to identify the structural phases corresponding to the basis patterns found using NMF, the basis patterns were compared to a set of reference spectra calculated from the crystallographic databases available at NIST. In particular, we used the Inorganic Crystal Structure Database ICSD[79] and the NIST Structural Database.[96] If the composition of the reference pattern was within or very near the composition

space where a given basis pattern was prevalent, and the peaks were separated by less than 0.4°, then we considered this to be a match. We note that several of the peaks present in the basis patterns produced by NMF contain unidentified peaks. The main reason that not all of the diffraction peaks were identified using this method is that there are a limited number of reference patterns available for comparison in the crystallographic databases. The number of available reference patterns is especially sparse as one moves away from the binary edges of the ternary diagram.

Figure 7.6 presents a ternary diagram in which the weights of the NMF basis patterns for each composition have been represented as pie charts. Since the basis patterns found using NMF correspond to structural phases, this diagram gives us a quantitative distribution of structural phases as a function of composition, including the existence of multiphase regions.

Although the full ternary phase diagram of this system is not available for comparison, the projection of the identified distributions to the two binary Fe–Ga and Fe–Pd systems matches the known phase diagrams reasonably well. According to the published equilibrium phase diagrams, in the Fe–Ga system,[80] starting from the pure Fe end, the α-Fe phase persists up to about 80% Fe, beyond which various mixture regions containing the Fe–Ga $L1_2$ phase stretches up to about 50% Fe. The $L1_2$ phase has an FCC structure, which in our study was correctly identified as being isostructural to FCC Fe. In the Fe–Pd system,[81] a mixture of α-Fe and $Fe_{50}Pd_{50}$ is known to extend from 100% Fe to about 50% Fe. It is expected that this region would "appear" as mainly α-Fe. In our study, we find that at approximately $Fe_{65}Pd_{35}$, the dominant phase switches from α-Fe to FCC $Fe_{65}Pd_{35}$, which stretches beyond 50%

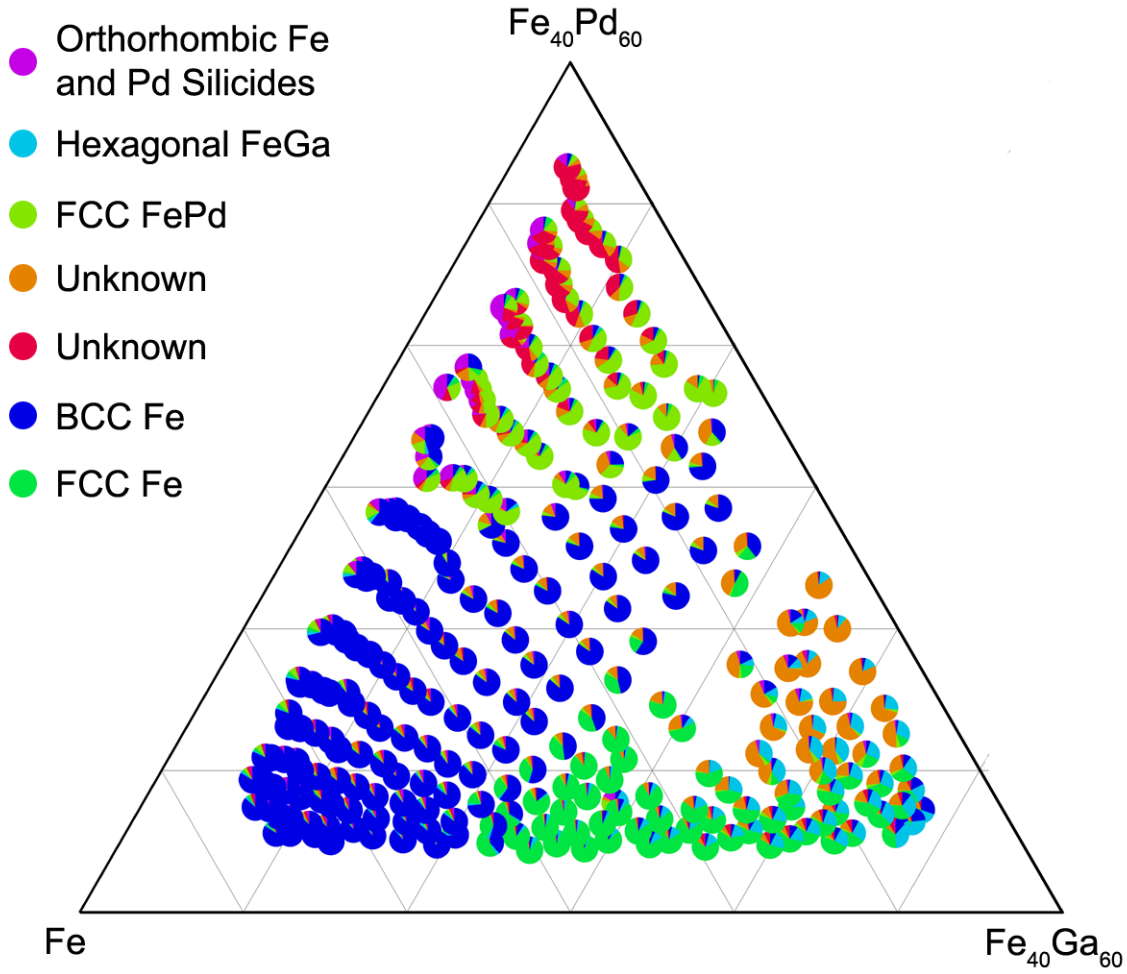

Figure 7.6: The structural phase diagram produced using the weights of the basis diffraction patterns found using NMF. Each pie chart corresponds to a composition for which XRD was measured; each piece of the pie chart corresponds to the weight of one of the basis patterns found using NMF. The phase diagram produced in this manner contains a quantitative representation of the phases present throughout the part of the ternary system that we have explored. Possible matches to a database of known patterns are presented at the top left.

Fe. Our analysis has identified this region starting at the correct composition as the FCC $Fe_{65}Pd_{35}$, which we believe is a quenched phase.

7.6 Problems in Multivariate Analysis of Combinatorial XRD Data

The ultimate goal of our efforts is to reach a point where the analysis of hundreds of spectra automatically identifies all of the pure phases present in a system and quantifies the percent of each phase present in each sample. The work presented here represents a step towards this goal, but there are still several problems left to overcome. Some of these problems are inherent in the use of thin films, while others are a result of the analysis techniques.

One of the problems one faces when attempting to do structure identification of thin films is that it may simply not be possible to precisely identify all the lattice parameters, and thus, the exact structure of the material. In principle, in order to completely determine the lattice parameters, one must measure the intensity of all X-ray reflections, as in powder diffraction. The films under study here are often at least textured, if not sometimes even epitaxially grown, reducing the number of reflections to only the ones from the preferred orientations. It is also possible that the film may exhibit different preferred orientations at different sites, resulting in different sets of reflections for the same structure. As a partial solution to the problem of textured films, it is sometimes possible to obtain some additional information about textured samples by tilting the wafer. Other problems include formation of "spurious" phases such as silicides, as observed here. There could also be formation of meta-stable

phases that are unique to the film structures and not present in bulk form.

In addition to the problems associated with the use of thin films, there are also problems that are particular to the analysis of XRD data using NMF. One of the difficulties of quantifying the amount of each phase present in a sample is that the structure factor can be different for each pattern. This results in a difference in the brightness of different patterns. Thus the relative intensities of the patterns present in a sample provided by the NMF weights matrix and presented in Figure 7.6 cannot be directly compared to the volume fraction of the structures present in a sample. It is possible to get around this problem by re-normalizing the weights of each basis pattern by the intensity of each pure phase. However this is only possible if for each pure phase there is at least one sample that is not a mixture. A second difficulty that is not addressed by NMF is peak shifting due to changing lattice constants. If there are a number of diffraction patterns across which there is a large shift in the position of a peak, then it will be more profitable for the algorithm to "spend" its basis patterns describing this peak shift, instead of identifying other structural phases. The best that can be achieved in the case of peak shifts using NMF is the identification of several patterns, each corresponding to a different shift. Yet a third weakness is that diffraction patterns that correspond to different preferred orientations of the same structure might be identified as different structures. Often, these problems can be partially solved by manually scrutinizing the basis patterns produced by NMF and/or by applying prior knowledge about the materials.

7.7 Conclusion

In this chapter we applied NMF to the problem of de-convolving the diffraction spectra from the Fe-Ga-Pd XRD data set into a much smaller set of basis patterns. We found that the application of NMF is well suited to the analysis of samples that contain multiple crystallographic phases, producing a structural phase diagram that contains a quantitative description of mixed phase regions. The resulting basis patterns also have a lower signal to noise ratio than the experimental patterns, potentially aiding in the identification of crystal structures. This technique shows great promise for the rapid construction of structural phase diagrams.

Chapter 8

Summary & Conclusion

In this dissertation, we have discussed two main topics. Part I focused on expanding the capabilities of the open ended coaxial resonator NFMM, while Part II focused on the rapid analysis of XRD data from combinatorial libraries. Both parts of this dissertation are motivated by the demands of combinatorial materials exploration.

In Chapter 3 we explored the possibility of performing scanning FMR spectroscopy using an open ended coaxial resonator NFMM. By mapping the absorption of microwave energy by a normally magnetized Ga:YIG disk we found that the coaxial microwave probe images the nodes of magnetostatic spin wave modes. We developed a model of the RF magnetic field around the probe tip and found that the nominal spatial resolution of scanning FMR is given by the spatial confinement of the RF magnetic field, which is on the order of the length of the tip ($\sim$2 mm in this case). This spatial resolution is much more coarse than the spatial resolution for the mapping of dielectric properties using the same NFMM geometry, which is on the order of the radius of curvature of the probe tip. However, the sample size in wafer-scale thin film combinatorial libraries is typically a few mm. In this case, we expect that the ability to perform both dielectric and magnetic characterization using the same probe will be quite valuable.

In Chapter 4 we showed that the spatial resolution of the NFMM can be pushed

to the atomic scale by bringing the tip close enough to a conducting sample to form a tunnel junction. The open ended coaxial NFMM is particularly well suited to this type of measurement because it is possible to obtain atomic resolution on conducting samples without making any type of connection (microwave or DC) to the sample. In principle, the large bandwidth (4 MHz in our case) of the NFMM allows it to sample the tunnel junction impedance much more quickly than traditional STM[23]. This increased bandwidth can be used to perform rapid imaging, high frequency displacement detection (up to megahertz frequencies), and shot noise thermometry.[23] In future research we also plan to explore phenomena that induce modulations in the tunnel current near the operational frequency of 2.5 GHz. Such a modulation should be detectable through resonant amplification in the microwave cavity. Possible experiments include single electron spin resonance[24, 25] and investigation of spin-transfer torque oscillations[35].

In Chapter 6 we applied dimensionality reduction, visualization, and agglomerative hierarchical clustering techniques to the problem of analyzing XRD data from an Fe-Ga-Pd ternary combinatorial library. We found that the application of these techniques can greatly speed up the process of mapping out structural phase diagrams by identifying groups of compositions that correspond to the same crystal structure. By selecting the most representative member of each group of spectra, the arduous analysis and classification of hundreds of spectra is reduced to a much shorter analysis of only a few spectra.

In Chapter 7 we applied NMF to the problem of de-convolving the diffraction spectra from the Fe-Ga-Pd XRD data set into much smaller set of basis patterns.

We found that the application of NMF is well suited to the analysis of samples that contain multiple crystallographic phases, producing a structural phase diagram that contains a quantitative description of mixed phase regions. The resulting basis patters also have a lower signal to noise ratio than the experimental patterns, potentially aiding in the identification of crystal structures.

The ultimate goal of our efforts is to reach a point where the analysis of hundreds of new materials can be performed rapidly and the underlying composition-structure-property relationships can be understood physically. The work presented here represents a step towards this goal, but there is still much research to be done.

In the field of NFMM, we are currently working on integrating a quartz tuning fork AFM into the NFMM-STM system so that we can perform AFM, STM, and NFMM on the same region of a sample. The motivation of this investigation is to improve the ability to characterize devices (which frequently have both conducting and non-conducting components) and to explore samples which exhibit nano-scale variation in the surface conductivity and permittivity.

Our work on multivariate analysis of XRD is being focused on integrating knowledge of crystallography directly into the structural identification algorithms and applying existing multivariate techniques to other types of combinatorial data.

Appendix A

Supplemental Information

A.1 Power Absorbed by a Sample for Scanning FMR

The quality factor of the resonator is the energy stored in the resonator divided by the energy lost per cycle. The energy lost per cycle is the average power dissipated in resonator-sample system times the period of one oscillation.

$$Q = \frac{E_R}{\tau P} \tag{A.1}$$

Where Q is the resonator quality factor, E_R is the energy stored in the resonator, τ is the period of an oscillation, and P is the average power dissipated in the resonator-sample system. The power dissipated in the system can be divided into power dissipated in the resonator, P_R and power dissipated in the sample P_S.

$$Q = \frac{E_R}{\tau(P_R + P_S)} \tag{A.2}$$

For $P_s \ll P_r$, we can approximate.

$$Q \simeq \frac{E_R}{\tau P_R}\left(1 - \frac{P_S}{P_R}\right) \tag{A.3}$$

The power dissipated in the sample depends on the applied magnetic field, as does

the resonator Q. Differentiating, we have

$$\frac{\mathrm{d}Q}{\mathrm{d}H} = -\frac{E_R}{\tau P_R^2}\frac{\mathrm{d}P_S}{\mathrm{d}H} \tag{A.4}$$

Up to a calibration constant, we have

$$P_S \propto -\int \frac{\mathrm{d}Q}{\mathrm{d}H}\mathrm{d}H \tag{A.5}$$

The in-phase microwave mixer signal (I_{mix}) is proportional to Q, so we have

$$P_S \propto -\int \frac{\mathrm{d}I_{mix}}{\mathrm{d}H}\mathrm{d}H \tag{A.6}$$

The lock-in amplifier (V_{lock}) output is proportional to $\frac{\mathrm{dI_{mix}}}{\mathrm{dH}}$, so we have

$$P_S \propto -\int V_{\mathrm{lock}}\mathrm{d}H \tag{A.7}$$

A.2 M-H Loops for the Ga:YIG Disk

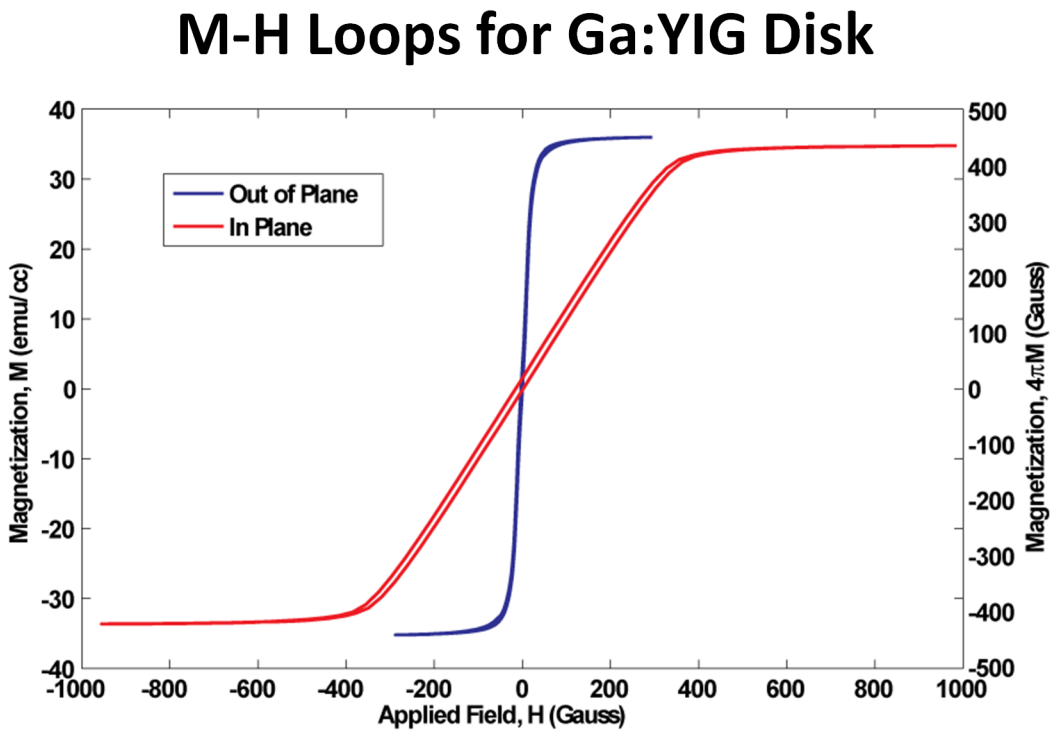

Figure A.1: M-H loops measured using vibrating sample magnetometry for the Ga:YIG disk studied in Chapter 3. The saturation magnetization ($4\pi M_s$) is 450 Gauss.

A.3 Equivalent Circuit Model for NFMM-STM

Several candidate equivalent circuit models were considered to serve as models for the hybrid NFMM-STM. In order to illustrate the modeling process, the simplest candidate model and the associated analysis are briefly discussed here.

Figure A.2 shows the schematic of an equivalent circuit model that includes a capacitive tip-sample interaction as well as an atomic scale tunnel junction between the tip and sample. Note that in this case the sample is assumed to be a perfect conductor; if one wished to include a sample resistance, one could add a resistor in

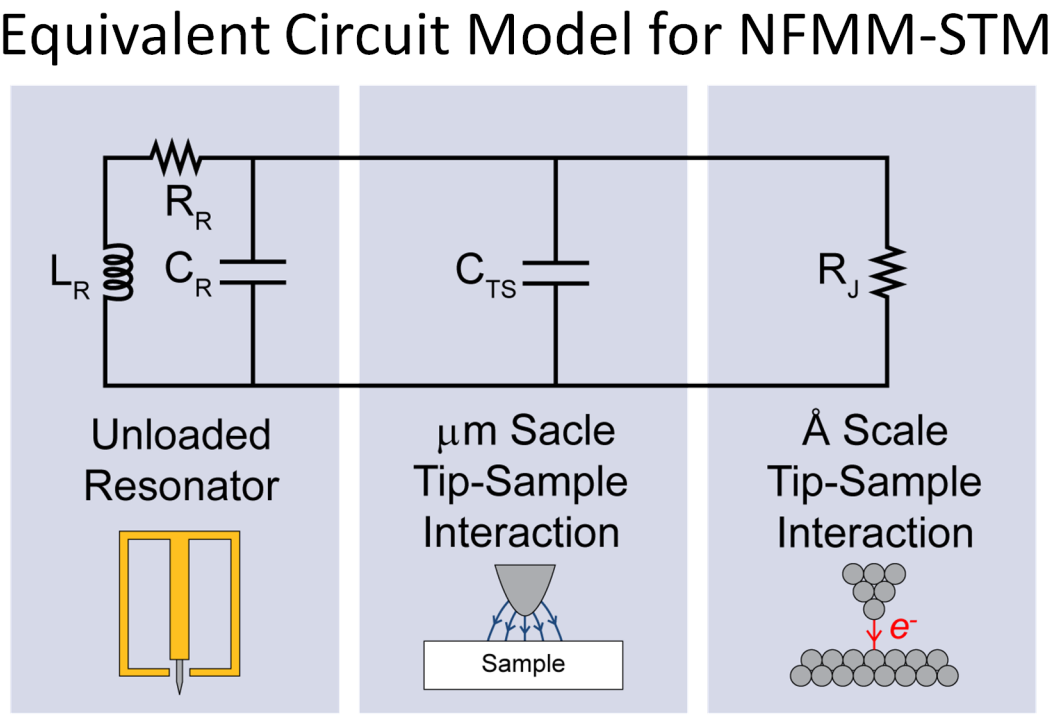

Figure A.2: A simple equivalent circuit model for NFMM-STM. L_R, R_R, and C_R are the unloaded resonator circuit parameters. The classical capacitive interaction between the tip and sample is represented by a capacitance (C_{TS}) in parallel with the unloaded resonator capacitance. Tunneling between the tip and sample is modeled by adding a resistance (R_J) in parallel with the unloaded resonator capacitance.

series with the tip-sample capacitance.

This circuit is analyzed by transforming it into a simple series LCR circuit with modified circuit parameters. Figure A.3 illustrates this process. The first step is to lump together C_R, C_{TS}, and R_J into the form of a real impedance in series with an effective capacitance, as shown in Figure A.3 part (b). These can then be lumped into effective LCR circuit parameters, as shown in Figure A.3 parts (c) and (d). The resulting resonant frequency and quality factor are shown in Figure A.3 part (e). It should be noted that this circuit model is quite simple; more complicated circuits may not have analytical solutions, but should be amenable to SPICE simulations.

Once we have analytic expressions for the resonant frequency and quality factor, as shown in Figure A.3 part (e), we can sweep the circuit model parameters and look at their effect on the resonance. Figure A.4 parts (a) and (b) show the behavior of the resonant frequency and quality factor of the circuit as the tunnel junction resistance is varied while the tip sample capacitance is held fixed. These plots are relevant when scanning the tip over atomic scale features in constant height mode. In constant height mode the topography feedback is turned off, leaving the tip-sample capacitance fixed while the resistance of the tunnel junction may still vary between on-atom and off-atom sites. Figure A.4 parts (c) and (d) show the behavior of the resonant frequency and quality factor as the tip-sample capacitance is varied while the tunnel resistance is assumed to be infinite. This corresponds to approaching the tip to the surface of a perfect conductor before the onset of tunneling.

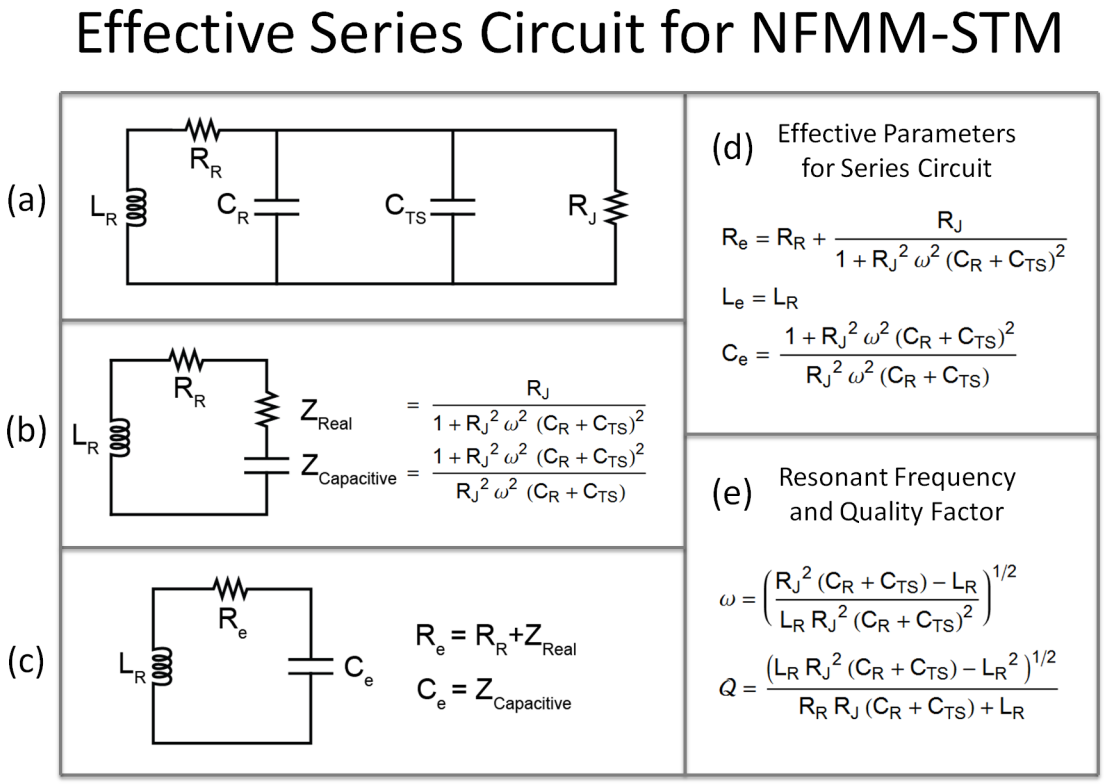

Figure A.3: Part (a) a shows the equivalent circuit model for the NFMM-STM. In order to simplify the calculation of the resonant frequency and quality factor, the circuit is represented as a series circuit as shown in part (b). The series circuit parameters are then lumped together to form effective LCR circuit parameters, as shown in parts (c) and (d). Finally, the resonant frequency and quality factor are calculated using the effective LCR circuit parameters, with the result shown in part (e).

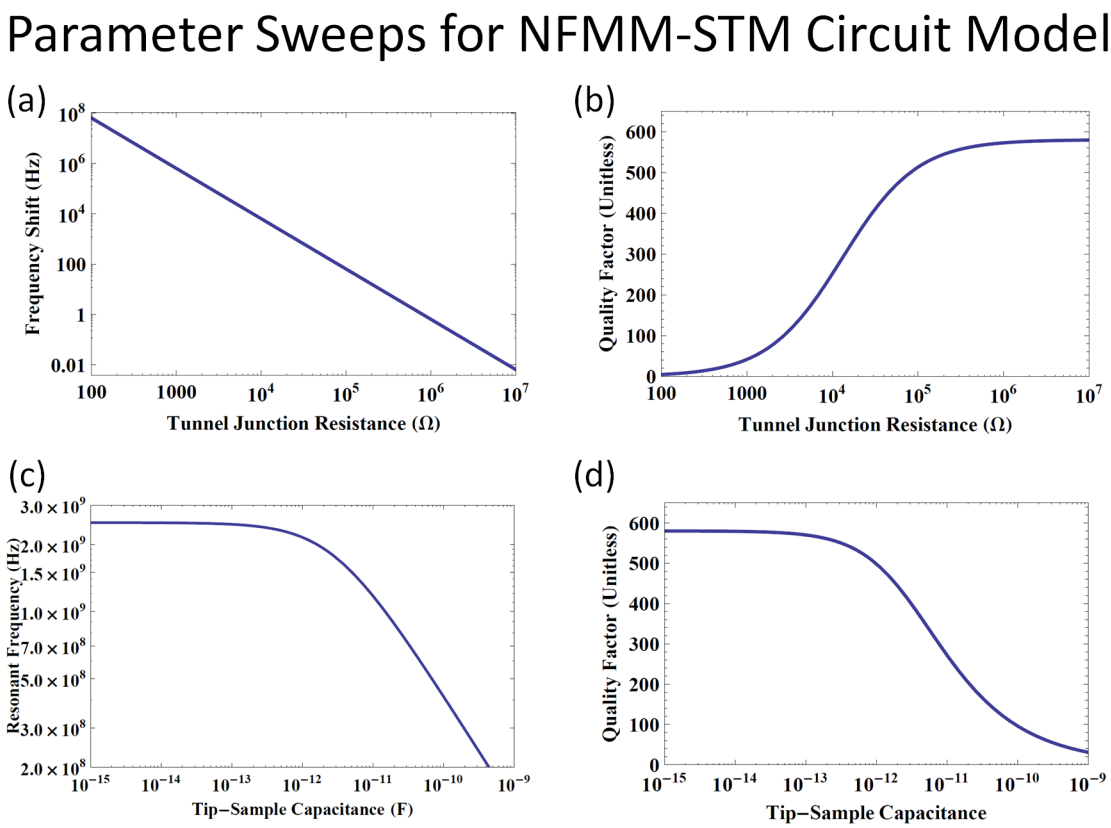

Figure A.4: Theoretical curves for the resonant frequency and quality factor of the resonator as the circuit parameters are varied. Parts (a) and (b) show the behavior of the resonant frequency and quality factor of the circuit as the tunnel junction resistance is varied while C_{TS} is held fixed (in fact we set it to zero here because it is small compared to the resonator capacitance). The resonant frequency decreases as the tunnel junction resistance is decreased. In parts (c) and (d) the tip-sample capacitance, C_{TS}, is varied while the tunnel junction resistance is held fixed at 10^{15} Ω. The values of the unloaded resonator circuit parameters used here correspond to the resonator used for NFMM-STM; in particular, $L_R = 1.43$ nH, $C_R = 2.82$ pF, and $R_R = 39$ mΩ.

Bibliography

[1] X.-D. Xiang, X. Sun, G. Briceño, Y. Lou, K.-A. Wang, H. Chang, W. G. Wallace-Freedman, S.-W. Chen and P. G. Schultz, "A combinatorial approach to materials discovery," Science **23,** 1738 (1995); doi:10.1126/science.268.5218.1738

[2] C. Gao and X.-D. Xiang "Quantitative microwave near-field microscopy of dielectric properties," Rev. Sci. Instrum. **69**, 3846 (1998); doi:10.1063/1.1149189

[3] A. Tselev, S. M. Anlage, Z. Ma, and J. Melngailis, "Broadband dielectric microwave microscopy on micron length scales," Rev. Sci. Instrum. **78**, 044701 (2007); doi:10.1063/1.2719613

[4] A. N. Reznik and V. V. Talanov "Quantitative model for near-field scanning microwave microscopy: Application to metrology of thin film dielectrics," Rev. Sci. Instrum. **79**, 113708 (2008); doi:10.1063/1.3020705

[5] H. Chang, C. Gao, I. Takeuchi, Y. Yoo, J. Wang, P. G. Schultz, X.-D. Xiang, R. P. Sharma, M. Downes, and T. Venkatesan "Combinatorial synthesis and high throughput evaluation of ferroelectric/dielectric thin-film libraries for microwave applications" Appl. Phys. Lett. **72**, 2185 (1998); doi:10.1063/1.121316

[6] H. Chang, I. Takeuchi, and X.-D. Xiang "A low-loss composition region identified from a thin-film composition spread of $(Ba_{1xy}Sr_xCa_y)TiO_3$," Appl. Phys. Lett. **74**, 1165 (1999); doi:10.1063/1.123475

[7] K.-S. Chang, M. Aronova, O. Famodu, I. Takeuchi, S. E. Lofland, J. Hattrick-Simpers, and H. Chang, "Multimode quantitative scanning microwave microscopy of insitu grown epitaxial $Ba_{1x}Sr_xTiO_3$ composition spreads," Appl. Phys. Lett. **79**, 4411 (2001); doi:10.1063/1.1427438

[8] K.-S. Chang, M. A. Aronova, C.-L. Lin, M. Murakami, M.-H. Yu, J. Hattrick-Simpers, O. O. Famodu, S. Y. Lee, R. Ramesh, M. Wuttig, I. Takeuchi, C. Gao, and L. A. Bendersky, "Exploration of artificial multiferroic thin-film heterostructures using composition spreads," Appl. Phys. Lett. **84**, 3091 (2004); doi:10.1063/1.1699474

[9] M. Murakami, K.-S. Chang, M. A. Aronova, C.-L. Lin, M. H. Yu, J. Hattrick-Simpers, M. Wuttig, I. Takeuchi, C. Gao, B. Hu, S. E. Lofland, L. A. Knauss, and L. A. Bendersky "Tunable multiferroic properties in nanocomposite $PbTiO_3$–$CoFe_2O_4$ epitaxial thin films," Appl. Phys. Lett. **87**, 112901 (2005); doi:10.1063/1.2041825

[10] C. Gao, B. Hu, I. Takeuchi, K.-S. Chang, X.-D. Xiang, and G. Wang "Quantitative scanning evanescent microwave microscopy and its applications in characterization of functional materials libraries," Meas. Sci. Technol. **16** 248 (2005); doi: 10.1088/0957-0233/16/1/033

[11] D. E. Steinhauer, C. P. Vlahacos, S. K. Dutta, B. J. Feenstra, F. C. Wellstood, and Steven M. Anlage "Quantitative imaging of sheet resistance with a scanning near-field microwave microscope," Appl. Phys. Lett. **72**, 861 (1998); doi:10.1063/1.120918

[12] S.-C. Lee, C. P. Vlahacos, B. J. Feenstra, A. Schwartz, D. E. Steinhauer, F. C. Wellstood, and S. M. Anlage "Magnetic permeability imaging of metals with a scanning near-field microwave microscope," Appl. Phys. Lett. **77**, 4404 (2000); doi:10.1063/1.1332978

[13] D. I. Mircea and T. W. Clinton "Near-field microwave probe for local ferromagnetic resonance characterization," Appl. Phys. Lett. **90**, 142504 (2007); doi:10.1063/1.2719241

[14] F. Sakran, M. Golosovsky, D. Davidov, and P. Monod "Localized spin-wave excitation by the evanescent microwave scanning probe," Rev. Sci. Instrum. **77**, 023902 (2006); doi:10.1063/1.2167131

[15] C. Gao, B. Hu, X. Li, C. Liu, M. Murakami, K.-S. Chang, C. J. Long, M. Wuttig, and I. Takeuchi "Measurement of the magnetoelectric coefficient using a scanning evanescent microwave microscope," Appl. Phys. Lett. **87**, 153505 (2005); doi:10.1063/1.2093925

[16] A. Imtiaz, and S. M. Anlage, "A novel STM-assisted microwave microscope with capacitance and loss imaging capability," Ultramicroscopy **94,** 209 (2003); doi:10.1016/S0304-3991(02)00291-7

[17] A. Imtiaz, M. Pollak, S. M. Anlage, J. D. Barry, and J. Melngailis, "Near-field microwave microscopy on nanometer length scales," J. Appl. Phys. **97**, 044302 (2005); doi:10.1063/1.1844614

[18] B. T. Rosner and D. W. van der Weide, "High-frequency near-field microscopy," Rev. Sci. Instrum. **73**, 2505 (2002); doi:10.1063/1.1482150

[19] S. M. Anlage, D. E. Steinhauer, B. J. Feenstra, C. P. Vlahacos, and F. C. Wellstood, *Microwave Superconductivity* (Kluwer, Amsterdam, 2001), pp. 239–269.

[20] C. Gao, B. Hu, I. Takeuchi, K.-S. Chang, X.-D. Xiang, and G. Wang, "Quantitative scanning evanescent microwave microscopy and its applications in characterization of functional materials libraries," Meas. Sci. Technol. **16**, 248 (2005); doi:10.1088/0957-0233/16/1/033

[21] X. W. Tu, J. H. Lee, and W. Ho, "Atomic-scale rectification at microwave frequency," J. Chem. Phys. **124**, 021105 (2006); doi:10.1063/1.2159491

[22] Z. J. Donhauser, G. S. McCarty, L. A. Bumm, and P. S. Weiss, "High resolution dopant profiling using a tunable AC scanning tunneling microscope," AIP Conf. Proc. **550**, 641 (2001); doi:10.1063/1.1354469

[23] U. Kemiktarak, T. Ndukum, K. C. Schwab, and K. L. Ekinci, "Radio-frequency scanning tunnelling microscopy," Nature London **450**, 85 (2007); doi:10.1038/nature06238

[24] Y. Manassen, R. J. Hamers, J. E. Demuth, and A. J. Castellano, Jr., "Direct observation of the precession of individual paramagnetic spins on oxidized silicon surfaces," Phys. Rev. Lett. **62**, 2531 (1989); doi:10.1103/PhysRevLett.62.2531

[25] J. Lee, X. Tu, and W. Ho, "Spectroscopy and Microscopy of Spin-Sensitive Rectification Current Induced by Microwave Radiation," Nano Lett. **5**, 2613 (2005); doi:10.1021/nl0522330

[26] R. F. Soohoo, "A microwave magnetic microscope," J. Appl. Phys. **33**, 1276 (1962); doi:10.1063/1.1728690

[27] G. Binnig, H. Rohrer, C. Gerber, and E. Weibel, "Tunneling through a controllable vacuum gap," Appl. Phys. Lett. **40**, 178 (1982); doi:10.1063/1.92999

[28] C. Gao, T. Wei, F. Duewer, Y. Lu, and X.-D. Xiang, "High spatial resolution quantitative microwave impedance microscopy by a scanning tip microwave near-field microscope," Appl. Phys. Lett. **71**, 1872 (1997); doi:10.1063/1.120444

[29] SPI Supplies, 466PS-AB.

[30] SPI Supplies, 436HP-AB, Grade SPI-2.

[31] Veeco, cut Platinumt/Iridium STM tips, Part # PT10.

[32] X.-D. Xiang, C. Gao, F. Duewer, H. Yang, and Y. Lu, U. S. Patent No. 7550963 B1 June, **23**, (2009).

[33] B. Knoll, F. Keilmann, A. Kramer, and R. Guckenberger, "Contrast of microwave near-field microscopy," Appl. Phys. Lett. **70**, 2667 (1997); doi:10.1063/1.119255

[34] F. Duewer, C. Gao, I. Takeuchi, and X.-D. Xiang, "Tip-sample distance feedback control in a scanning evanescent microwave microscope," Appl. Phys. Lett. **74**, 2696 (1999); doi:10.1063/1.123940

[35] S. I. Kiselev, J. C. Sankey, I. N. Krivorotov, N. C. Emley, R. J. Schoelkopf, R. A. Buhrman, and D. C. Ralph, "Microwave oscillations of a nanomagnet driven by a spin-polarized current," Nature London **425**, 380 (2003); doi:10.1038/nature01967

[36] K. Rivkin, and J. B. Kettersona, "Micromagnetic simulations of absoption spectra," J. Magn. Magn. Mater. **306**, 204 (2006); doi:10.1016/j.jmmm.2006.02.245

[37] K. Rivkin, A. Heifetz, P.R. Sievert, J.B. Ketterson, "Resonant modes of dipole-coupled lattices" Phys. Rev. B **70**, 184410 (2004); doi: 10.1103/PhysRevB.70.184410

[38] S. V. Vonsovskii, Ferromagnetic Resonance: the Phenomenon of Resonant Absorption of a High-Frequency Magnetic Field in Ferromagnetic Substances, (Pergamon Press, Pergamon, 1966).

[39] P. Kabos and V.S Stalmachov, Magnetostatic Waves and Their Applications, (Chapman and Hall, London, 1994).

[40] C. Kittel "On the theory of ferromagnetic resonance absorption," Phys. Rev. **73**, 155 (1948); doi:10.1103/PhysRev.73.155

[41] L. D. Landau, E. M. Lifshitz "Theory of the dispersion of magnetic permeability in ferromagnetic bodies", Phys. Z. Sowietunion **8**, 153 (1935).

[42] T. L. Gilbert "A phenomenological theory of damping in ferromagnetic materials", IEEE Trans. Mag. **40**, 3443 (2004); doi:10.1109/TMAG.2004.836740

[43] S. E. Lofland, S. M. Bhagat, Q. Q. Shu, M. C. Robson, and R. Ramesh, "Magnetic imaging of perovskite thin films by ferromagnetic resonance microscopy—$La_{0.7}Sr_{0.3}MnO_3$," Appl. Phys. Lett. **75**, 1947 (1999); doi:10.1063/1.124880

[44] S.-C. Lee, C. P. Vlahacos, B. J. Feenstra, A. Schwartz, D. E. Steinhauer, F. C. Wellstood, and S. M. Anlage, "Magnetic permeability imaging of metals with a scanning near-field microwave microscope," Appl. Phys. Lett. **77**, 4404 (2000); doi:10.1063/1.1332978

[45] D. I. Mircea and T. W. Clinton, "Near-field microwave probe for local ferromagnetic resonance characterization," Appl. Phys. Lett. **90**, 142504 (2007); doi:10.1063/1.2719241

[46] N. Benatmane and T. W. Clinton "The effects of a microbridge buffer layer on the sensitivity of a local ferromagnetic resonance probe," J. Appl. Phys. **103**, 07D925 (2008); doi:10.1063/1.2844603

[47] F. Sakran, A. Copty, M. Golosovsky, N. Bontemps, D. Davidov, and A. Frenkel, "Electron spin resonance microscopic surface imaging using a microwave scanning probe," Appl. Phys. Lett. **82**, 1479 (2003); doi:10.1063/1.1556561

[48] T. An, N. Ohnishi, T. Eguchi, Y. Hasegawa, and P. Kabos, "Local Excitation of Ferromagnetic Resonance and Its Spatially Resolved Detection With an Open-Ended Radio-Frequency Probe," IEEE Magn. Lett. **1**, 3500104 (2010); doi:10.1109/LMAG.2010.2040247

[49] H. Koinuma and I. Takeuchi, "Combinatorial solid-state chemistry of inorganic materials," Nature Materials **3**, 429 (2004); doi: 10.1038/nmat1157

[50] Combinatorial Materials Syntheses, edited by I. Takeuchi and X.-D. Xiang, (Dekker, New York, 2003).

[51] I. Takeuchi, R. B. van Dover, and H. Koinuma, "Combinatorial Synthesis and Evaluation of Functional Inorganic Materials Using Thin-Film Techniques," MRS Bulletin **27**, 301 (2002); doi:10.1557/mrs2002.97

[52] T. Fukumura, M. Ohtani, M. Kawasaki, Y. Okimoto, T. Kageyama, T. Koida, T. Hasegawa, Y. Tokura, and H. Koninuma, "Rapid construction of a phase diagram of doped Mott insulators with a composition-spread approach," Appl. Phys. Lett. **77**, 3426 (2000); doi:10.1063/1.1326847

[53] I. Takeuchi, W. Yang, K.-S. Chang, M. Aronova, R. D. Vispute, T. Venkatesan, L. A. Bendersky, "Monolithic multichannel ultraviolet detector arrays and continuous phase evolution in MgxZn1xO composition spreads," Journal of Applied Physics **94**, 7336 (2003); doi:10.1063/1.1623923

[54] R. B. van Dover, L. F. Schneemeyer, and R. M. Fleming, "Discovery of a useful thin-film dielectric using a composition-spread approach," Nature **392**, 162-164 (1998); doi:10.1038/32381

[55] I. Takeuchi, O. Famodu, J. C. Read, M. Aronova, K.-S. Chang, C. Craciunescu, S. E. Lofland, M. Wuttig, F. C. Wellstood, L. Knouse, A. Orozco, "Identification of novel compositions of ferromagnetic shape-memory alloys using composition spreads," Nat. Mater. **2**, 180 (2003); doi:10.1038/nmat829

[56] S.-W. Cheong and H. Y. Hwang, Ferromagnetism vs. Charge/Orbital Ordering in Mixed-Valent Manganites: Colossal Magneto-Resistive Oxides, edited by Y. Tokura (Gordon and Breach, Amsterdam, 2000), p. 237.

[57] A. Damascelli, Z. Hussain, and Z.-X. Shen, "Angle-resolved photoemission studies of the cuprate superconductors," Rev. Mod. Phys. **75**, 473 (2003); doi:10.1103/RevModPhys.75.473

[58] J. C. Zhao, "A Combinatorial Approach for Structural Materials," Adv. Eng. Mat. **3**, 143 (2001); doi:10.1002/1527-2648(200103)3:3<143::AID-ADEM143>3.0.CO;2-F

[59] J. C. Zhao, J. Mater. Res. "A combinatorial approach for efficient mapping of phase diagrams and properties," **16**, 1565 (2001).

[60] M. J. Turchinskaya, L. A. Bendersky, A. J. Shapiro, K. S. Chang, I. Takeuchi, and A. L. Roytburd, "Rapid constructing magnetic phase diagrams by magneto-optical imaging of composition spread films," Journal of Materials Research **19**, 2546 (2004); doi:10.1557/JMR.2004.0327

[61] Special issue of Meas. Sci. and Technol. Combinatorial Materials Science **16** (2005).

[62] E. D. Issacs, M. Marcus, G. Aeppli, X.-D. Xiang, X.-D. Sun, P. G. Schultz, H.-K. Kao, G. S. Cargill, R. Haushalter, "Synchrotron X-ray microbeam diagnostics of combinatorial synthesis," Appl. Phys. Lett. **73**, 1820 (1998).

[63] Y. K. Yoo, T. Ohnishi, G. Wang, F. W. Duewer, X.-D. Xiang, Y.-S. Chu, D.D. Mancini, Y.-Q. Li, R. C. O'Handley, "Continuous mapping of structure–property relations in $Fe_{1-x}Ni_x$ metallic alloys fabricated by combinatorial synthesis," Intermetallics **9**, 541 (2001); doi:10.1016/S0966-9795(01)00030-9

[64] Y. S. Chu, A. Tkachuk, S. Vogt, P. Illinski, D. A. Walko, D. C. Mancini, E. M. Dufresne, L. He, F. Tsui, "Structural investigation of CoMnGe combinatorial epitaxial thin films using microfocused synchrotron X-ray," Appl. Surf. Sci. **223**, 175 (2004); doi:10.1016/S0169-4332(03)00894-8

[65] E. D. Specht, A Rah, G. M. Pharr, E. P. George, P. Zschack, H. Hong and J. Ilavsky, "Rapid structural and chemical characterization of ternary phase diagrams using synchrotron radiation," J. Mater. Res. **18**, 2522 (2003).

[66] M. Ohtani, T. Fukumura, M. Kawasaki, K. Omote, T. Kikuchi, J. Harada, A. Ohtomo, M. Lippmaa, T. Ohnishi, D. Komiyama, R. Takahashi, Y. Matsumoto, and H. Koinuma, "Concurrent X-ray diffractometer for high throughput structural diagnosis of epitaxial thin films," Appl. Phys. Lett. **79**, 3594 (2001); doi:10.1063/1.1415402

[67] R. Kaimuna, H. Nakano, and K. Ishida, "Martensitic transformations in NiMnAl beta phase alloys," Metall. Mater. Trans. A **27A**, 4153 (1996).

[68] O. O. Famodu, J. Hattrick-Simpers, M. Aronova, K.-S. Chang, M. Murakami, M. Wuttig, T. Okazaki, Y. Furuya and I. Takeuchi, Materials Transactions, JIM **45**, 173 (2004).

[69] M. J. Turchinskaya, L. A. Bendersky, A. J. Shapiro, K. S. Chang, I. Takeuchi, and A. L. Roytburd, "Rapid constructing magnetic phase diagrams by magneto-optical imaging of composition spread films," J. Mater. Res. **19**, 2546 (2004); doi:10.1557/JMR.2004.0327

[70] I. Takeuchi, C. J. Long, O. O. Famodu, M. Murakami, J. Hattrick-Simpers, and G. W. Rubloff, "Data management and visualization of X-ray diffraction spectra from thin film ternary composition spreads," Rev. Sci. Instrum. **76**, 062223 (2005); doi:10.1063/1.1927079

[71] J. Cui, Y. S. Chu, O. O. Famodu, Y. Furuya, J. Hattrick-Simpers, R. D. James, A. Ludwig, S. Thienhaus, M. Wuttig, Z. Zhang, and I. Takeuchi, "Combinatorial search of thermoelastic shape-memory alloys with extremely small hysteresis width," Nat. Mater. **5**, 286 (2006); doi:10.1038/nmat1593

[72] G. Barr, W. Dong, C. J. Gilmore, "PolySNAP: a computer program for analysing high-throughput powder diffraction data," J. Appl. Cryst. **37**, 658 (2004); doi:10.1107/S0021889804011173

[73] G. Petculescu, K. B. Hathaway, T.A. Lograsso, M. Wun-Fogle, A.E. Clark, "Magnetic field dependence of galfenol elastic properties," J. Appl. Phys. **97**, 10M315 (2005).

[74] M. Sugiyama, R. Oshima, F. E. Fujita, "Martensitic Transformation in the Fe-Pd Alloy System," Mater. Trans. JIM **25**, 585 (1984).

[75] T. Fukuda, T. Takeuchi, T. Kakeshita, Material Japan **40**, 544 (2001).

[76] I.T. Jollife, Principal Component Analysis. (Springer, New York, 1986).

[77] Gower, J.C. "Some distance properties of latent root and vector methods used in multivariate analysis," Biometrica, **53**, 325 (1966).

[78] A. D. Gordon, Classification, 2nd ed. (Chapman and Hall, London CRC, Boca Raton, FL, 1999).

[79] A. Belsky, M. Hellenbrandt, V. L. Karen, and P. Luksch, "New developments in the Inorganic Crystal Structure Database (ICSD): accessibility in support of materials research and design," Acta Cryst. **B58**, 364 (2002); doi:10.1107/S0108768102006948

[80] Binary Alloy Phase Diagrams, 2nd ed., edited by T. B. Massalki (ASM International, Ohio, 1990), p. 1064.

[81] Binary Alloy Phase Diagrams, 2nd ed., edited by T. B. Massalki (ASM International, Ohio, 1990), p. 1751.

[82] C. J. Gilmore, G. Barr. & J. Paisley, "High-throughput powder diffraction. I. A new approach to qualitative and quantitative powder diffraction pattern analysis using full pattern profiles," J. Appl. Cryst. **37**, 231 (2004); doi:10.1107/S002188980400038X

[83] G. Barr, W. Dong, & C. J. Gilmore, "High-throughput powder diffraction. II. Applications of clustering methods and multivariate data analysis," J. Appl. Cryst. **37**, 243 (2004); doi:10.1107/S0021889804000391

[84] C. J. Long, J. Hattrick-Simpers, M. Murakami, R. C. Srivastava, I. Takeuchi, V. L. Karen, and X. Li, "Rapid structural mapping of ternary metallic alloy systems using the combinatorial approach and cluster analysis," Rev. Sci. Instrum. **78**, 072217 (2007); doi:10.1063/1.2755487

[85] J. Koeda, Y. Nakamura, T. Fukuda, T. Kakeshita, T. Takeuchi, and K. Kishio, "Magnetic field dependence of galfenol elastic properties," Trans. Mater. Res. Soc. Jpn. **26**, 215 (2001); doi:10.1063/1.1855711

[86] Certain commercial materials and equipment are identified in this paper to specify the experimental procedure. In no instance does such identification imply recommendation or endorsement by the National Institute of Standards and Technology or that the material or equipment identified is necessarily the best available for the purpose.

[87] D. D. Lee and H. S. Seung, "Learning the parts of objects by non-negative matrix factorization," Nature London **401**, 788 (1999); doi:10.1038/44565

[88] F. Shahnaz, M. Berry, V. P. Pauca, and R. Plemmons, "Document clustering using nonnegative matrix factorization," Inf. Process. Manage. **42**, 373 (2006); doi:10.1016/j.ipm.2004.11.005

[89] J. Piper, V. P. Pauca, R. J. Plemmons, and M. Giffin, "Object characterization from spectral data using nonnegative factorization and information theory," Proceedings of AMOS Technical Conference, Maui, HI (2004).

[90] M. W. Berry, M. Browne, A. N. Langville, P. V. Pauca, and R. J. Plemmons, "Algorithms and applications for approximate nonnegative matrix factorization," Comput. Stat. Data Anal. **52**, 155 (2007); doi:10.1016/j.csda.2006.11.006

[91] A. Cichocki and R. Zdunek, "Regularized alternating least squares algorithms for non-negative matrix/tensor factorization ," Lect. Notes Comput. Sci. 4493, 793 (2007); doi:10.1007/978-3-540-72395-0_97

[92] A. Cichocki and R. Zdunek, http://www.bsp.brain.riken.jp/ICALAB/nmflab.html

[93] C. Ding, T. Lib, and W. Peng, "On the equivalence between Non-negative Matrix Factorization and Probabilistic Latent Semantic Indexing," Comput. Stat. Data Anal. **52**, 3913 (2008); doi:10.1016/j.csda.2008.01.011

[94] S. Wild, J. Curry, and A. Dougherty, "Improving non-negative matrix factorizations through structured initialization," Pattern Recogn. **37**, 2217 (2004); doi:10.1016/j.patcog.2004.02.013

[95] C. Boutsidis and E. Gallopoulos, "SVD based initialization: A head start for nonnegative matrix factorization," Pattern Recogn. **41**, 1350 (2008); doi:10.1016/j.patcog.2007.09.010

[96] NIST Standard Reference Data Program, Gaithersburg, MD 20899.

Christian John Long

University of Maryland • Department of Physics

College Park, Maryland 20742 USA

crslong@gmail.com

EDUCATION

Ph.D., Physics August, 2011

University of Maryland, College Park

Thesis: Near-field microwave microscopy and multivariate analysis of XRD data

Advisor: Ichiro Takeuchi

B.S., Physics December, 2004

University of Maryland, College Park

AWARDS

- **Best Presentation**, Center for Nanophysics and Advanced Materials Graduate Student Seminar, College Park, MD, 2010.
- **Ludo Frevel Crystallography Scholarship**, 2009.
- **Best Poster**, 4th International Workshop on Combinatorial Materials Science & Technology, San Juan, PR, 2006.
- **Bruker Excellence in X-Ray Diffraction Scholarship**, 2006.
- **Bruker Excellence in X-Ray Diffraction Scholarship**, 2005.

PUBLICATIONS

1. **C. J. Long**, S. A. Kitt, N. Taketoshi, J. Lee, S. Lofland, and I. Takeuchi, "Development of a Scanning Near-Field Microwave Microscope for Localized Ferromagnetic Resonance Measurements," In preparation.
2. J. Lee, **C. J. Long**, H. Yang, X.-D. Xiang, and I. Takeuchi, "Atomic Resolution Imaging at 2.5 GHz using Near-Field Microwave Microscopy," Appl. Phys. Lett. **97**, 183111 (2010).
3. **C. J. Long**, D. Bunker, X. Li, V. L. Karen, and I. Takeuchi, "Rapid Identification of Structural Phases in Combinatorial Thin-film Libraries using X-Ray Diffraction and Non-Negative Matrix Factorization," Rev. Sci. Instrum. **80**, 103902 (2009).
4. **C. J. Long**, J. Hattrick-Simpers, M. Murakami, R. C. Srivastava, I. Takeuchi, V. L. Karen, and X. Li, "Rapid Structural Mapping of Ternary Metallic Alloy Systems using the Combinatorial Approach and Cluster Analysis," Rev. Sci. Instrum. **78**, 072217 (2007).
5. R. Dell'Anna, P. Lazzeri, R. Canteri, **C. J. Long**, J. Hattrick-Simpers, I. Takeuchi, M. Anderle, "Data Analysis in Combinatorial Experiments: Applying Supervised Principal Component Technique to Investigate the Relationship Between ToF-SIMS Spectra and the Composition Distribution of Ternary Metallic Alloy Thin Films," QSAR Comb. Sci. **27**, 171 (2007). **Cover Article**
6. M. Murakami, S. Fujino, S.-H. Lim, **C. J. Long**, L. G. Salamanca-Riba, M. Wuttig, I. Takeuchi, V. Nagarajan, and A. Varatharajan, "Fabrication of Multiferroic Epitaxial $BiCrO_3$ Thin Films," Appl. Phys. Lett. **88**, 152902 (2006).
7. I. Takeuchi, **C. J. Long**, O. O. Famodu, M. Murakami, J. Hattrick-Simpers, and G. W. Rubloff, "Data Management and Visualization of X-Ray Diffraction Spectra from Thin Film Ternary Composition Spreads," Rev. Sci. Instrum. **76**, 062223 (2005).
8. C. Gao, B. Hu, X. Li, C. Liu, M. Murakami, K.-S. Chang, **C. J. Long**, M. Wuttig, and I. Takeuchi, "Measurement of the Magnetoelectric Coefficient using a Scanning Evanescent Microwave Microscope," Appl. Phys. Lett. **87**, 153505 (2005).

SELECTED PRESENTATIONS

1. **C. J. Long**, J. Lee, S. Kitt, S. Lofland, and I. Takeuchi, "Development of a Scanning Near-Field Microwave Microscope for Localized Magnetic Resonance Measurements," 11th Joint MMM/Intermag Conference, Washington, DC, 19 January, 2010.
2. **C. J. Long**, I. Takeuchi, D. Bunker, X. Li, and V. L. Karen, "Rapid Identification of Structural Phases in Combinatorial Thin-Film Libraries using X-Ray Diffraction and Non-Negative Matrix Factorization," Materials Research Society Spring Meeting, San Francisco, CA, 16 April, 2009.
3. **C. J. Long**, N. Taketoshi, I. Takeuchi, H. Yang, and X.-D. Xiang, "Development of an Evanescent Microwave Probe – STM to Study Localized ESR," American Physical Society March Meeting, New Orleans, LA, 13 March, 2008.
4. **C. J. Long**, J. Hattrick-Simpers, M. Murakami, R. C. Srivastava, I. Takeuchi, V. L. Karen, and X. Li, "Rapid Structural Mapping of Ternary Metallic Alloy Systems Using the Combinatorial Approach and Cluster Analysis," Materials Research Society Fall Meeting, Boston, MA, 28 November, 2007.
5. **C. J. Long**, J. Hattrick-Simpers, M. Murakami, R.C. Srivastava, I. Takeuchi, and V. L. Karen, "Structural Mapping of Ternary Metallic Alloy Systems Using the Combinatorial Approach: Data Visualization and Cluster Analysis of XRD Data," 4th International Workshop on Combinatorial Materials Science & Technology, San Juan, PR, 5 December, 2006.
6. **C. J. Long**, O. O. Famodu, M. Murakami, J. Hattrick-Simpers, G. W. Rubloff, I. Takeuchi, M. Stukowski, and K. Rajan, "Visualization of X-Ray Diffraction Spectra from Combinatorial Thin Film Libraries," Materials Research Society Fall Meeting, Boston, MA, 1 December, 2005.

PROFESSIONAL AFFILIATIONS

- Member, American Physical Society (APS) 2008-Present
- Member, Materials Research Society (MRS) 2005-Present